UNIVERSIDADE FEDERAL DE MINAS GERAIS
Escola de Engenharia
Programa de Pós-graduação em Engenharia Elétrica

Jose Olger Vargas Garay

EFFICIENT INVERSE SCATTERING ALGORITHMS BASED ON CONJUGATE GRADIENT APPROACHES FOR MICROWAVE IMAGING

Belo Horizonte
2022

Jose Olger Vargas Garay

EFFICIENT INVERSE SCATTERING ALGORITHMS BASED ON CONJUGATE GRADIENT APPROACHES FOR MICROWAVE IMAGING

Versão final

Tese de Doutorado apresentada ao Programa de Pós-Graduação em Engenharia Elétrica da Universidade Federal de Minas Gerais, como requisito parcial para obtenção do título de Doutor em Engenharia Elétrica.

Orientador: Ricardo Luiz da Silva Adriano

Belo Horizonte
2022

Garay, Jose Olger Vargas.
G212e Efficient inverse scattering algorithms based on conjugate gradient approaches for microwave imaging [recurso eletrônico] / Jose Olger Vargas Garay. - 2022.
1 recurso online (120 f. : il., color.) : pdf.

Orientador: Ricardo Luiz da Silva Adriano.

Tese (doutorado) - Universidade Federal de Minas Gerais, Escola de Engenharia.

Apêndices: f. 116-120.

Bibliografia: f. 110-115.
Exigências do sistema: Adobe Acrobat Reader.

1. Engenharia elétrica - Teses. 2. Equações integrais - Teses. 3. Microondas - Teses. 4. Ondas eletromagnéticas - Espalhamento - Teses. I. Adriano, Ricardo Luiz da Silva. II. Universidade Federal de Minas Gerais. Escola de Engenharia. III. Título.

CDU: 621.3(043)

Ficha catalográfica elaborada pela Bibliotecária Roseli Alves de Oliveira CRB/6 2121
Biblioteca Prof. Mário Werneck, Escola de Engenharia da UFMG

UNIVERSIDADE FEDERAL DE MINAS GERAIS
ESCOLA DE ENGENHARIA
PROGRAMA DE PÓS-GRADUAÇÃO EM ENGENHARIA ELÉTRICA

FOLHA DE APROVAÇÃO

"EFFICIENT INVERSE SCATTERING ALGORITHMS BASED ON CONJUGATE GRADIENT APPROACHES FOR MICROWAVE IMAGING"

JOSE OLGER VARGAS GARAY

Tese de Doutorado submetida à Banca Examinadora designada pelo Colegiado do Programa de Pós-Graduação em Engenharia Elétrica da Escola de Engenharia da Universidade Federal de Minas Gerais, como requisito para obtenção do grau de Doutor em Engenharia Elétrica. Aprovada em 12 de setembro de 2022. Por:

Prof. Dr. Ricardo Luiz da Silva Adriano
DEE (UFMG) - Orientador

Prof. Dr. Renato Cardoso Mesquita
DEE (UFMG)

Prof. Dr. Fernando José da Silva Moreira
DELT (UFMG)

Profa. Dra. Úrsula do Carmo Resende
Departamento de Engenharia Elétrica (CEFET-MG)

Prof. Dr. Xisto Lucas Travassos Junior
Departamento de Engenharia Elétrica e Eletrônica (UFSC)

Documento assinado eletronicamente por **Renato Cardoso Mesquita**, **Professor do Magistério Superior**, em 12/09/2022, às 16:58, conforme horário oficial de Brasília, com fundamento no art. 5º do Decreto nº 10.543, de 13 de novembro de 2020.

Documento assinado eletronicamente por **Ricardo Luiz da Silva Adriano**, **Professor do Magistério Superior**, em 12/09/2022, às 16:59, conforme horário oficial de Brasília, com fundamento no art. 5º do Decreto nº 10.543, de 13 de novembro de 2020.

Documento assinado eletronicamente por **Fernando Jose da Silva Moreira**, **Professor do Magistério Superior**, em 13/09/2022, às 09:51, conforme horário oficial de Brasília, com fundamento no art. 5º do Decreto nº 10.543, de 13 de novembro de 2020.

Documento assinado eletronicamente por **Ursula do Carmo Resende**, **Usuária Externa**, em 14/09/2022, às 12:21, conforme horário oficial de Brasília, com fundamento no art. 5º do Decreto nº 10.543, de 13 de novembro de 2020.

Documento assinado eletronicamente por **XISTO LUCAS TRAVASSOS JUNIOR**, **Usuário Externo**, em 14/09/2022, às 17:57, conforme horário oficial de Brasília, com fundamento no art. 5º do Decreto nº 10.543, de 13 de novembro de 2020.

A autenticidade deste documento pode ser conferida no site https://sei.ufmg.br/sei/controlador_externo.php?acao=documento_conferir&id_orgao_acesso_externo=0, informando o código verificador **1744627** e o código CRC **C29C55AE**.

To my family

Acknowledgements

First of all, I would like to express my sincere gratitude to my advisor, Prof. Ricardo Adriano, for his support, encouragement, motivation, and guidance in my Ph.D. study and research. I am thankful to him for his collaboration, patience, and suggestions for the development of this research.

I would like to thank André Batista for interesting discussions and suggestions on inverse scattering algorithms and microwave imaging. I also would like to thank Prof. Lucas Batista for his helpful comments and collaboration in my research.

I would also like to thank all the laboratory partners. Especially, I would like to thank Polyanna and Maria for their help and friendship over the years.

I would like to acknowledge my colleagues and friends: Andrés, Marlon, Luilly, and Diego Tami for their collaboration, fun, and friendship. I thank my dear friend Pilar. Thanks for all the laughs and shared moments. Many thanks to my friends at UFMG for making my life more balanced and enjoyable.

I would like to express my deep sense of gratitude to my parents. Without their support and sacrifice, I would not be able to reach my dream.

Finally, I would like to thank the CNPq agency for providing the scholarship to support me during my doctoral study.

"Fall in love with some activity, and do it! Nobody ever figures out what life is all about, and it doesn't matter. Explore the world. Nearly everything is really interesting if you go into it deeply enough. Work as hard and as much as you want to on the things you like to do the best. Don't think about what you want to be, but what you want to do..."

Richard Feynman

Resumo

O problema de espalhamento eletromagnético inverso para imageamento em microondas visa recuperar as propriedades dielétricas, localização, tamanho e forma de objetos espalhadores dentro de um domínio de interesse inacessível. Este é um importante campo das aplicações em eletromagnetismo como imagens biomédicas, detecção de objetos enterrados, exploração de petróleo e gás e avaliação não-destrutiva. O imageamento é realizado analisando as medições de campo espalhado. Nesse contexto, um método de inversão iterativo é frequentemente necessário para minimizar uma função objetivo construída pelo erro entre o campo espalhado medido e o campo espalhado calculado.

Nesta tese são apresentados diferentes algoritmos eficientes baseados no método do gradiente conjugado (*conjugate gradient method*, CGM) para resolver problemas de espalhamento inverso em duas e três dimensões. Este método consiste na solução do problema de espalhamento direto e o cálculo da direção do gradiente da função objetivo dentro de cada iteração. Dependendo da aproximação do gradiente, o CGM pode ser classificado em duas abordagens principais: métodos linearizados e não linearizados. Cada cálculo do problema direto pode ter um alto custo computacional. Assim, para evitar o esforço computacional os solucionadores diretos são implementados eficientemente usando métodos iterativos para resolver sistemas lineares combinados com algoritmos FFT (*fast Fourier transform*).

Os métodos de inversão propostos nesta tese são baseados em abordagens de gradiente conjugado. Inicialmente é proposta uma implementação eficiente do CGM não linearizado, o qual não requer o cálculo da matriz inversa. Essa abordagem reduz o custo computacional e os requisitos de armazenamento do algoritmo de reconstrução em comparação com a versão original. Em seguida, também é proposto um CGM baseado em subespaços (*subspace-based CGM*, S-CGM), que é baseado no CGM linearizado e no conceito de subespaços. Por fim, propomos um *fast* CGM para resolver problemas de espalhamento inverso com baixa não linearidade. Várias simulações numéricas foram realizadas para validar os algoritmos de inversão propostos. No caso 2D, os métodos foram testados com dados sintéticos e experimentais. Os resultados da reconstrução apresentam eficácia na estimativa da localização, forma do objeto e valores de permissividade dos espalhadores. Além disso, simulações numéricas usando dados sintéticos mostram eficácia para reconstrução de imagens em problemas tridimensionais.

Palavras-chave: Equações integrais, Imageamento em micro-ondas, Métodos de gradiente conjugado, Problemas de espalhamento inverso, Reconstrução de imagens.

Abstract

The electromagnetic inverse scattering problem in microwave imaging aims to recover the dielectric properties, location, size, and shape of scatterers inside an inaccessible domain. This is an important field of electromagnetic wave applications, such as biomedical imaging, buried object detection, oil-gas exploration, and nondestructive evaluation. The imaging is performed by analyzing the scattered field measurements, which are usually cast into an optimization problem. In this context, an iterative inversion method is often required to minimize a cost function constructed by the mismatch of the measured scattered field and the computed one.

In this thesis, different efficient algorithms based on the conjugate gradient method (CGM) to solve two- and three-dimensional inverse scattering problems are presented. The inversion CGM requires the solution of the forward scattering problem and the calculation of the gradient direction of the cost function at each iteration step. Depending on the gradient approximation, the CGM can be classified into two main approaches, linearized and nonlinearized methods. Each computation of the forward problem can be very time-consuming. To avoid the computational burden, the forward solvers are efficiently implemented by using iterative methods to solve systems of simultaneous equations combined with FFT (fast Fourier transform) algorithms.

The inversion methods proposed in this thesis are based on conjugate gradient approaches. Firstly, an efficient implementation of the nonlinearized CGM is proposed, which does not require calculating the inverse matrix. Such an approach reduces the computational cost and storage requirement of the reconstruction algorithm compared to the original one. Secondly, a subspace-based CGM (S-CGM) is also proposed, which is based on the linearized CGM and the concept of subspaces. Lastly, we propose a fast CGM to solve inverse scattering problems with a low degree of nonlinearity. Several numerical simulations have been carried out to validate the proposed inversion algorithms. In the 2D case, the methods are tested against both synthetic and experimental data. The reconstruction results show effectiveness in estimating the location, object shape, and permittivity values of the scatterers. In addition, numerical simulations using synthetic data show effectiveness for image reconstruction in three-dimensional problems.

Keywords: Integral equations, Microwave imaging, Conjugate gradient methods, Inverse scattering problems, Image reconstruction.

List of Figures

List of Tables

List of Symbols

$\overline{E}$	Total electric field
$\overline{E}^{inc}$	Incident field vector
$\overline{E}^{sca}$	Scattered electric field
$\overline{J}$	Electric current density
$\delta\overline{J}^{d}$	Deterministic part of the variational induced current
$\overline{\rho}_l$	Residual error for each incidence
$\overline{d}$	Search direction vector
$\overline{g}$	Gradient vector
$\overline{\overline{G}}$	Dyadic Green's function
$\overline{\overline{I}}$	Identity matrix
$\overline{\overline{\chi}}$	Contrast matrix
$\mathbf{A}(\mathbf{r})$	Magnetic vector potential
$\mathbf{B}(\mathbf{r})$	Magnetic flux density
$\mathbf{D}(\mathbf{r})$	Electric flux density
$\mathbf{H}(\mathbf{r})$	Magnetic field
γ	Tikhonov regularization parameter
λ	Wavelength
μ	Permeability
μ_0	Vacuum permeability
ω	Angular frequency
σ	Electric conductivity
ε	Complex permittivity
ε_0	Vacuum permeability
c	Speed of light in a vacuum

k	Wavenumber
N	Number of cells
N_i	Number of incidences
N_r	Number of receivers
W	Weighting coefficient
j	Unit imaginary number $\sqrt{-1}$
ERR_ε	Permittivity profile error
$\overline{\overline{A}}^H$	Hermitian matrix
$\overline{\overline{A}}^T$	Transpose of the matrix $\overline{\overline{A}}$
$\overline{\overline{A}}^*$	Complex conjugate of the matrix $\overline{\overline{A}}$
$\langle a, b \rangle$	Inner product between a and b
$\| \cdot \|$	Euclidean norm

List of abbreviations and acronyms

2D	Two-dimensional
3D	Three-dimensional
AWGN	Additive white Gaussian noise
BA	Born approximation
BiCGSTAB	Biconjugate gradient stabilized
BIM	Born iterative method
BP	Back-propagation
CG	Conjugate gradient
CSI	Contrast source inversion
DBIM	Distorted Born iterative method
DGF	Dyadic Green's function
DOI	Domain of interest
DTA	Diagonal tensor approximation
EA	Evolutionary algorithm
EBA	Extended Born approximation
EFIE	Electric field integral equation
EM	Electromagnetic
FDM	Finite difference method
FEM	Finite element method
FFT	Fast Fourier transform
GA	Genetic algorithm
ISP	Inverse scattering problem
MoM	Method of moments

NDE	Nondestructive evaluation
NDT	Nondestructive testing
NK	Newton-Kantorovich
PSO	Particle swarm optimization
QA	Quasi-analytical
QL	Quasi-linear
RCS	Radar cross section
S-CGM	Subspace-based conjugate-gradient method
S-DBIM	Subspace-based Distorted Born Iterative Method
SOM	Subspace-based optimization method
S-VBIM	Subspace-based variational Born iterative method
STIE	Source-type integral equation
SVD	Singular value decomposition
TM	Transverse magnetic
TV	Total variation

Contents

1 Introduction

This chapter introduces the principles of the electromagnetic inverse scattering problems. A brief review of some inversion methods and their applications in microwave imaging problems is presented. A classification of the different algorithms, including the main challenges in solving the inverse problem, is discussed. The research motivation and the contributions of this thesis are presented. Finally, the work outline details the content of the following chapters.

1.1 Background

Electromagnetic inverse scattering in microwave imaging has increased interest in recent years. The inverse scattering problem (ISP) consists of recovering the dielectric properties, location, and shape of unknown objects from scattered field measurements under the illumination of incident electromagnetic (EM) waves. The research of microwave imaging techniques is motivated by their potential in a wide range of practical applications. For example, in biomedical imaging, the inverse scattering problem has been applied in microwave tomography (Abubakar; Van den Berg; Mallorqui, 2002; Abubakar et al., 2012) and breast cancer detection (Chandra et al., 2015). In nondestructive evaluation (NDE) or nondestructive testing (NDT), this is often used for crack detection in civil structures (Massa et al., 2006; Kharkovsky; Zoughi, 2007; Oliveri; Ding; Poli, 2015). In radar imaging, it is applied to detection and identification of targets, such as the through-wall imaging (Song; Yu; Liu, 2005; Xu et al., 2018). In geoscience, it is also used in subsurface prospecting (Persico, 2014). Due to all these important civil and military applications, it is essential to develop accurate and efficient methods to solve different ISPs.

In ISPs, the measured scattered field is linked to the electromagnetic properties of the objects by an integral or differential equation. Unfortunately, this problem is nonlinear and *ill-posed*; that is, the existence, uniqueness, and stability of the solution are not simultaneously guaranteed (Hadamard, 1923). Such features represent the major difficulty in solving inverse problems (Colton; Kress, 2019). The *ill-posedness* can be mitigated by using regularization strategies. For example, the Tikhonov regularization and singular value decomposition (SVD) have been widely used in solving inverse scattering problems (Abubakar; Van den Berg; Mallorqui, 2002; Mojabi; LoVetri, 2009; Liu; Wang; Heng, 2003; Chen, 2018). In most reconstruction algorithms, the cost function for the minimization procedure is generally constructed by the mismatch between the measured and predicted scattered field. One way to solve the inverse problem is to compute the forward problem at each iteration step of an optimization algorithm. However, this is often time-consuming.

The forward scattering problem is based on Maxwell's equations, which can be represented in differential or integral form.

Generally speaking, the formulation of the inverse scattering problem leads to a nonlinear equation. Optimization procedures to solve the inverse scattering problem can be classified into noniterative and iterative methods. First, noniterative methods have been developed for the reconstruction of weak scatterers or low contrasts, i.e., there is only a slight difference between the permittivity of the scatterer and the permittivity of the background medium. The most common noniterative methods are based on Born or Rytov type approximations (Pastorino, 2010). These approximations lead to a linear relationship between the measured scattered field and the unknown contrast. For example, in the Born approximation (BA) method the total electric field inside the object domain is replaced by the incident field. When this approximation is applied in the forward and inverse problems, the result is a linear system. However, this is only valid for weak scatterers and the size of scatterers cannot be much larger than the wavelength (Chen, 2018). In order to increase the range applicability, the extended Born approximation (EBA) method was developed by Habashy, Groom and Spies (1993). Other approximation methods have been proposed to extend the validity range of the original Born approximation method, such as the quasi-linear (QL) approximation, quasi-analytical (QA) approximation (Zhdanov; Fang; Hursán, 2000), and diagonal tensor approximation (DTA) (Song; Liu, 2004) methods. Alternatively, a noniterative method based on back-propagation (BP) scheme is proposed in Belkebir, Chaumet and Sentenac (2005), which works for the reconstruction of weak scatterers illuminated by arbitrary incident fields. Despite their limited application ranges, these noniterative methods are computationally efficient and can also be used as a starting point or initial guess for iterative inversion methods.

A second kind of methods are addressed to inverse scattering problems involving strong scatterers. These formulations of inverse problems include all the scattering phenomena and are capable of reconstructing any dielectric object with high resolution image in far field, using monochromatic waves, that is, only a single frequency data set (Cui et al., 2001). In the last decades, many iterative inversion methods have been developed. According to the optimization strategy adopted, they can be classified into two categories: deterministic and stochastic algorithms. The first category is based on local inversion techniques, such as the Gauss-Newton method (Abubakar et al., 2012; Mojabi; LoVetri, 2009), the Levenberg–Marquardt method (Franchois; Pichot, 1997), and the conjugate gradient method (CGM) (Harada et al., 1995; Lobel et al., 1996; Chaumet; Belkebir, 2009). The second one is based on global inversion techniques, such as the genetic algorithm (GA) (Pastorino; Massa; Caorsi, 2000; Massa et al., 2005), the particle swarm optimization (PSO) (Donelli; Massa, 2005; Donelli et al., 2009), and the evolutionary algorithms (EAs) (Rocca et al., 2009).

The deterministic optimization methods also include the Born iterative method (BIM) (Wang; Chew, 1989) and the distorted Born iterative method (DBIM) (Chew; Wang, 1990), that is proven to be equivalent to the Newton-Kantorovich (NK) method (Remis; van den Berg, 2000). These are referred to as field-type methods. In the BIM, the Green's function is fixed during the iterative procedure. Whereas in the DBIM, Green's function associated to inhomogeneous background medium is updated at each iteration. Usually, these iterative methods use some regularization procedure to solve the ill-posed system.

The main drawback of stochastic algorithms is their high computational cost. One way to speed up these algorithms is to use parallelization procedures (Caorsi et al., 2004). On the other hand, the main advantage of deterministic algorithms is their convergence speed. However, they are limited to a few scatterers and have difficulty dealing with high contrasts. Due to its computational efficiency and simplicity, deterministic algorithms could be applied in hybrid methods integrating deterministic and stochastic approaches. Some hybridization techniques can be found in chapter 8 of Pastorino (2010). Recently, deep learning schemes have also been used to solve the ISP (Li et al., 2019; Zhou et al., 2021). Compared to the conventional inversion methods, these methods present a better performance and are capable of recovering scatterers with higher contrast.

Alternatively, source-type inversion methods have also been developed for the reconstruction algorithms, such as the source type integral equation (STIE) method (Habashy; Oristaglio; Hoop, 1994), the contrast source inversion (CSI) method (Van den Berg; Kleinman, 1997), and its variant versions (Van den Berg; Van Broekhoven; Abubakar, 1999; Agarwal et al., 2013; Bevacqua et al., 2017). These methods do not need to solve the corresponding forward problem, since the cast optimization problem consists of two terms, the first is the mismatch in the data equation and the second one is the error in satisfying the state equation. The two residual errors need to be updated at each iteration of the optimization procedure. For example, the CSI uses the conjugate gradient (CG) method to alternately update the contrast and the contrast source. Recently, other more robust methods have also been proposed, such as the subspace-based optimization method (SOM) (Chen, 2018; Chen, 2010), which uses the spectral property of the mapping from the induced current to scattered fields. Some variations and improvements of the SOM are presented in Zhong, Chen and Agarwal (2010) and Zhong and Chen (2011). Moreover, the subspace concept of the SOM to calculate a deterministic part of the induced current has inspired other works, among them are the subspace-based distorted Born iterative method (S-DBIM) (Ye; Chen, 2017) and the subspace-based variational Born iterative method (S-VBIM) (Liu; Nie, 2019).

In this thesis, we will focus mainly in an efficient implementation of conjugate gradient-based methods. These inversion methods require the solution of both the forward problem and the calculation of the gradient direction of the cost function during the

optimization procedure. Consequently, the subject of this thesis is addressed to two ways: first, to investigate efficient procedures to speed up the forward solvers, so as to reduce the whole computational cost of image reconstruction; second, to investigate methods for solving ISPs for dielectric objects, which makes the optimization converge faster and obtain a better image reconstruction.

1.2 Inverse Scattering Problem

In a broad sense, the forward or direct problem is commonly a problem of modeling some physical system or phenomena. The goal of solving a forward problem is to find measured data from parameters of a given model. The opposite problem is called the inverse problem. As shown in Figure 1, an inverse problem intend to obtain information about the model from observed measurements.

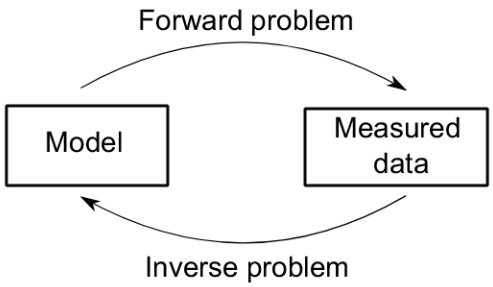

Figure 1 – Simple illustration of a forward and inverse problem.

From a mathematical form, we consider that if $Af = g$ is a forward problem and $A^{-1}g = f$ is the corresponding inverse problem, then g will be considered to be the data on the basis of which the object properties f are to be inferred (Roy; Couchman, 2001). In this work, the forward problem is related to calculation of the scattered field by an arbitrary dielectric object (where the object properties are known), whereas the inverse problem consists on the determination of the object or scatterer from the field scattered data. Figure 2 shows two different configurations of inverse scattering problems, which are often used for two- and three-dimensional imaging. An inhomogeneous scatterer is embedded in the rectangular domain D, which is also called the domain of interest (DOI). The transmitter-receiver array can be placed on coaxial circles (domain S) surrounding the object domain D. In general, the goal of inverse scattering problems is to recover characteristics of unknown objects by analyzing scattered field measurements. Other imaging configurations and models of inverse scattering problems can be found in chapter 4 of Pastorino (2010).

One of the most critical aspect in solving inverse problems is usually its ill-posedness. In the sense of Hadamard, a problem is well-posed if its solution exits, is unique, and is stable with respect to data, that is, depends continuously on the data (Hadamard, 1923). If

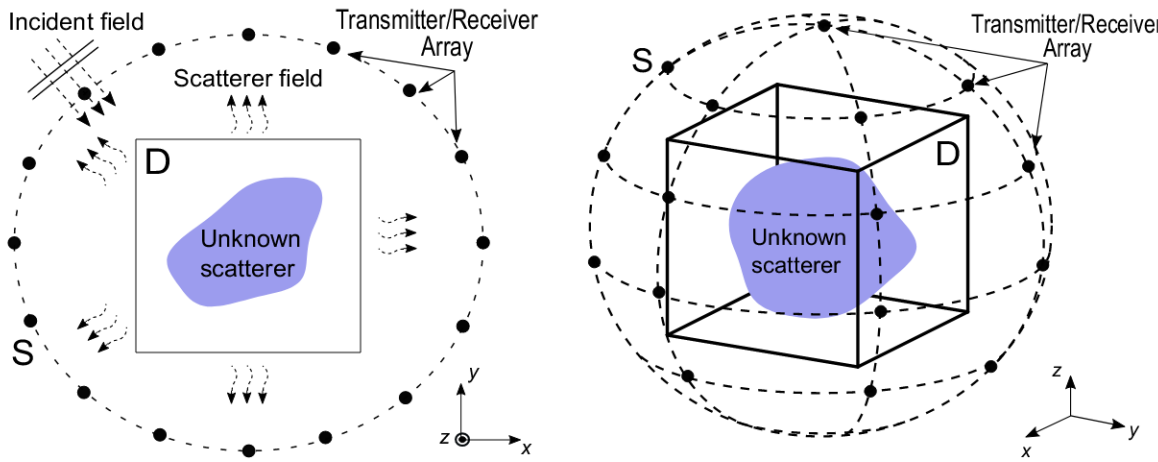

Figure 2 – Configuration of inverse scattering problems. (a) 2D geometry. (b) 3D geometry.

any of these conditions is not satisfied, the problem is called ill-posed. An ill-posed problem can become well-posed basically in two ways, either by restricting the set of the admissible solutions when a *priori* information is available, or by projecting the approximate data on the range of an unperturbed operator, and then inverting these processed data (Roy; Couchman, 2001). It is assumed that the restricted set or space of admissible solutions contains the true solution. The study of ill-posedness is an important issue for the solution of the inverse problem because an inverse problem cannot be solved experimentally (Glasko, 1984). Then an inversion procedure or reconstruction algorithm must be provided.

For electromagnetic waves, the uniqueness of the ISPs has been proved by Colton and Päivärinta (1992). Under certain conditions, for a fixed wavenumber, all directions of incidence, and all polarizations of the incident wave, the knowledge about the electric far field pattern for all angles uniquely determines the permittivity. Regarding stability, an ISP involving dielectric scatterers cannot be stably solved. In fact, even if the amount of collected data is sufficient to guarantee uniqueness, the unknowns usually do not depend on the measured data in a stable way (Chen, 2018). In practice, the data are often contaminated with noise or measurement errors. For an ill-posed problem a small error in the measured data results in a large error in the solution. However, restrictions in the space of admissible unknowns by assuming that they satisfy some a *priori* information, guarantee that the unknowns depend continuously on the measured data.

The focus of this thesis is to reconstruct the permittivity profile of dielectric scatterers by using quantitative reconstruction algorithms. Specifically, the scatterers are assumed to be nonmagnetic, that is, the relative permeability is $\mu_r = 1$, and have complex relative permittivity satisfying: $1 \leq \mathcal{R}(\varepsilon_r) < \infty$ and $|\mathcal{I}(\varepsilon_r)| \geq 0$. In addition, the scatterers have dimensions comparable to or larger than the wavelength.

1.3 Motivations and Contributions

1.3.1 Motivations

The conjugate gradient method (CGM) is a powerful deterministic technique for solving nonlinear optimization problems, such as the electromagnetic ISP. This method requires the solution of both the forward problem and the calculation of the gradient direction of the cost function during the optimization procedure. There are two main approaches: linearized and nonlinearized methods. In the first approach, the total electric field is assumed to be independent of the optimization variable, e.g., the unknown contrast (Chaumet; Belkebir, 2009). Therefore, the linearized CGM simplifies the gradient computation at each iteration step, since it only needs to solve a forward problem to obtain the gradient of the cost function. The second approach considers the total electric field as an additional parameter to calculate the gradient direction. Consequently, this leads to a nonlinear relation between the scattered field and the contrast (Lobel et al., 1996). Moreover, the nonlinearized approach needs to solve multiple scattering forward problems. One of the advantages of the CGM is that it works without any regularization scheme, e.g., Tikhonov regularization, even for moderate noise levels in the scattered data. Compared with the nonlinear inversion CGM, the linearized inversion CGM is less time-consuming. However, when the ISP is highly nonlinear, it fails to retrieve the scatterers.

The original nonlinearized CGM version needs a matrix inversion, which is used to solve the forward problem and calculate the gradient direction. Due to the multiple forward problems the computational cost and memory storage overhead in the computation of the gradient direction are very expensive. Furthermore, the original CGM (Lobel et al., 1996) has been little explored in inverse scattering applications in recent years. Motivated by the limitations of both linearized and nonlinearized CGM inversion approaches, this thesis proposes fast and efficient procedures for the implementation of inversion algorithms based on CGM. The inversion methods discussed in this thesis are based on the electric field integral equation (EFIE), and the method of moments (MoM) is used for the forward problem model. An alternative to EFIE formulations is solving the partial differential equation using differential equation formulations, such as the finite-difference method (FDM) or the finite element method (FEM). While differential equation formulations, such as the FDM, are most easily employed in the solution of closed domain electromagnetic problems, open domain problems with the knowledge of Green's function are well suited to discretization by the MoM. Solving integral equations using MoM produces a dense system of equations. However, the matrix associated with the integral equations has a *Toeplitz* structure (Vogel, 2002). Toeplitz matrices are matrices having constant entries along their diagonals. This convolutional structure leads to the implementation of more efficient algorithms in both two- and three-dimensional scattering problems.

In this context, the motivation of this work is mainly to investigate an alternative way to implement efficient conjugate gradient-based methods. For example, iterative methods to solve systems of simultaneous equations combined with FFT algorithms can be used to accelerate the computation of both the forward problem and the gradient direction of the cost function at each iteration. These reconstruction algorithms could be applied to any kind of lossy dielectric scatterer, even for large domain discretizations.

Furthermore, new approximations of the total electric field are also important to achieve faster convergence speed and higher accuracy, as well as extend inversion methods to three-dimensional problems.

1.3.2 Contributions

The contributions of the thesis consist of two main parts: an efficient implementation of the CGM and a new CGM based on the subspace concept for solving ISPs. The original contributions are listed as follows.

- Proposal of an efficient implementation of a CGM for solving electromagnetic ISPs, which is independent of a regularization parameter. For 2D ISPs, the forward problem and gradient direction can be efficiently calculated by using CG-FFT procedures, whereas the BiCGSTAB-FFT procedure is used to solve the forward problems in 3D ISPs.

- Comparison of the computational cost and the storage requirements of the CGM implementations. As a consequence, the computational complexity of the efficient CGM (nonlinearized CGM approach) is found to be similar to that of the DBIM.

- Proposal of a subspace-based conjugate-gradient method (S-CGM) for solving electromagnetic ISPs. It updates the total field with the addition of the deterministic part of the variational induced current instead of only the total field of the previous iteration. This new approach achieves a better convergence speed and higher accuracy solution than the original linearized CGM approach.

- Proposal of a fast forward-solver scheme based on inverse matrix approximation and recursive approaches for updating the fields at each iteration within the CGM. Under certain conditions, the solution converges and can improve the computational efficiency of the CGM. In particular, the proposed fast CGM provides an accurate solution to low-degree nonlinearity problems. In addition, this approximation is very low computational complexity.

1.4 Thesis Organization

This thesis is organized in six chapters, including this one. Chapter 2 contains the principles of the forward scattering problem. Integral equations and discretization of the two- and three-dimensional continuous models are presented. The application of the iterative methods combined with FFT algorithms for solving the equation system derived from the integral equations is described here. In Chapter 3 the proposed inversion algorithms based on the conjugate gradient methods are introduced. The results of image reconstruction in 2D problems are presented in Chapter 4 and 3D inversion results are presented in Chapter 5. Finally, Chapter 6 presents the conclusions and future research work.

2 Forward Problem

This chapter contains the foundation of electromagnetic theory. Here the electromagnetic scattering problem is governed by the electric field integral equation (EFIE). Mathematical formulation and numerical examples of the EFIE for 2D and 3D scattering problems are presented. In addition, some approaches for solving linear equation systems are provided, which can be applied in later chapters.

2.1 Maxwell's Equations

The electromagnetic field is governed by Maxwell's equations. The time-harmonic forms of Maxwell's equations in differential form can be written as

$$\nabla \times \mathbf{E}(\mathbf{r}) = -j\omega\mathbf{B}(\mathbf{r}), \tag{2.1}$$

$$\nabla \times \mathbf{H}(\mathbf{r}) = j\omega\mathbf{D}(\mathbf{r}) + \mathbf{J}(\mathbf{r}), \tag{2.2}$$

$$\nabla \cdot \mathbf{D}(\mathbf{r}) = \rho(\mathbf{r}), \tag{2.3}$$

$$\nabla \cdot \mathbf{B}(\mathbf{r}) = 0, \tag{2.4}$$

where $\mathbf{r}$ denotes the position vector in meters. $\mathbf{E}$, $\mathbf{H}$, $\mathbf{D}$, $\mathbf{B}$, $\mathbf{J}$ and ρ are the corresponding complex spatial quantities (Balanis, 1989). $\mathbf{E}$ is the electric field intensity (V/m), $\mathbf{H}$ is the magnetic field intensity (A/m), $\mathbf{D}$ is the electric flux density ($\mathrm{C/m^2}$), $\mathbf{B}$ is the magnetic flux density (T), $\mathbf{J}$ is the electric current density ($\mathrm{A/m^2}$), and ρ is the volume electric charge density ($\mathrm{C/m^3}$).

Note that all the equations above present both space and time dependency, here the time derivatives are replaced by the factor $j\omega$. Throughout this work, the time dependence is assumed to be $e^{j\omega t}$, where ω and t are the angular frequency and time, respectively, and j represents the unit imaginary number ($j = \sqrt{-1}$). In addition to Maxwell's equations, the continuity equation is given by

$$\nabla \cdot \mathbf{J}(\mathbf{r}) = -j\omega\rho(\mathbf{r}). \tag{2.5}$$

In discontinuous media, boundary conditions for solving Maxwell's equations are needed. Considering two different media denoted as medium 1 and medium 2, in which

the normal $\hat{\mathbf{n}}$ of the boundary pointing from medium 1 into medium 2. The boundary conditions become

$$\hat{\mathbf{n}} \times (\mathbf{H}_2 - \mathbf{H}_1) = \mathbf{J}_s, \tag{2.6}$$

$$\hat{\mathbf{n}} \times (\mathbf{E}_2 - \mathbf{E}_1) = 0, \tag{2.7}$$

$$\hat{\mathbf{n}} \cdot (\mathbf{D}_2 - \mathbf{D}_1) = \rho_s, \tag{2.8}$$

$$\hat{\mathbf{n}} \cdot (\mathbf{B}_2 - \mathbf{B}_1) = 0, \tag{2.9}$$

where subscripts 1 and 2 indicate the EM fields in medium 1 and medium 2, respectively. $\mathbf{J}_s$ is the surface electric current density (A/m) and ρ_s is the surface charge density (C/m^2).

2.2 Electric Field Integral Equation

The electric field integral equation (EFIE) is formulated from the principle of linear superposition and the volume equivalence theorem. In the superposition principle, the total field can be determined by the sum of the incident field and scattered field, and the volume equivalence theorem consists of introducing an equivalent current density to relate the total field to the electromagnetic properties of the object.

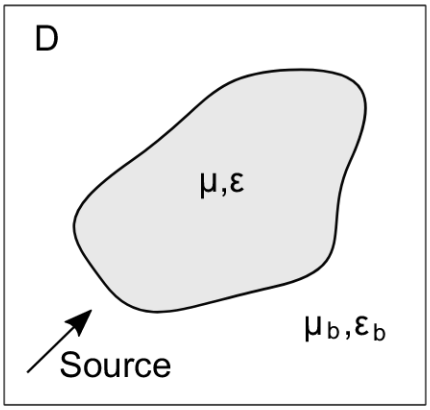

Figure 3 – A dielectric scatterer embedded in a homogeneous background medium.

2.2.1 Volume equivalence theorem

Consider an arbitrary scatterer embedded in a homogeneous background medium, as shown in Figure 3, which has a complex permittivity ε and permeability μ. The bounded homogeneous background medium is characterized by ε_b and μ_b. The scatterer is illuminated by an incident wave (primary source) located in the background medium.

In the volume equivalence theorem, the original scattering problem is replaced by an equivalent problem. Here the dielectric properties and the total fields inside the scatterer are related by equivalent sources. To obtain this relationship, consider Maxwell's equations in the presence of the scatterer

$$\nabla \times \mathbf{E} = -j\omega\mu\mathbf{H}, \tag{2.10}$$

$$\nabla \times \mathbf{H} = j\omega\varepsilon\mathbf{E}. \tag{2.11}$$

Now, consider Maxwell's equations in the absence of the scatterer, that is, the background fields are denoted by

$$\nabla \times \mathbf{E}_b = -j\omega\mu_b\mathbf{H}_b, \tag{2.12}$$

$$\nabla \times \mathbf{H}_b = j\omega\varepsilon_b\mathbf{E}_b. \tag{2.13}$$

From the total fields we have to $\mathbf{E} = \mathbf{E}_b + \mathbf{E}_s$ and $\mathbf{H} = \mathbf{H}_b + \mathbf{H}_s$, where the subscript s denotes the scattered fields. By using Equations (2.10) to (2.13), we found the equivalent sources

$$\mathbf{J} = j\omega(\epsilon - \epsilon_b)\mathbf{E}, \tag{2.14}$$

$$\mathbf{M} = j\omega(\mu - \mu_b)\mathbf{H}. \tag{2.15}$$

Note that $\mathbf{M}$ is mathematically equivalent to the magnetic current density, but it does not exist physically.

Due to the superposition principle, it is possible to determine the radiation in the background medium from a current density. We consider the situation where only electric current density exists in the homogeneous background. From Maxwell's equations we have

$$\nabla \times \mathbf{E}(\mathbf{r}) = -j\omega\mu_b\mathbf{H}(\mathbf{r}), \tag{2.16}$$

$$\nabla \times \mathbf{H}(\mathbf{r}) = j\omega\varepsilon_b\mathbf{E}(\mathbf{r}) + \mathbf{J}(\mathbf{r}). \tag{2.17}$$

By taking the curl of Equation (2.16) and replacing the result in Equation (2.17), we obtain the vector wave equation

$$\nabla \times \nabla \times \mathbf{E}(\mathbf{r}) - k_b^2\mathbf{E}(\mathbf{r}) = -j\omega\mu_b\mathbf{J}(\mathbf{r}), \tag{2.18}$$

where $k_b = \omega\sqrt{\mu_b \varepsilon_b}$ is the background wavenumber. The radiation field generated by an arbitrary electric current distribution $\mathbf{J}(\mathbf{r})$ can be formulated by the following integral

$$\mathbf{E}(\mathbf{r}) = j\omega\mu_b \iiint \overline{\overline{G}}(\mathbf{r}, \mathbf{r}') \cdot \mathbf{J}(\mathbf{r}') d\mathbf{r}', \tag{2.19}$$

where $\overline{\overline{G}}(\mathbf{r}, \mathbf{r}')$ is the dyadic Green's function given by

$$\overline{\overline{G}}(\mathbf{r}, \mathbf{r}') = -\left[\overline{\overline{I}} + \frac{1}{k_b^2}\nabla\nabla\right] g(\mathbf{r}, \mathbf{r}'), \tag{2.20}$$

where $\overline{\overline{I}}$ is an identity matrix, and the scalar Green's function $g(\mathbf{r}, \mathbf{r}')$ satisfies the following differential equation

$$\left(\nabla^2 - k_b^2\right) g(\mathbf{r}, \mathbf{r}') = \delta(\mathbf{r}, \mathbf{r}'). \tag{2.21}$$

The $g(\mathbf{r}, \mathbf{r}')$ is related to an impulse response function, and the corresponding expression in three dimensions is given by

$$g(\mathbf{r}, \mathbf{r}') = \frac{e^{-jk_b|\mathbf{r}-\mathbf{r}'|}}{4\pi\,|\mathbf{r} - \mathbf{r}'|}. \tag{2.22}$$

2.2.2 Volume scattering by dielectric scatterers

From the relationship between the scattered fields and induced currents, (2.10) to (2.13), we can be expressed the scattering problem in integral form as

$$\mathbf{E}(\mathbf{r}) - \mathbf{E}^{inc}(\mathbf{r}) = j\omega\mu_0 \iiint \overline{\overline{G}}(\mathbf{r}, \mathbf{r}') \cdot \mathbf{J}(\mathbf{r}') d\mathbf{r}' + \iiint \left[\nabla \times \overline{\overline{G}}(\mathbf{r}, \mathbf{r}')\right] \cdot \mathbf{M}(\mathbf{r}') d\mathbf{r}'. \tag{2.23}$$

The equivalent sources $\mathbf{J}$ and $\mathbf{M}$ depend on the dielectric properties of the scatterer and the total electric field. In this work, we assume nonmagnetic scatterers, that is, the permeability of the background is equal to the vacuum permeability ($\mu_b = \mu_0$), then the equivalent magnetic current is eliminated, and the electric field integral equation (EFIE) is defined as

$$\mathbf{E}(\mathbf{r}) - \mathbf{E}^{inc}(\mathbf{r}) = j\omega\mu_0 \iiint \overline{\overline{G}}(\mathbf{r}, \mathbf{r}') \cdot \mathbf{J}(\mathbf{r}') d\mathbf{r}'. \tag{2.24}$$

In the forward scattering problem, the only unknown in Equation (2.24) is the total electric field $\mathbf{E}(\mathbf{r})$ and the equivalent electric current distribution is given by

$$\mathbf{J}(\mathbf{r}) = j\omega\left[\varepsilon(\mathbf{r}) - \varepsilon_b\right]\mathbf{E}(\mathbf{r}). \tag{2.25}$$

For convenience, the current density $\mathbf{J}(\mathbf{r})$ can be written as an induced contrast current by using contrast function $\chi(\mathbf{r})$

$$\mathbf{J}(\mathbf{r}) = j\omega\varepsilon_b\chi(\mathbf{r})\mathbf{E}(\mathbf{r}), \tag{2.26}$$

where the contrast function is given by

$$\chi(\mathbf{r}) = \frac{\varepsilon(\mathbf{r})}{\epsilon_b} - 1, \tag{2.27}$$

and

$$\varepsilon(\mathbf{r}) = \varepsilon_0\ \varepsilon_r(\mathbf{r}), \tag{2.28}$$

$$\varepsilon_b = \varepsilon_0\ \varepsilon_{rb}. \tag{2.29}$$

Subscript b in the equations above denotes the background medium and ε_0 is the vacuum permittivity. In inverse scattering problems, we assume that the inhomogeneous dielectric scatterer is characterized by the relative complex permittivity $\varepsilon_r(\mathbf{r})$, and the homogeneous background medium is known and is characterized by the relative complex permittivity ε_{rb}. The complex permittivity is expressed as

$$\varepsilon(\mathbf{r}) = \varepsilon_0\left[\varepsilon_r(\mathbf{r}) - j\frac{\sigma(\mathbf{r})}{\omega\varepsilon_0}\right] = \varepsilon_0\left[{\varepsilon_r}'(\mathbf{r}) - j{\varepsilon_r}''(\mathbf{r})\right], \tag{2.30}$$

where $\sigma(\mathbf{r})$ is the electric conductivity (S/m) of the scatterer.

Finally, substituting the Equation (2.26) in Equation (2.24), we have

$$\mathbf{E}(\mathbf{r}) = \mathbf{E}^{inc}(\mathbf{r}) + k_b^2\iint\overline{\overline{G}}(\mathbf{r},\mathbf{r}')\cdot\chi(\mathbf{r}')\mathbf{E}(\mathbf{r}')d\mathbf{r}'. \tag{2.31}$$

2.3 Two-Dimensional Scattering Problems

The scattering formulation presented in the previous section concerns general three-dimensional problems. In some special cases, the three-dimensional problem can be simplified to a two-dimensional problem by assuming parameters invariant in a spatial coordinate. Throughout this work, we assume 2D domain objects invariant along the z-axis. With this assumption, the cross section of the arbitrary cylinder (scatterer) is a function of x and y. In addition, if illuminated by an incident field which is polarized in the z-direction; that is, transverse magnetic (TM) field, the z component of the electric current density $\mathbf{J}$ generates the TM field component, $\mathbf{E}_z$. Consequently, the Equation (2.31) is reduced to

$$\mathbf{E}_z(\mathbf{r}) = \mathbf{E}_z^{inc}(\mathbf{r}) + k_b^2 \iint g(\mathbf{r}, \mathbf{r}') \cdot \chi(\mathbf{r}') \mathbf{E}_z(\mathbf{r}') d\mathbf{r}', \tag{2.32}$$

where

$$g(\mathbf{r}, \mathbf{r}') = \frac{1}{4j} H_0^{(2)} \left(k_b \left| \mathbf{r} - \mathbf{r}' \right| \right), \tag{2.33}$$

is the scalar Green's function for two-dimensional problems, where $H_0^{(2)}$ is the Hankel function of zeroth order and second kind. $\mathbf{E}_z^{inc}(\mathbf{r})$ denotes the known incident field, and the distance between the observation point $\mathbf{r} = (x, y)$ and the source point $\mathbf{r}' = (x', y')$ is calculated by

$$|\mathbf{r} - \mathbf{r}'| = \sqrt{(x - x')^2 + (y - y')^2}. \tag{2.34}$$

2.3.1 Method of moments

In most EM problems the resulting equations cannot be solved analytically. Therefore it is necessary to reformulate the equations by using some numerical method to obtain an approximation to the solution. In this work, we use the method of moments (MOM), which is a general procedure for approximating linear equations. Here, the MoM is used to approximate the solution of the EFIE, which results in a linear system that can be solved by an iterative method.

Consider the inhomogeneous equation (Harrington, 1968)

$$L(f) = g, \tag{2.35}$$

where L is a linear operator, typically is an integral or integro-differential, g is the known excitation or source function (incident field) and f is the unknown function (field or current) to be determined. The MoM starts by expanding the function f into a series of known *expansion* or *basis functions*, $f_1, f_2, \cdots, f_N$ in the domain of L, as follows

$$f = \sum_{n=1}^{N} \alpha_n f_n, \tag{2.36}$$

where α_n are expansion coefficients to be determined. Since L is linear, substitution of (2.36) into (2.35) yields

$$\sum_{n=1}^{N} \alpha_n L(f_n) \approx g. \tag{2.37}$$

Introducing the *weighting functions* or *testing functions* $w_1, w_2, \cdots, w_N$, and taking the inner product of the Equation (2.37) with each w_m, produces

$$\sum_{n=1}^{N} \alpha_n \langle w_m, Lf_n \rangle = \langle w_m, g \rangle \qquad \text{for } m = 1, 2, ..., N. \tag{2.38}$$

The set of equations in (2.38) can be written in matrix form as

$$\begin{bmatrix} Z_{11} & Z_{12} & \cdots & Z_{1N} \\ Z_{21} & Z_{22} & \cdots & Z_{2N} \\ \vdots & \vdots & \cdots & \vdots \\ Z_{N1} & Z_{2N} & \cdots & Z_{NN} \end{bmatrix} \begin{bmatrix} \alpha_1 \\ \alpha_2 \\ \vdots \\ \alpha_N \end{bmatrix} = \begin{bmatrix} \langle w_1, g \rangle \\ \langle w_2, g \rangle \\ \vdots \\ \langle w_N, g \rangle \end{bmatrix} \tag{2.39}$$

or written in compacted form

$$[\mathbf{Z}]\,[\alpha] = [\mathbf{b}]\,, \tag{2.40}$$

where $Z_{mn} = \langle w_m, L(f_n) \rangle$, $b_m = \langle w_m, g \rangle$, and the vector α contains the unknown coefficients. We define an inner product $\langle w, g \rangle$ as

$$\langle w, g \rangle = \iint_D w \cdot g^* dD, \tag{2.41}$$

where w is the testing or weighting function, g is the function being tested, D is the domain of w and g, and the superscript * denotes the complex conjugate operator.

The system of linear equations in (2.40) can be solved by direct or iterative methods. This completes the MoM procedure. The accuracy of the solution to Equation (2.40) depends on the choice of f_n and w_n. A common choice is that the same basis functions are used as testing functions, that is, $w_n = f_n$. This procedure is known as *Galerkin's* method (Harrington, 1968). Another way is to ensure that Equation (2.37) is satisfied at discrete points in the domain of interest. This method is called *matching point* (Harrington, 1968), which is equivalent to using a delta function as the weighting function in evaluating $Z_{mn} = \langle w_m, L(f_n) \rangle$ with

$$w_m(\mathbf{r}) = \delta(\mathbf{r}). \tag{2.42}$$

The characteristic of the basis function f_n is useful to represent the behavior of the unknown function in a domain of interest. Moreover, the complexity of evaluating matrix elements also depends on the choice of the basis functions. Local basis functions are commonly used in MoM, this approximation is referred to as the *method of subsections* (Harrington, 1968).

2.3.2 Discretization of the EFIE

Consider a two-dimensional scattering problem configuration under TM illumination, which is formulated by the Equation (2.32). In order to apply MoM, the domain D is discretized into N small square cells, as shown in Figure 4. Moreover, assume that $\chi(\mathbf{r})$ and $E^{inc}(\mathbf{r})$ are constant in each cell.

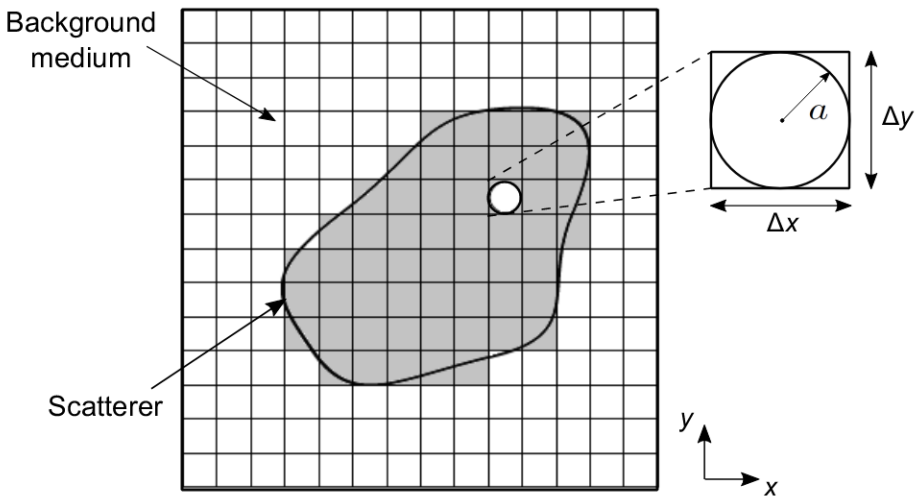

Figure 4 – 2D discretization of the domain of interest.

Therefore, we discrete the domain of interest into $N = N_x \times N_y$ cells with spatial coordinate centers located at

$$\begin{aligned} x &= x_{\min} + \left(i - \tfrac{1}{2}\right)\Delta x \qquad \text{for} \quad i = 1, 2, ..., N_x \\ y &= y_{\min} + \left(j - \tfrac{1}{2}\right)\Delta y \qquad \text{for} \quad j = 1, 2, ..., N_y \end{aligned}, \tag{2.43}$$

where

$$\Delta x = \frac{x_{\max} - x_{\min}}{N_x}, \quad \Delta y = \frac{y_{\max} - y_{\min}}{N_y}. \tag{2.44}$$

Applying the pulse basis function and point matching technique

$$f_n(\mathbf{r}) = \begin{cases} 1 & \text{if } \mathbf{r} \in \text{cell } n \\ 0 & \text{otherwise} \end{cases} \tag{2.45}$$

and expanding the unknown total electric field inside the domain of interest

$$E_z(\mathbf{r}) \cong \sum_{n=1}^{N} E_n f_n(\mathbf{r}), \tag{2.46}$$

where E_n are coefficients to be determined. Then, the Equation (2.32) can be rewritten as

$$E^{inc}(\mathbf{r}) \cong \sum_{n=1}^{N} E_n \left\{ f_n - k_b^2 \iint\limits_{cell\ n} \frac{1}{4j} H_0^{(2)}\left(k_b \left|\mathbf{r}-\mathbf{r}'\right|\right) \chi(\mathbf{r}')\ d\mathbf{r}' \right\}. \tag{2.47}$$

Enforcing (2.47) at the center of each of the N cells, we obtain the following matrix system

$$\begin{bmatrix} E_1^{inc} \\ E_2^{inc} \\ \vdots \\ E_N^{inc} \end{bmatrix} = \begin{bmatrix} Z_{11} & Z_{12} & \cdots & Z_{1N} \\ Z_{21} & Z_{22} & \cdots & Z_{2N} \\ \vdots & \vdots & \cdots & \vdots \\ Z_{N1} & Z_{2N} & \cdots & Z_{NN} \end{bmatrix} \begin{bmatrix} E_1 \\ E_2 \\ \vdots \\ E_N \end{bmatrix} \tag{2.48}$$

where the matrix elements are given by

$$Z_{mn} = -\frac{k_b^2}{4j} \iint\limits_{cell\ n} H_0^{(2)}\left(k_b R_m\right) \boldsymbol{\chi}_n\ d\mathbf{r}' \quad m \neq n \tag{2.49}$$

$$Z_{mm} = 1 - \frac{k_b^2}{4j} \iint\limits_{cell\ m} H_0^{(2)}\left(k_b R_m\right) \boldsymbol{\chi}_m\ d\mathbf{r}', \tag{2.50}$$

where

$$R_m = \sqrt{(x_m - x')^2 + (y_m - y')^2}. \tag{2.51}$$

To evaluate integrals (2.49) and (2.50) in closed-form, square cells are approximated by a circle of radius a centered at $\mathbf{r}_n$ (Richmond, 1965), as shown in Figure 4. Using integrals in cylindrical coordinates, we introduce the Green's function operator

$$G_{mn} = \frac{k_b^2}{4j} \int_0^{2\pi} \int_0^{a} H_0^{(2)}(k_b \left|\mathbf{r}-\mathbf{r}'\right|) \rho' d\rho' d\phi'. \tag{2.52}$$

For convenience, we rewritten the system of linear equations in compact form

$$\overline{E}^{inc} = \overline{\overline{Z}} \cdot \overline{E} = \left(\overline{\overline{I}} - \overline{\overline{G}} \cdot \overline{\overline{\chi}}\right) \cdot \overline{E}, \tag{2.53}$$

where $\overline{E}^{inc}$ is the $N \times 1$ incident field vector, $\overline{E}$ is the $N \times 1$ total electric field vector, $\overline{\overline{I}}$ is the $N \times N$ identity matrix, $\overline{\overline{\chi}}$ is the diagonal contrast matrix containing χ_n, and the $N \times N$ matrix $\overline{\overline{G}}$ represents the dyadic Green's function, which has the following entries

$$G_{mn} = \begin{cases} \frac{\pi k_b a}{2j} J_1(k_b a) H_0^{(2)}(k_b R_{mn}) & \text{for } m \neq n \\ \\ \frac{\pi k_b a}{2j} H_1^{(2)}(k_b a) - 1 & \text{for } m = n \end{cases}, \tag{2.54}$$

where $J_1(\cdot)$ is the first order Bessel function, $H_1^{(2)}(\cdot)$ is the first order Hankel function of the second kind, and a is the radius of the circle of area equivalent to the square cell, that is

$$a = \sqrt{\frac{\Delta x \Delta y}{\pi}} \tag{2.55}$$

and

$$R_{mn} = \sqrt{(x_m - x_n)^2 + (y_m - y_n)^2}. \tag{2.56}$$

Note that the accuracy of the numerical solution is determined by the number of cells in the domain. As a rule of thumb, the maximum length of one side of each square cell is no larger than one-tenth of the wavelength of the dielectric medium inside the cell (Peterson; Ray; Mittra, 1998); that is, Δx can be defined as

$$\Delta x \leq \frac{1}{10} \frac{\lambda_0}{\sqrt{|\varepsilon_r|}}, \tag{2.57}$$

where λ_0 is the wavelength in free space.

It is important to mention that the matrix $\overline{\overline{G}}$ is dense and has a *Toeplitz* (or block Toeplitz) structure (Vogel, 2002). The Toeplitz pattern in two-dimensional problems is shown in Figure 5, the structure inherent in the matrix $\overline{\overline{G}}$ leads to the implementation of efficient algorithms (Peterson; Ray; Mittra, 1998; Su, 1987; Barrowes; Teixeira; Kong, 2001).

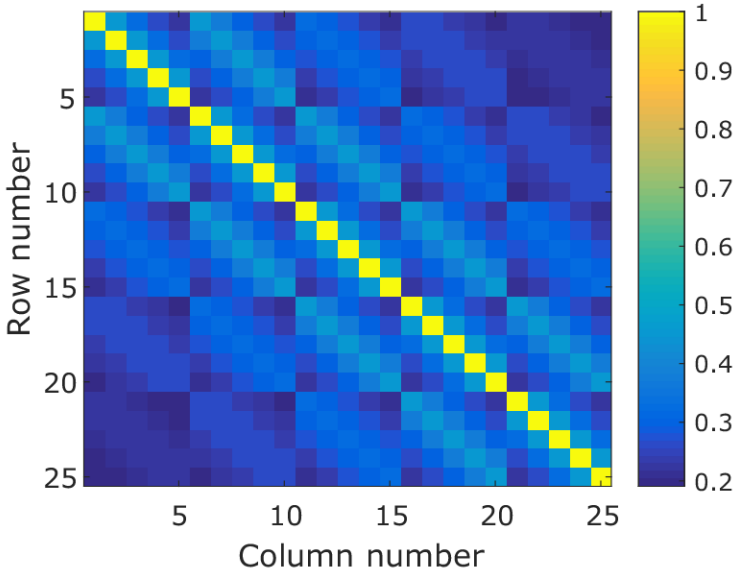

Figure 5 – Toeplitz structure of the 2D dense matrix.

For the example in Figure 5, the discretized domain is $N = N_x \times N_y$ (5×5 cells), then the dense matrix $\overline{\overline{G}}$ is size $N \times N$ (25×25 cells). This matrix can be described only by the entries in the first row $\overline{\overline{G}}_{1\times N}$. Accordingly, we extend the domain of interest as follows

$$\begin{aligned} x &= x_{\min} + \left(\tfrac{N_x}{2} - i'\right)\Delta x \qquad \text{for} \quad i' = 1, 2, ..., 2N_x - 1 \\ y &= y_{\min} + \left(\tfrac{N_y}{2} - j'\right)\Delta y \qquad \text{for} \quad j' = 1, 2, ..., 2N_y - 1 \end{aligned} \quad . \tag{2.58}$$

Then the nonredundant matrix entries are converted to a 2D matrix of size $(2N_x - 1) \times (2N_y - 1)$. Figure 6 shows the rearranged matrix $\overline{\overline{G}}'$ for two-dimensional discrete convolution. In this case, the corresponding matrix is size $(2N_x - 1) \times (2N_y - 1)$ (9×9 cells), which evidently reduces memory storage, especially for large-scale problems. Instead of storing the whole matrix $\overline{\overline{G}}$, the convolutional kernels of the integral equations can be performed in $O(N \log N)$ operations using FFT algorithms (Peterson; Ray; Mittra, 1998). The next two subsections introduce efficient procedures for the solution of the matrix system in (2.53).

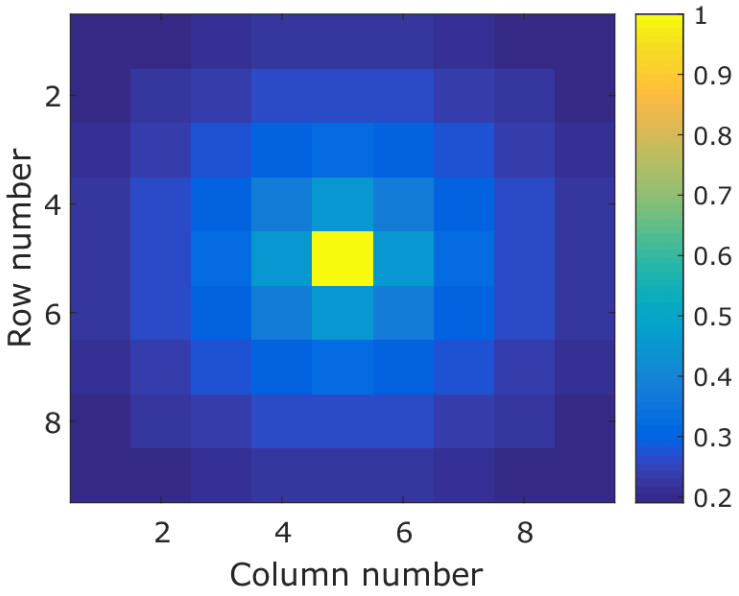

Figure 6 – Kernel for 2D discrete convolution procedure.

2.3.3 Conjugate gradient method

The linear system resulting from the EFIE can be solved by iterative methods, such as the conjugate gradient (CG) method. Due to the *Toeplitz* structure of the matrix $\overline{\overline{G}}$, it is possible to use the discrete convolution theorem and the fast Fourier transform algorithm (FFT) to perform matrix-vector multiplications. The CG-FFT procedure has been widely used to solve matrix systems in electromagnetic problems involving integral equations (Sarkar; Arvas; Rao, 1986; Peterson; Ray; Mittra, 1998; Su, 1987; Catedra; Gago, 1990; Shi; Liang, 2007).

The conjugate gradient (CG) algorithm is an iterative method for solving matrix systems. The CG method is a procedure to minimize an error function by using a sequence of conjugate directions, which reduces to the process of generating the orthogonal vectors and finding the proper coefficients to construct the desired solution (Peterson; Ray; Mittra, 1998).

Consider the linear equation system

$$\mathbf{A}\mathbf{x} = \mathbf{b}, \tag{2.59}$$

where $\mathbf{A}$ denotes an $N \times N$ matrix, $\mathbf{x}$ is an unknown column vector of $N \times 1$, and $\mathbf{b}$ is a $N \times 1$ given column vector, or right-hand side. The error functional can be presented as

$$F(\mathbf{x}) = \|\mathbf{A}\mathbf{x} - \mathbf{b}\|^2, \tag{2.60}$$

where $\|\cdot\|^2$ is the Euclidean norm. The conventional CG method is restricted to the special case of a Hermitian positive-definite matrix $\mathbf{A}$. In order to apply the CG method to arbitrary linear systems, we employ the so-called normal equations, as follows

$$\mathbf{A}^\dagger\mathbf{A}\mathbf{x} = \mathbf{A}^\dagger\mathbf{b}, \tag{2.61}$$

where the superscript † denotes the transpose conjugate operator and operation $\mathbf{A}^\dagger\mathbf{A}$ is symmetric and positive defined. The implementation of a CG method for the normal equations is summarized in the Algorithm 1 (Peterson; Ray; Mittra, 1998).

Algorithm 1: Conjugate gradient algorithm

Initial steps:

Guess $\mathbf{x}_0$

$\mathbf{r}_0 = \mathbf{A}\mathbf{x}_0 - \mathbf{b}$

$\mathbf{p}_1 = -\mathbf{A}^\dagger\mathbf{r}_0$

Iterate $(n = 1, 2, ...)$:

$\alpha_n = -\frac{\langle \mathbf{A}\mathbf{p}_n, \mathbf{r}_{n-1}\rangle}{\|\mathbf{A}\mathbf{p}_n\|^2} = \frac{\|\mathbf{A}^\dagger\mathbf{r}_{n-1}\|^2}{\|\mathbf{A}\mathbf{p}_n\|^2}$

$\mathbf{x}_n = \mathbf{x}_{n-1} + \alpha_n\mathbf{p}_n$

$\mathbf{r}_n = \mathbf{A}\mathbf{x}_\mathbf{n} - \mathbf{b} = \mathbf{r}_{n-1} + \alpha_n\mathbf{A}\mathbf{p}_n$

$\beta_n = \frac{\|\mathbf{A}^\dagger\mathbf{r}_n\|^2}{\|\mathbf{A}^\dagger\mathbf{r}_{n-1}\|^2}$

$\mathbf{p}_{n+1} = -\mathbf{A}^\dagger\mathbf{r}_n + \beta_n\mathbf{p}_n$

Terminate when a norm of $\mathbf{r}_n$ falls below some predetermined value.

The CG algorithm stops the iterations when the maximum number of iterations n_{max} is reached, or the residual norm decreases to a predetermined value. We use the following convergence criterion

$$\frac{\|\mathbf{r}_n\|}{\|\mathbf{b}\|} = \frac{\|\mathbf{A}\mathbf{x}_n - \mathbf{b}\|}{\|\mathbf{b}\|} < \epsilon, \tag{2.62}$$

where ϵ is the tolerance. The CG method has been used widely in computational electromagnetics. The implementation steps of the CG algorithm in EM problems, matrix eigenvalues features, and convergence rate are reviewed in Peterson et al. (1991) and Wilton and E. Wheeler III (1991).

2.3.4 Matrix-vector multiplication using FFT

Electromagnetic problems posed in terms of integral equations with convolutional kernels can sometimes be discretized to yield matrices with discrete convolutional symmetries (Peterson; Ray; Mittra, 1998). In the one-dimensional case, we consider the following operation

$$y_m = \sum_{n=1}^{N} G_{m-n}\, x_n, \tag{2.63}$$

where y, x, and G denote sequences of numbers. The Equation (2.63) can be written in matrix form as

$$\begin{bmatrix} y_1 \\ y_2 \\ y_3 \\ \vdots \\ y_N \end{bmatrix} = \begin{bmatrix} G_0 & G_{-1} & G_{-2} & \cdots & G_{1-N} \\ G_1 & G_0 & G_{-1} & \cdots & G_{2-N} \\ G_2 & G_1 & G_0 & \cdots & G_{3-N} \\ \vdots & \vdots & \vdots & \ddots & \vdots \\ G_{N-1} & G_{N-2} & G_{N-3} & \cdots & G_0 \end{bmatrix} \begin{bmatrix} x_1 \\ x_2 \\ x_3 \\ \vdots \\ x_N \end{bmatrix}. \tag{2.64}$$

The matrix $N \times N$ depicted in the matrix system of (2.64) is a general Toeplitz matrix. This matrix is described by a total of $2N-1$ different values, corresponding to the entries in the first row and column. If the elements of the sequence G repeat with period N, so that, the operation

$$G_{n-N} = G_n \qquad n = 1, 2, ..., N-1, \tag{2.65}$$

is known as the circular discrete convolution. However, (2.65) is not a circular discrete convolution, since the second row of the $N \times N$ matrix is not a circular right shift of the elements of the first row. Otherwise, it is well known that any noncircular discrete convolution can be embedded into a circular discrete convolution. This can be performed

by extending the original sequence G to repeat with period $2N-1$. The extended sequence G^e can be written as a vector and the elements are given by

$$\overline{G}^e = [G_0, G_1, G_2, \cdots, G_{N-1}, G_{1-N}, G_{2-N}, G_{-1}]^T , \tag{2.66}$$

And the extended sequence $\overline{x}^e$ is obtained by zero-padding the original sequence $\overline{x}$ into a vector of size $2N-1$, as follows

$$\overline{x}^e = [x_1, x_2, x_3, \cdots, x_N, 0, 0, \cdots 0]^T . \tag{2.67}$$

According to the discrete convolution theorem, the discrete convolution operation of (2.63) can be implemented using the FFT and inverse FFT algorithm

$$\overline{y}^e = \mathrm{FFT}^{-1}\left[\mathrm{FFT}(\overline{G}^e) \odot \mathrm{FFT}(\overline{x}^e)\right], \tag{2.68}$$

where $\odot$ denotes point-wise multiplication. If the discrete convolution is linear, then the FFTs must be of length $2N-1$ rather than length N, and the result of the operation in (2.68) is extracted from the first N elements of $\overline{y}^e$.

We can extend to the case of two-dimensional discrete convolution

$$y_{ij} = \sum_{m=1}^{M}\sum_{n=1}^{N} G_{i-m,j-n}\ x_{mn} \qquad \begin{Bmatrix} i \\ j \end{Bmatrix} = 1, 2, ..., \begin{Bmatrix} M \\ N \end{Bmatrix} . \tag{2.69}$$

The equivalent $MN \times MN$ matrix can be written as

$$\mathbf{G} = \begin{bmatrix} \mathbf{G}_0 & \mathbf{G}_{-1} & \mathbf{G}_{-2} & \cdots & \mathbf{G}_{1-M} \\ \mathbf{G}_1 & \mathbf{G}_0 & \mathbf{G}_{-1} & \cdots & \mathbf{G}_{2-M} \\ \mathbf{G}_2 & \mathbf{G}_1 & \mathbf{G}_0 & \cdots & \mathbf{G}_{3-M} \\ \vdots & \vdots & \vdots & \ddots & \vdots \\ \mathbf{G}_{M-1} & \mathbf{G}_{M-2} & \mathbf{G}_{M-3} & \cdots & \mathbf{G}_0 \end{bmatrix} \tag{2.70}$$

where each element is an $N \times N$ block Toeplitz matrix, which is itself a Toeplitz matrix of the form presented in (2.64). This procedure can be easily generalized to multiple dimensions by using Equation (2.68).

In summary, for a matrix of size $N \times N$, the matrix-vector product using FFT algorithms has a computational complexity of $O(N \log N)$, which is lower than the counterpart $O(N^2)$ of the traditional iterative methods (Peterson; Ray; Mittra, 1998).

The discrete convolutional procedure described above can be applied to the integral equation for the two-dimensional scattering problem formulated in subsection 2.3.2. From (2.53) we have the following discrete system

$$E_{ij}^{inc} = E_{ij} - \sum_{m=1}^{N_x}\sum_{n=1}^{N_y} G_{i-m,j-n}\,\chi_{mn}\,E_{mn}, \qquad \begin{cases} i = 1,2,...,N_x \\ j = 1,2,...,N_y \end{cases} \tag{2.71}$$

This can be embedded into a circular discrete convolution by extending the parameter $\overline{\overline{G}}^{\mathrm{e}}$ of size $(2N_x - 1) \times (2N_y - 1)$

$$G^{\mathrm{e}}(p,q) = G_{p',q'}$$

$$p' = \begin{cases} p-1, & \text{if } 1 \le p \le N_x \\ p - 2N_x, & N_x \le p \le 2N_x - 1 \end{cases} , q' = \begin{cases} q-1, & \text{if } 1 \le q \le N_y \\ q - 2N_y, & N_y \le q \le 2N_y - 1 \end{cases} \tag{2.72}$$

For convenience, Equation (2.71) is generalized by introducing the notation $U = \chi E$. Therefore, U represents any parameter. In practice, U can be replaced by the electric field or it can also be the electric current density J as in Chen (2018) and Peterson, Ray and Mittra (1998). The extended parameter $\overline{\overline{U}}^{\mathrm{e}}$ of size $(2N_x - 1) \times (2N_y - 1)$ is defined in the extend domain by zero padding as

$$U^{\mathrm{e}}(p,q) = \begin{cases} U(p,q), & \text{if } 1 \le p \le N_x \text{ and } 1 \le q \le N_y \\ 0, & \text{else} \end{cases} \tag{2.73}$$

By using (2.68) the matrix-vector multiplication can be efficiently calculated by

$$\overline{\overline{G}} \cdot \overline{U} = \mathrm{FFT}_2^{-1}\left\{\mathrm{FFT}_2(\overline{\overline{G}}^{\mathrm{e}}) \odot \mathrm{FFT}_2(\overline{U}^{\mathrm{e}})\right\}, \tag{2.74}$$

where FFT_2 denotes a two-dimensional fast Fourier transform. Finally, the result of the product of (2.74) is extracted from the elements of its upper left sub-matrix of size $N_x \times N_y$. More details on the implementation and examples of the convolution-type matrix-vector products are provided in Appendix A.

To solve the matrix system of (2.53), the CG algorithm can be efficiently implemented by using the matrix-vector multiplication procedure presented above. This approach is known as the CG-FFT method (Peterson; Ray; Mittra, 1998). The CG algorithm requires two types of matrix-vector multiplication at each iteration, one with $\mathbf{A}$ and the other with $\mathbf{A}^{\dagger}$, that is, the CG implies that the transpose conjugate matrix also needs to be computed. In discrete form, $\mathbf{A}^{\dagger}$ is written as $\overline{\overline{A}}^{H}$, where the superscript H denotes the Hermitian operator, i.e., transpose conjugate operator. Therefore, the discrete system in terms of FFTs produces

$$(\overline{\overline{I}} - \overline{\overline{G}} \cdot \overline{\overline{\chi}}) \cdot \overline{E} = \overline{E} - \mathrm{FFT}^{-1}\left\{\mathrm{FFT}(\overline{\overline{G}}^{\mathrm{e}}) \odot \mathrm{FFT}(\overline{\overline{\chi \cdot E}}^{\mathrm{e}})\right\} \tag{2.75}$$

and

$$(\overline{\overline{I}} - \overline{\overline{G}} \cdot \overline{\overline{\chi}})^H \cdot \overline{E} = \overline{E} - \left\{ \overline{\overline{\chi}} \cdot \mathrm{FFT}^{-1} \left[\mathrm{FFT}(\overline{\overline{G}}^{\mathrm{e}}) \odot \mathrm{FFT}(\overline{\overline{E}}^{\mathrm{e}*}) \right] \right\}^* . \tag{2.76}$$

This implementation is computationally efficient since the computation of matrix-vector operations is performed by FFTs instead of storing the whole matrix $\overline{\overline{G}}$ and computing full matrix-vector products. The advantage of using the CG-FFT scheme is that it only requires $O(N \log N)$ operations and necessary storage of $O(N)$, where N is the number of unknowns.

2.4 Three-Dimensional Scattering Problems

This section describes the scattering problem in three dimensions. Similar to the two-dimensional problem of the previous section, we consider EFIE formulations applied to scattering by objects of arbitrary shape. Approaches using the dyadic Green's function (DGF) for both the electric field and the magnetic vector potential are presented.

For a three-dimensional problem, all spatial components are present. In this case, the object domain $D \subset \mathbf{R}^3$ embeds an arbitrary scatterer and the spatial domain is $\mathbf{r} = (x, y, z)$. The electromagnetic scattering is governed by the following electric field volume integral equation based on the well-known Lippmann–Schwinger equation

$$\mathbf{E}(\mathbf{r}) = \mathbf{E}^{inc}(\mathbf{r}) + k_b^2 \iiint \overline{\overline{G}}(\mathbf{r}, \mathbf{r}') \cdot \overline{\overline{\chi}}(\mathbf{r}') \mathbf{E}(\mathbf{r}') d\mathbf{r}'. \tag{2.77}$$

where the electric field $\mathbf{E}(\mathbf{r})$ contains the three components (E_x, E_y, E_z) and the contrast tensor is $\overline{\overline{\chi}} = \mathrm{diag}[\chi_x \ \chi_y \ \chi_z]$. If an isotropic medium is assumed then $\chi_x = \chi_y = \chi_z$, that is, the diagonal of the tensor $\overline{\overline{\chi}}$ corresponds to three replicas of the isotropic contrast function.

For 3D scattering problems, the electric field can be expressed in terms of both electric and magnetic dyadic Green's functions. The conventional method to solve the integral equation (2.77) is the method of moments. The aforementioned DGFs can be evaluated with analytic expressions (Livesay; Chen, 1974; Zhang; Liu, 2015). In comparison, the DGF for the magnetic vector potential is computed using weak-form discretization. Whereas, the DGF for the electric field uses the conventional MoM with the pulse basis functions. We point out that both formulations of DGF have been successfully applied to 3D inverse scattering problems (Zhang et al., 2003; Zhong; Chen, 2011; Estatico et al., 2018). However, the conventional 3D MoM (without the weak-form discretization) works well for low dielectric contrasts. The limitations of the conventional MoM are discussed in Massoudi, Durney and Iskander (1984). Meanwhile, the weak-form discretization also works for high dielectric contrasts, as shown in Zhang et al. (2003).

It is important to emphasize that the DGFs in the integral equation have a singularity. Much research has been done to treat this singularity, such as the numerical method presented in Livesay and Chen (1974), which uses the conventional MoM. Here, the singularity is computed with the contribution of a unit current density in the discretized cell, when $\mathbf{r} = \mathbf{r}'$, and adding a correction term (Van Bladel, 1961). On the other hand, the scheme developed by Zwamborn and van den Berg (1992) leads to a weaker singularity in the dyadic Green's function operation, which does not involve the surface charge term in Su (1993).

In this thesis, we exhibit two alternatives to solve the forward scattering problem in 3D, where the singularity is circumvented in different ways. We focus on numerical implementations and efficient methods that combine iterative and FFT algorithms. We would prefer to use the weak-form scheme, which appears to be more accurate (Zhang et al., 2003). However, the scatterers of the inverse scattering problems used in this work do not deal with high contrasts, so either of the two formulations can be adopted.

2.4.1 Dyadic Green's function for 3D scattering problems

For three-dimensional scattering by isotropic dielectric objects, the volume integral equation (2.77) can be rewritten in terms of the DGF for the magnetic vector potential $\mathbf{A}$ (DGFA)

$$\mathbf{E}^{inc}(\mathbf{r}) = \mathbf{E}(\mathbf{r}) - (k_b^2 + \nabla\nabla\cdot)\mathbf{A}(\mathbf{r}), \quad \mathbf{r} \in D \tag{2.78}$$

where the magnetic vector potential is given by

$$\mathbf{A}(\mathbf{r}) = \int_D \overline{\overline{G}}^A(\mathbf{r}, \mathbf{r}') \cdot \overline{\overline{\chi}}(\mathbf{r}')\mathbf{E}(\mathbf{r}')d\mathbf{r}' \tag{2.79}$$

where $\overline{\overline{G}}^A$ is the DGFA, which is defined as

$$\overline{\overline{G}}^A(\mathbf{r}, \mathbf{r}') = g(\mathbf{r}, \mathbf{r}')\overline{\overline{I}} \tag{2.80}$$

where $\overline{\overline{I}}$ is the unit tensor and $g(\mathbf{r}, \mathbf{r}')$ is the 3D scalar Green's function (2.22). The Equation (2.79) can be treated as a convolution since the translational invariance of the dyadic Green's function can be written as $\overline{\overline{G}}(\mathbf{r}, \mathbf{r}') = \overline{\overline{G}}(\mathbf{r} - \mathbf{r}')$ and

$$|\mathbf{r} - \mathbf{r}'| = \sqrt{(x - x')^2 + (y - y')^2 + (z - z')^2}. \tag{2.81}$$

Alternatively, if the DGF for the electric field $\mathbf{E}$ (DGFE) is adopted, the volume integral equation can be rewritten as

$$\mathbf{E}^{inc}(\mathbf{r}) = \mathbf{E}(\mathbf{r}) - k_b^2 \int_D \overline{\overline{G}}^E(\mathbf{r}, \mathbf{r}') \cdot \overline{\overline{\chi}}(\mathbf{r}')\mathbf{E}(\mathbf{r}')d\mathbf{r}', \quad \mathbf{r} \in D \tag{2.82}$$

where $\overline{\overline{G}}^E$ is the DGFE, which is defined as

$$\overline{\overline{G}}^E(\mathbf{r},\mathbf{r}') = \left[\overline{\overline{I}} + \frac{1}{k_b^2}\nabla\nabla\right] g(\mathbf{r},\mathbf{r}') \tag{2.83}$$

Equations (2.78) and (2.82) are valid both inside and outside the domain D. The numerical solutions of these EFIEs are presented in the following two subsections.

2.4.2 Evaluation of the DGFA

Equation (2.78) is the Fredholm integral equation of the second kind and represents the solution of the internal electric field $\mathbf{E}(\mathbf{r})$. However, note that this equation is hyper-singular and involves the second-order derivatives of the scalar Green's function. In order to discretize (2.78), we use a variant of the weak-form discretization and a finite-difference scheme to approximate the differential operator $\nabla\nabla\cdot\mathbf{A}(\mathbf{r})$ (Zhang et al., 2003).

Consider a three-dimensional scattering problem configuration under the illumination of an incident field, which is formulated by the Equation (2.77). In order to apply the weak form of the EFIE, the domain D is discretized into N small cubic cells, as shown in Figure 7.

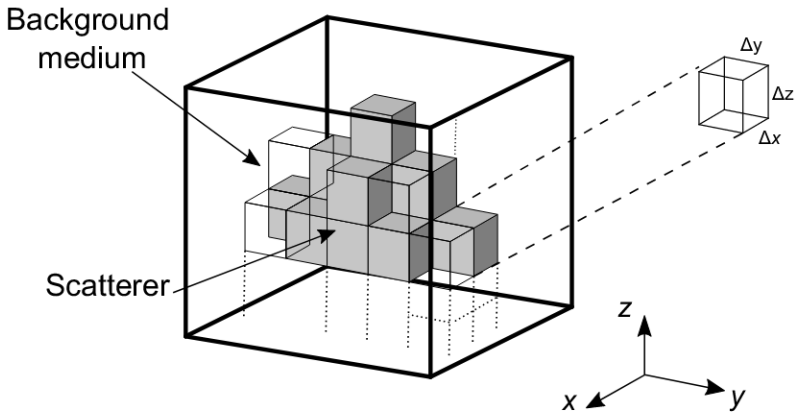

Figure 7 – 3D discretization of the domain of interest.

Initially, we discrete the cubic cells with the cell centers located at $\mathbf{r}_{i,j,k} = (x_i, y_j, z_k)$

$$\mathbf{r}_{i,j,k} = \left[x_{\min} + (i-\frac{1}{2})\Delta x\right]\hat{\mathbf{x}} + \left[y_{\min} + (j-\frac{1}{2})\Delta y\right]\hat{\mathbf{y}} + \left[z_{\min} + (k-\frac{1}{2})\Delta z\right]\hat{\mathbf{z}} \tag{2.84}$$

where $i \in [1, N_x]$, $j \in [1, N_y]$, $k \in [1, N_z]$, and the grid cell sizes are Δx, Δy, Δz.

Enforcing (2.78) at the center of each of the cells with the Dirac delta function as testing functions (Harrington, 1968), we obtain

$$\mathbf{E}^{inc}_{i,j,k} = \mathbf{E}_{i,j,k} - k_b^2\mathbf{A}_{i,j,k} - (\nabla\nabla\cdot\mathbf{A})_{i,j,k} \tag{2.85}$$

where $\mathbf{E}^{inc}_{i,j,k} = \mathbf{E}^{inc}(\mathbf{r}_{i,j,k})$, $\mathbf{E}_{i,j,k} = \mathbf{E}(\mathbf{r}_{i,j,k})$, $\mathbf{A}_{i,j,k} = \mathbf{A}(\mathbf{r}_{i,j,k})$. If the contrast and the total electric field are assumed to be constant in each cell, the magnetic vector potential $\mathbf{A}_{i,j,k}$ can be expressed as

$$\mathbf{A}_{i,j,k} = \sum_{i'=1}^{N_x}\sum_{j'=1}^{N_y}\sum_{k'=1}^{N_z}\int G(\mathbf{r}_{i,j,k},\mathbf{r}')\chi_{i',j',k'}\mathbf{E}_{i',j',k'}d\mathbf{r}'. \tag{2.86}$$

For a homogeneous and isotropic medium, in Zwamborn and van den Berg (1992) is presented a spherical mean (weak-form) of the Green's function to suppress the singularity when $\mathbf{r} = \mathbf{r}'$. Using spherical coordinates, the weak-form of the Green's function can be defined as

$$[G](\mathbf{r}) = \frac{\int_{|\mathbf{r}''|<(1/2)\Delta r} G(\mathbf{r}+\mathbf{r}'')d\mathbf{r}''}{\int_{|\mathbf{r}''|<(1/2)\Delta r} d\mathbf{r}''}. \tag{2.87}$$

Therefore, the weakened Green's function can be implemented as

$$[G](\mathbf{r},\mathbf{r}') = \begin{cases} \frac{\left(1+\frac{1}{2}jk_b\Delta r\right)e^{-\frac{1}{2}jk_b\Delta r}-1}{\frac{1}{6}\pi k_b^2(\Delta r)^3} & |\mathbf{r}-\mathbf{r}'| = 0, \\ \frac{e^{-jk_b|\mathbf{r}-\mathbf{r}'|}\left[\frac{-\sinh\left(-\frac{1}{2}jk_b\Delta r\right)}{\frac{1}{2}jk_b\Delta r}-\cosh\left(-\frac{1}{2}jk_b\Delta r\right)\right]}{\frac{1}{3}\pi(k_b\Delta x)^2|\mathbf{r}-\mathbf{r}'|} & |\mathbf{r}-\mathbf{r}'| > \frac{1}{2}\Delta r, \end{cases} \tag{2.88}$$

where $\Delta r = \min(\Delta x, \Delta y, \Delta z)$. As a consequence, the discritized form of the magnetic vector potential $\mathbf{A}_{i,j,k}$ can be written as

$$\mathbf{A}_{i,j,k} = \Delta x\Delta y\Delta z\sum_{i'=1}^{N_x}\sum_{j'=1}^{N_y}\sum_{k'=1}^{N_z} G_{i-i',j-j',k-k'}\chi_{i',j',k'}\mathbf{E}_{i',j',k'} \tag{2.89}$$

where $i \in [0, N_x+1]$, $j \in [0, N_y+1]$, $k \in [0, N_z+1]$, which is denoted as domain D' containing D, as shown in Figure 8. As in Zhang and Liu (2003), the Cartesian components of $(\nabla\nabla\cdot\mathbf{A})_{i,j,k}$ in (2.85) are approximated by the following central finite differencing scheme

$$\begin{aligned}(\nabla\nabla\cdot\mathbf{A})_{x;i,j,k} \approx\ & \frac{A_{x;i+1,j,k} - 2A_{x;i,j,k} + A_{x;i-1,j,k}}{\Delta x^2} \\ &+ \frac{A_{y;i+1,j+1,k} - A_{y;i+1,j-1,k} - A_{y;i-1,j+1,k} + A_{y;i-1,j-1,k}}{4\Delta x\Delta y} \\ &+ \frac{A_{z;i+1,j,k+1} - A_{z;i+1,j,k-1} - A_{z;i-1,j,k+1} + A_{z;i-1,j,k-1}}{4\Delta x\Delta z}\end{aligned} \tag{2.90}$$

$$
\begin{aligned}
(\nabla\nabla\cdot\mathbf{A})_{y;i,j,k} \approx & \frac{A_{x;i+1,j+1,k}-A_{x;i+1,j-1,k}-A_{x;i-1,j+1,k}+A_{x;i-1,j-1,k}}{4\Delta x\Delta y} \\
& + \frac{A_{y;i,j+1,k}-2A_{y;i,j,k}+A_{y;i,j-1,k}}{\Delta y^2} \\
& + \frac{A_{z;i,j+1,k+1}-A_{z;i,j+1,k-1}-A_{z;i,j-1,k+1}+A_{z;i,j-1,k-1}}{4\Delta y\Delta z}
\end{aligned} \tag{2.91}
$$

$$
\begin{aligned}
(\nabla\nabla\cdot\mathbf{A})_{z;i,j,k} \approx & \frac{A_{x;i+1,j,k+1}-A_{x;i+1,j,k-1}-A_{x;i-1,j,k+1}+A_{x;i-1,j,k-1}}{4\Delta x\Delta z} \\
& + \frac{A_{z;i,j+1,k+1}-A_{z;i,j+1,k-1}-A_{z;i,j-1,k+1}+A_{z;i,j-1,k-1}}{4\Delta y\Delta z} \\
& + \frac{A_{z;i,j,k-1}-2A_{z;i,j,k}+A_{z;i,j,k+1}}{\Delta z^2}.
\end{aligned} \tag{2.92}
$$

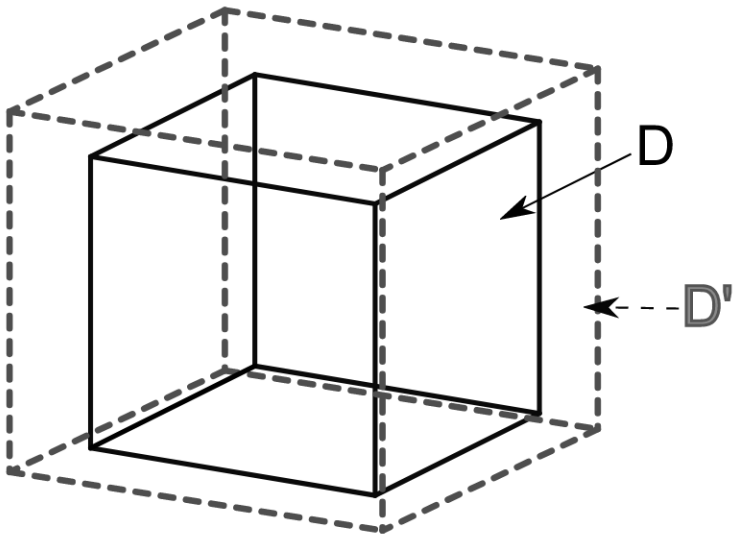

Figure 8 – Domains D and D' for finite-difference procedure.

Equation (2.85) can be written as a linear operator

$$\mathcal{L}\mathbf{E} = \mathbf{E}^{inc}, \tag{2.93}$$

where the linear operator $\mathcal{L}$ is a $3N \times 3N$ matrix, $\mathbf{E}$ is a $3N \times 1$ vector containing the three Cartesian components of the total electric field, similarly, $\mathbf{E}^{inc}$ is the $3N \times 1$ vector incident field.

The direct matrix inversion of (2.93) is computationally prohibitive. Iterative Krylov subspace methods are appropriate for the solution of large-scale volume integral equations, such as the conjugate gradient (CG) method, biconjugate gradient (BiCG) method, and biconjugate gradient stabilized (BiCGSTAB) method. If an iterative method is used the complexity computational is $O(N^2)$ and the memory requirement is $O(N^2)$,

where $N = N_x \times N_y \times N_z$ is the number of unknowns. However, it is possible to use the discrete convolution theorem and FFT algorithms to perform matrix-vector multiplications, similar to the two-dimensional case presented in Section 2.3. Consequently, each iteration requires only $O(N \log N)$ operations and necessary storage of $O(N)$.

In solving the three-dimensional scattering problem, many efficient methods combining iterative methods and FFT algorithms have been developed, such as the CG-FFT method (Zwamborn; van den Berg, 1992; Ma et al., 2009), the BiCG-FFT method (Gan; Chew, 1995; Zhang; Liu, 2001), and the BiCGSTAB-FFT method (Zhang; Liu; Xu, 2003). In this work, we adopt a biconjugate gradient stabilized (BiCGSTAB) method combined with a 3D FFT algorithm to solve the linear system in (2.93). The iterative method and FFT procedures are presented in subsections 2.4.4 and 2.4.5, respectively.

2.4.3 Evaluation of the DGFE

From (2.82) the scattered field by an arbitrary shape object can be described by the following EFIE

$$\mathbf{E}^{sca}(\mathbf{r}) = k_b^2 \int_D \overline{\overline{G}}^E(\mathbf{r}, \mathbf{r}') \cdot \overline{\overline{\chi}}(\mathbf{r}')\mathbf{E}(\mathbf{r}')d\mathbf{r}' \quad \text{for} \quad \mathbf{r} \in S. \tag{2.94}$$

According to Van Bladel (1961), a correction term in the scattered field must be added, thus $\mathbf{E}^{sca}(\mathbf{r})$ can be rewritten as

$$\mathbf{E}^{sca}(\mathbf{r}) = k_b^2 PV \int_D \overline{\overline{G}}^E(\mathbf{r}, \mathbf{r}') \cdot \overline{\overline{\chi}}(\mathbf{r}')\mathbf{E}(\mathbf{r}')d\mathbf{r}' + [\mathbf{E}^{sca}(\mathbf{r})]_{\text{correction}}, \tag{2.95}$$

$$\mathbf{E}^{sca}(\mathbf{r}) = k_b^2 PV \int_D \overline{\overline{G}}^E(\mathbf{r}, \mathbf{r}') \cdot \overline{\overline{\chi}}(\mathbf{r}')\mathbf{E}(\mathbf{r}')d\mathbf{r}' - \frac{1}{3}\overline{\overline{\chi}}(\mathbf{r})\mathbf{E}(\mathbf{r}), \tag{2.96}$$

where PV denotes the principal value of the integral. The total electric field is the sum of the incident field and scattered field, so that,

$$\mathbf{E}(\mathbf{r}) = \mathbf{E}^{inc}(\mathbf{r}) + k_b^2 PV \int_D \overline{\overline{G}}^E(\mathbf{r}, \mathbf{r}') \cdot \overline{\overline{\chi}}(\mathbf{r}')\mathbf{E}(\mathbf{r}')d\mathbf{r}' - \frac{1}{3}\overline{\overline{\chi}}(\mathbf{r})\mathbf{E}(\mathbf{r}). \tag{2.97}$$

Rearranging terms we have

$$\mathbf{E}^{inc}(\mathbf{r}) = \left(1 + \frac{1}{3}\overline{\overline{\chi}}(\mathbf{r})\right)\mathbf{E}(\mathbf{r}) - k_b^2 PV \int_D \overline{\overline{G}}^E(\mathbf{r}, \mathbf{r}') \cdot \overline{\overline{\chi}}(\mathbf{r}')\mathbf{E}(\mathbf{r}')d\mathbf{r}'. \tag{2.98}$$

Assume a three-dimensional scatterer, which is partitioned into N subvolumes or cells, as in Figure 7. Here, we apply MoM to approximate (2.98) into a matrix system.

Applying the pulse basis functions

$$\mathbf{E}(x,y,z) \cong \sum_{n=1}^{N} (\hat{x}E_{xn} + \hat{y}E_{yn} + \hat{z}E_{zn}) f_n(x,y,z), \tag{2.99}$$

where

$$f_n(x,y,z) = \begin{cases} 1 & \text{if } (x,y,z) \in \text{cell } n \\ 0 & \text{otherwise} \end{cases} \tag{2.100}$$

Enforcing Equation (2.98) at the center of each cell, where each cell is denoted by $v_m (m = 1, 2, \cdots, N)$, then the dyadic Green's function can be rewritten as follows

$$G^{mn}_{x_p x_q} = k_b^2 \left[\delta_{pq} + \frac{1}{k_b^2} \frac{\partial^2}{\partial x_p \partial x_q} \right] g_n \Delta v \qquad p, q = 1, 2, 3. \tag{2.101}$$

where $\Delta v = \Delta x \times \Delta y \times \Delta z$ is the volume of the rectangular cell, δ_{pq} is the Kronecker delta function, and $x_1 = x$, $x_2 = y$, and $x_3 = z$. After tedious calculations, we obtain the matrix elements of the Green's function for off-diagonal entries

$$\begin{aligned} G^{mn}_{x_p x_q} &= -\frac{\Delta v e^{-jk_b R_{mn}}}{4\pi R^3_{mn}} \{ (1 - k_b^2 R^2_{mn} + jk_b R_{mn}) \delta_{pq} \\ &+ \frac{(x_p^m - x_n^p)(x_q^m - x_n^q)}{R^2_{mn}} [k_b^2 R^2_{mn} - 3jk_b R_{mn} - 3] \}, \qquad m \neq n, \end{aligned} \tag{2.102}$$

where

$$R_{mn} = |\mathbf{r}_m - \mathbf{r}_n| \tag{2.103}$$

$$\mathbf{r}_m = (x_1^m, x_2^m, x_3^m) \qquad \mathbf{r}_n = (x_1^n, x_2^n, x_3^n)\,. \tag{2.104}$$

However, when $\mathbf{r}_m = \mathbf{r}_n$ the Green's function has singularity. In order to evaluate this integral, the subvolume v_n is approximated by an equivolumic sphere of radius a centered at $\mathbf{r}_n$ (Livesay; Chen, 1974), that is

$$a = \left(\frac{3\Delta v}{4\pi} \right)^{1/3}. \tag{2.105}$$

Then, the matrix diagonal elements are given by

$$G^{nn}_{x_p x_q} = \delta_{pq} [\frac{2}{3} (jk_b a + 1) e^{-jk_b a} - 1], \qquad m = n. \tag{2.106}$$

For convenience, we introduce the operators $\overline{\overline{G}}_D$ and $\overline{\overline{G}}_S$ which are operators mapping the domain integral equations in the domain of interest (DOI) and the transmitter-receiver region, see Figure 2. Mathematically, it is written as

$$k_b^2 \int_{\text{cell}} \left[\overline{\overline{I}} + \frac{1}{k_b^2} \nabla\nabla \right] g(\mathbf{r}, \mathbf{r}') d\mathbf{r}' = \begin{cases} \overline{\overline{G}}_D & \text{for} \quad \mathbf{r} \in D \\ \\ \overline{\overline{G}}_S & \text{for} \quad \mathbf{r} \in S \end{cases}. \tag{2.107}$$

Then the forward problem can be written in compact notations

$$\overline{\overline{E}} = \overline{E}^{inc} + \overline{\overline{G}}_D \cdot \overline{\overline{\chi}} \cdot \overline{E} \tag{2.108}$$

$$\overline{E}^{sca} = \overline{\overline{G}}_S \cdot \overline{\overline{\chi}} \cdot \overline{E}, \tag{2.109}$$

Finally, the matrix system in (2.108) can be written as

$$\overline{E}^{inc} = (\overline{\overline{I}} - \overline{\overline{G}}_D \cdot \overline{\overline{\chi}}) \cdot \overline{E}, \tag{2.110}$$

where

$$\overline{\overline{G}}_D = \begin{bmatrix} \overline{\overline{G}}_{D;xx} & \overline{\overline{G}}_{D;xy} & \overline{\overline{G}}_{D;xz} \\ \overline{\overline{G}}_{D;yx} & \overline{\overline{G}}_{D;yy} & \overline{\overline{G}}_{D;yz} \\ \overline{\overline{G}}_{D;zx} & \overline{\overline{G}}_{D;zy} & \overline{\overline{G}}_{D;zz} \end{bmatrix} \tag{2.111}$$

is a $3N \times 3N$ matrix whose entries are obtained from Equations (2.102) and (2.106), where $N = N_x \times N_y \times N_z$. Note that Equation (2.110) is approximate to the matrix system of the Equation (2.93) ($\mathcal{L}\mathbf{E} = \mathbf{E}^{inc}$) obtained from the DGFA formulation. In this way, the BiCGSTAB method and the FFT procedure to perform matrix-vector products can be applied to both DGFA and DGFE formulations.

2.4.4 Biconjugate gradient stabilized method

The implementation of the BiCGSTAB algorithm to solve the matrix system $\mathcal{L}\mathbf{E} = \mathbf{E}^{inc}$ is given in Algorithm 2. For three-dimensional scattering problems, the BiCGSTAB-FFT method converges much faster than the CG-FFT and BiCG-FFT methods (Xu; Liu; Zhang, 2003; Zhang; Liu; Xu, 2003). Moreover, the BiCGSTAB has shown much smoother convergence curves than the BiCG method (Van der Vorst, 1992). Compared to the CG scheme, the BiCGSTAB scheme does not require the transpose conjugate of the matrix $\mathcal{L}$, which is a difficult operation to evaluate. These advantages make the BiCGSTAB method a good alternative for solving large linear systems. Note that in this BiCGSTAB, the dominant computational cost is associated with two operations: $\mathcal{L}\mathbf{p}_n$ and $\mathcal{L}\mathbf{s}$, in which an FFT algorithm is used to evaluate the discrete convolution kernel.

Algorithm 2: Biconjugate gradient stabilized algorithm

Initial steps:

Guess $\mathbf{E}_0$

$\mathbf{r}_0 = \mathbf{E}^{inc} - \mathcal{L}\mathbf{E}_0$

$\rho_0 = \alpha = \omega_0 = 1$

$\mathbf{v}_0 = \mathbf{p}_0 = 0$

Choose $\hat{\mathbf{r}}_0$ such that $\langle \hat{\mathbf{r}}_0, \mathbf{r}_0 \rangle \neq 0$, e.g., $\hat{\mathbf{r}}_0 = \mathbf{r}_0$

Iterate $(n = 1, 2, ...)$:

$\rho_n = \langle \hat{\mathbf{r}}_0, \mathbf{r}_{n-1} \rangle$

$\beta = \left(\frac{\rho_n}{\rho_{n-1}}\right)\left(\frac{\alpha}{\omega_{n-1}}\right)$

$\mathbf{p}_n = \mathbf{r}_{n-1} + \beta(\mathbf{p}_{n-1} - \omega_{n-1}\mathbf{v}_{n-1})$

$\mathbf{v}_n = \mathcal{L}\mathbf{p}_n$

$\alpha = \frac{\rho_n}{\langle \hat{\mathbf{r}}_0, \mathbf{v}_n \rangle}$

$\mathbf{s} = \mathbf{r}_{n-1} - \alpha\mathbf{v}_n$

$\mathbf{t} = \mathcal{L}\mathbf{s}$

$\omega_n = \frac{\langle \mathbf{t}, \mathbf{s} \rangle}{\langle \mathbf{t}, \mathbf{t} \rangle}$

$\mathbf{E}_n = \mathbf{E}_{n-1} + \alpha\mathbf{p}_n + \omega_n\mathbf{s}$

$\mathbf{r}_n = \mathbf{s} - \omega_n\mathbf{t}$

Terminate when the relative residual error $\|\mathbf{r}_n\| / \|\mathbf{E}^{inc}\|$ falls below some predetermined value.

2.4.5 Matrix-vector multiplication using FFT

The dense matrix $\overline{\overline{G}}_D$ in three-dimensional problems is shown in Figure 9, which consists of 9 block-Toeplitz matrices. However, only 6 components of DGF are used.

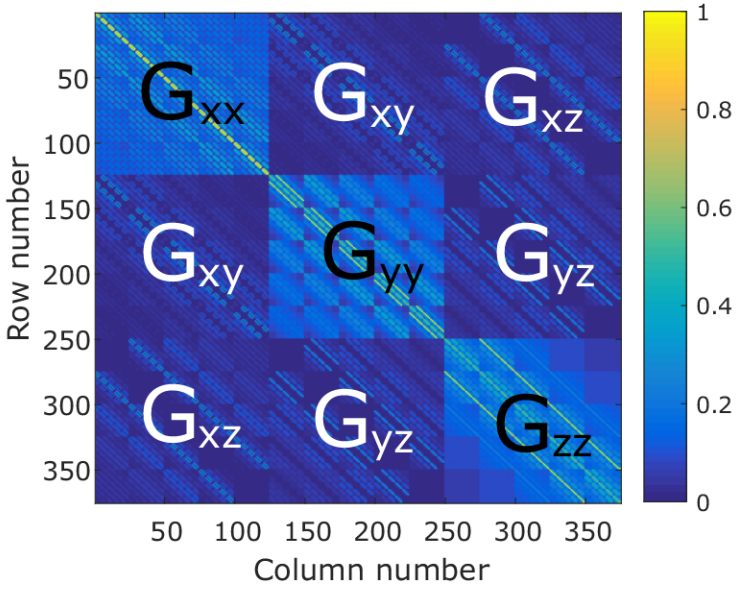

Figure 9 – Toeplitz structure of the dense matrix $\overline{\overline{G}}_D$ using N_x=N_y=$N_z = 5$.

The structure of each block-Toeplitz of the 3D dense matrix is similar to that of the 2D dense matrix introduced in subsection 2.3.2. Hence only the first row elements $[G_{x_p x_q}]_{1\times N}$ need to be stored. Now we extend the domain of interest in all spatial components as follows

$$\begin{aligned} x &= x_{\min} + \left(\tfrac{N_x}{2} - i'\right)\Delta x \qquad \text{for} \quad i' = 1, 2, ..., 2N_x - 1 \\ y &= y_{\min} + \left(\tfrac{N_y}{2} - j'\right)\Delta y \qquad \text{for} \quad j' = 1, 2, ..., 2N_y - 1. \\ z &= z_{\min} + \left(\tfrac{N_z}{2} - k'\right)\Delta z \qquad \text{for} \quad k' = 1, 2, ..., 2N_z - 1 \end{aligned} \tag{2.112}$$

Then the nonredundant matrix entries are converted to a 3D matrix of size $(2N_x - 1) \times (2N_y - 1) \times (2N_z - 1)$. Figure 10 shows the slices of the rearranged 3D matrix $\overline{\overline{G}}'$ for three-dimensional discrete convolution.

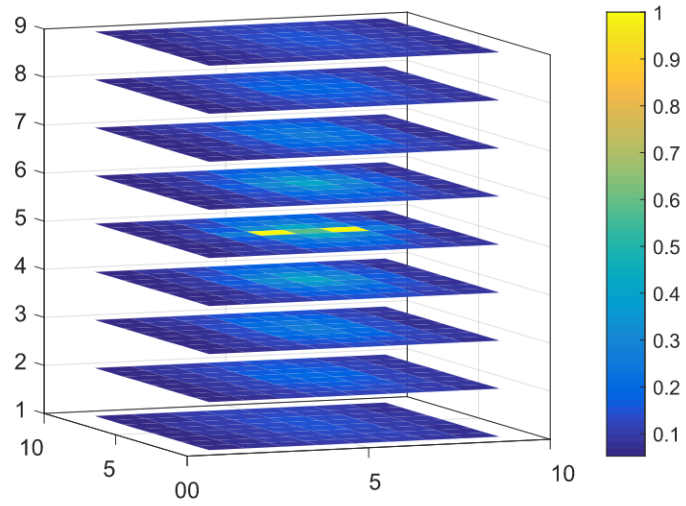

Figure 10 – Kernel for 3D discrete convolution procedure. 3D matrix slices using N_x=N_y=N_z = 5.

The discrete convolutional procedure described in subsection 2.3.4 can be easily extended to the integral equation for the three-dimensional scattering problems. From (2.93) or (2.110) we have the following discrete system

$$E^{inc}_{ijk} = E_{ijk} - \sum_{m=1}^{N_x}\sum_{n=1}^{N_y}\sum_{l=1}^{N_z} G_{i-m,j-n,k-l}\,\chi_{mnl}\,E_{mnl}, \qquad \begin{cases} i = 1, 2, ..., N_x \\ j = 1, 2, ..., N_y \\ k = 1, 2, ..., Nz \end{cases} \tag{2.113}$$

This can be embedded into a 3D circular discrete convolution by extending the parameter $\overline{\overline{G}}^{\mathrm{e}}$ of size $(2N_x - 1) \times (2N_y - 1) \times (2N_z - 1)$

$$G^{\mathrm{e}}(p, q, r) = G_{p',q',r'}$$

$$p' = \begin{cases} p-1 & \text{if } 1 \le p \le N_x \\ p-2N_x & N_x \le p \le 2N_x - 1 \end{cases}$$

$$q' = \begin{cases} q-1 & \text{if } 1 \le q \le N_y \\ p-2N_x & N_y \le p \le 2N_y - 1 \end{cases} \tag{2.114}$$

$$r' = \begin{cases} r-1 & \text{if } 1 \le r \le N_z \\ r-2N_z & N_z \le r \le 2N_z - 1 \end{cases}$$

The 3D extended parameter $\overline{\overline{U}}^{\mathrm{e}}$ of size $(2N_x-1)\times(2N_y-1)\times(2N_z-1)$ is defined in the extend domain by zero padding as

$$U^{\mathrm{e}}(p,q,r) = \begin{cases} U(p,q,r), & \text{if } 1 \le p \le N_x \\ & \text{and } 1 \le q \le N_y \\ & \text{and } 1 \le r \le N_z \\ 0, & \text{else} \end{cases} \tag{2.115}$$

Finally, the matrix-vector multiplication can be efficiently calculated by

$$\overline{\overline{G}} \cdot \overline{\overline{U}} = \mathrm{FFT}^{-1}\left\{\mathrm{FFT}(\overline{\overline{G}}^{\mathrm{e}}) \odot \mathrm{FFT}(\overline{\overline{U}}^{\mathrm{e}})\right\}, \tag{2.116}$$

where FFT denotes a three-dimensional fast Fourier transform and the result of the product of (2.116) is extracted from the elements of its upper left sub-matrix of size $N_x \times N_y \times N_z$. More details on the implementation of convolution-type matrix-vector products for 3D problems are provided in Appendix A.

2.5 Numerical Simulations

In this section, some numerical results in 2D and 3D dimensions are presented to validate the accuracy and efficiency of the EM forward solvers. We consider the scattering by a dielectric cylinder and a dielectric sphere. Then, the numerical solutions are compared with the corresponding analytical solution. The forward solvers are implemented with Matlab on an AMD Ryzen 5 2400G with Radeon Vega Graphics, 3.6GHz with 16GB RAM.

2.5.1 Scattering by a dielectric cylinder

We choose the scatterer to be a dielectric circular cylinder with $\varepsilon_r = 3.2 - j0.8$, this has a radius R of 0.5λ centered at the origin. The background is air, $\varepsilon_{rb} = 1$. The cylinder is illuminated by an incident plane wave, as shown in Figure 11(a). The operating

frequency is 300 MHz. According to the time dependency convention adopted in this work, the incident wave plane $\mathbf{E}^{inc}(z) = \hat{z}e^{-jk_b x}$ propagates in the $+x$ direction.

The analytical solution of the scattering by a dielectric cylinder is obtained from the formulation provided in chapter 6 of Jin (2015). In the MoM, the domain of interest D (2×2 m^2) is discretized into 60×60 square cells, as shown in Figure 11(b). The total electric field inside the domain D is recorded in the 1D distribution along the x-axis, at $y = 0$. As a result, Figure 12 shows the total electric field $\mathbf{E}(z)$. The numerical result is compared with the analytic solution, which is accurate in magnitude and phase.

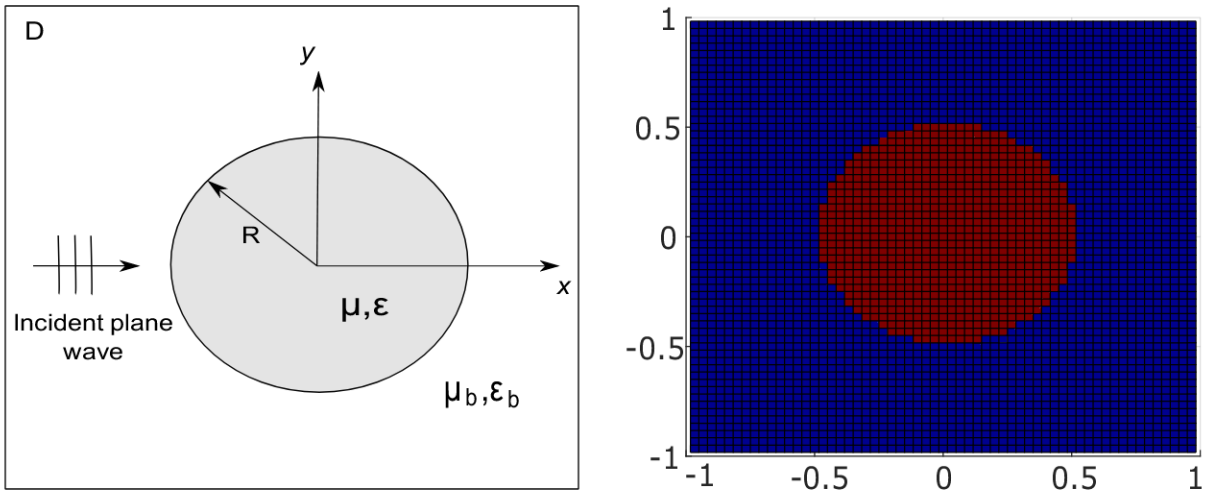

(a) (b)

Figure 11 – Cross section of the dielectric circular cylinder. (a) Continuous model. (b) 2D discretized model.

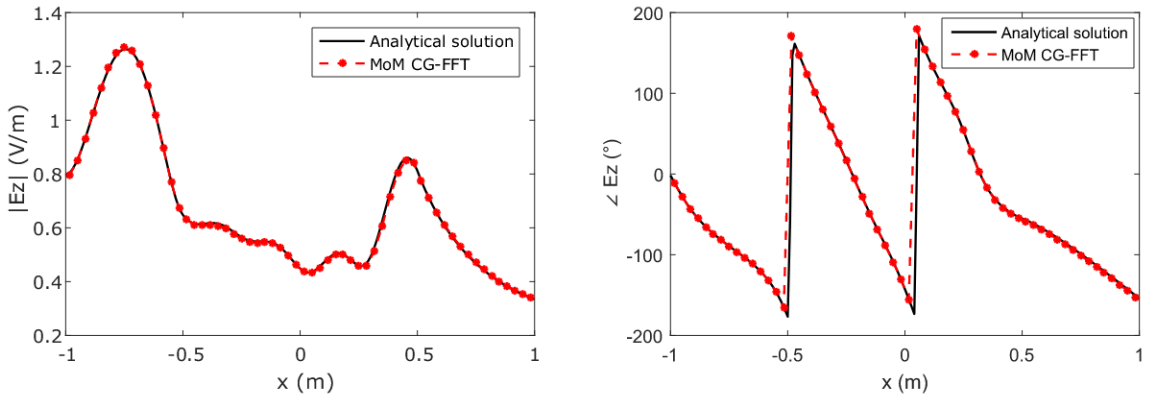

(a) (b)

Figure 12 – Total electric field by a dielectric cylinder ($\varepsilon_r = 3.2$ - $j0.8$ and radius equal to 0.5λ). z component along x-axis, y=0. (a) Magnitude. (b) Phase.

2.5.2 Scattering by a dielectric sphere

In order to compute the electromagnetic scattering by a dielectric sphere, we use both DGFE and DGFA formulations combined with the BiCGSTAB-FFT solver. The sphere has a radius equal to $\lambda/2$ and is characterized by ε_r = 2.4 - j0.5. The background medium is air, ε_{rb}=1. The sphere is illuminated by an incident plane wave, as shown in Figure 13(a), which is polarized along the x-direction and propagates along the $+z$-direction, i.e., $E^{inc} = \hat{x}e^{-jk_b z}$. The operating frequency is 300 MHz.

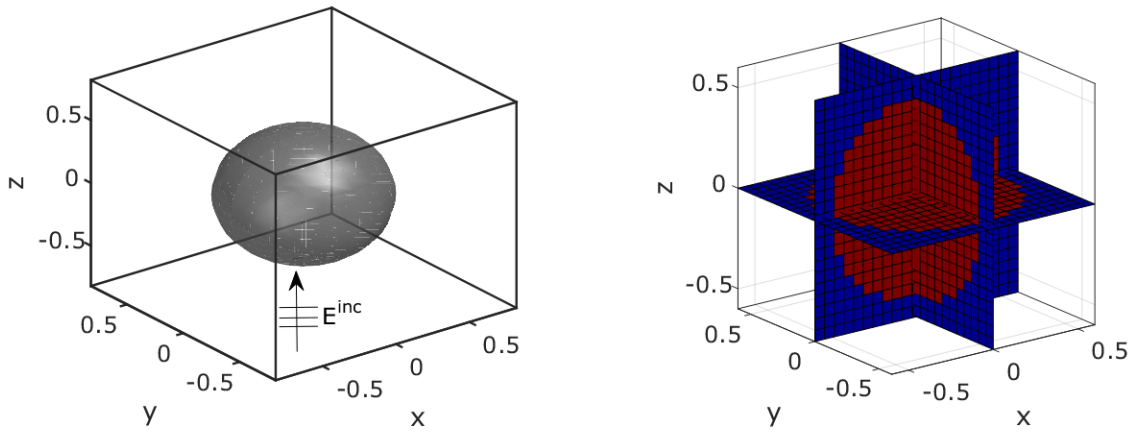

Figure 13 – Geometry of the dielectric sphere. (a) Continuous model. (b) 3D discretized model.

The bistatic radar cross section (RCS) is a useful parameter for the characterization of electromagnetic scattering. For a three-dimensional geometry, the radar cross section can be expressed as

$$\sigma_{3D} = \lim_{R\to\infty} 4\pi R^2 \frac{|\mathbf{E}^{sca}|^2}{|\mathbf{E}^{inc}|^2}, \tag{2.117}$$

where R is the far-field distance. In the 3D case, the RCS is usually normalized with respect to the wavelength λ. Bistatic RCS results of the dielectric sphere are compared with the analytical solution. MATLAB functions to compute the analytical expressions are available in Zhu (2022). In the EFIE solution with both DGFA and DGFE, the domain of interest D (1.2×1.2×1.2 m^3) is discretized into 21×21×21 square cells (9261 unknowns), as shown in Figure 13(b).

Figure 14 shows bistatic RCS versus scattering angles. Both DGFA and DGFE match the result of the analytical solution. Figure 15 shows the convergence curves of the BiCGSTAB-FFT solver by DGFA and DGFE. The forward solver takes 13 and 14 iterations through DGFA and DGFE, respectively, when the relative residual error becomes

less than 10^{-6}. Moreover, the CPU time of the BiCGSTAB-FFT solver is 6.45 seconds for the DGFA and 7.08 seconds for the DGFE.

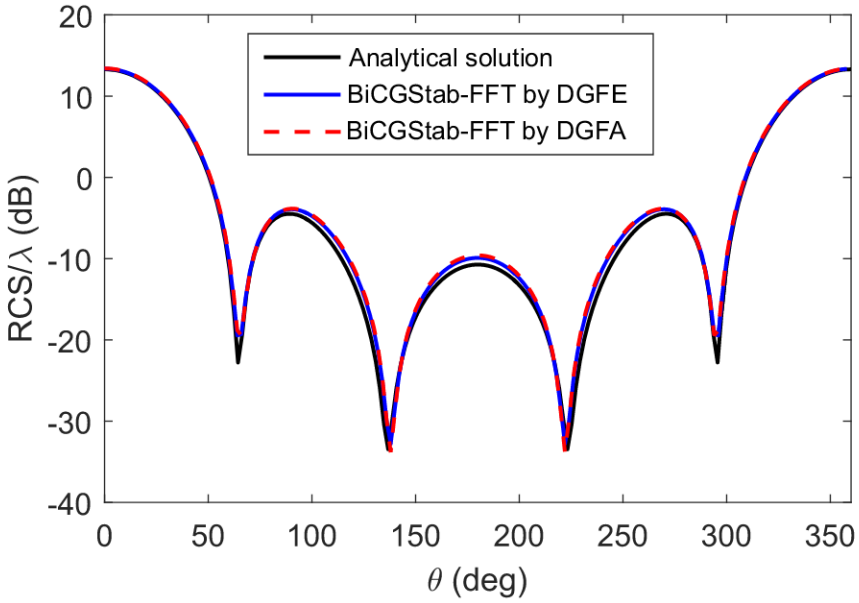

Figure 14 – Scattering cross section. Bistatic RCS of a dielectric sphere with radius $\lambda/2$ and $\varepsilon_r = 2.4 - j0.5$.

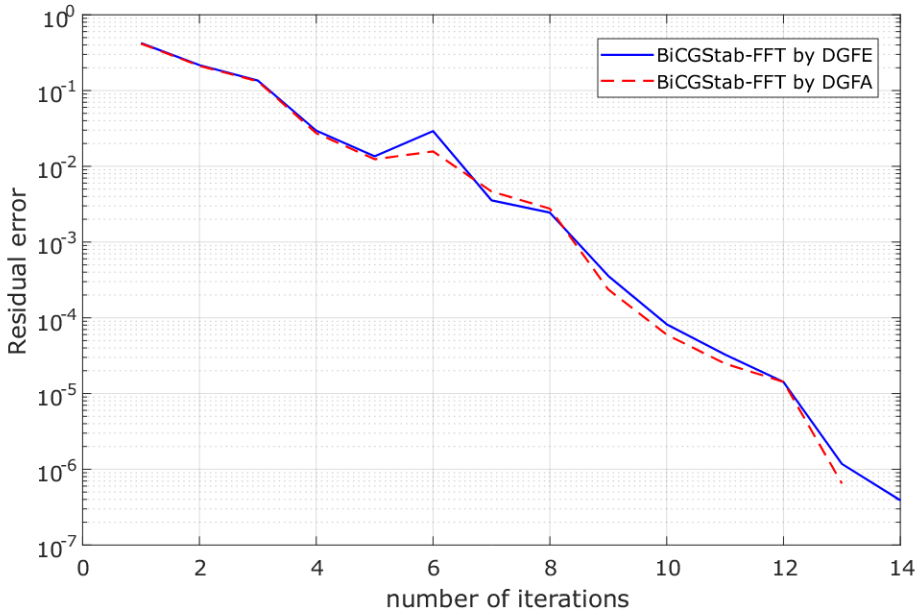

Figure 15 – Convergence curves of the BiCGSTAB-FFT algorithm.

2.6 Conclusion

In this chapter, we have presented the formulation and implementation of the two- and three-dimensional scattering forward problems. In the 2D case, the solution of the EFIE by using MoM and CG-FFT is a good approach for a full-wave EM solver. The performance of this implementation is superior to the conventional MoM. In the 3D

case, both DGFA and DGFE can be used to approximate the solution of the EFIE. In addition, we use an efficient iterative method combining the stabilized biconjugate-gradient (BiCGSTAB) method and the FFT algorithm to compute the electromagnetic fields in 3D problems. In this case, the difference between the solutions obtained through DGFA and DGFE is negligible.

The efficient solvers combining the iterative methods and the FFT algorithms imply symmetry in the domain of interest to preserve the convolutional symmetry in matrix coefficients. For the purpose of utilizing the FFT algorithms, we choose a rectangular domain embedding the scatterers. In this context, it is possible to discretize any domain with a minimum storage requirement without compromising the solution accuracy.

In reconstruction algorithms, the EM forward solver is important to generate numerical synthetic data, which is often used to test the performance of the inversion methods. Moreover, it can also be used to compute the corresponding forward problem during the optimization procedure in some inversion methods. In the next chapter, we will study some inversion methods based on forward solvers.

3 Inversion Methods

This chapter presents some inversion methods based on the conjugate gradient method, which are addressed to the reconstruction of permittivity profiles from measured scattering data. We present the forward model and inversion procedures. First, we present the original methods, then the proposed procedures and their implementation are described. Furthermore, the distorted-Born iterative method (DBIM) is also presented, which is used to compare the performance and computational complexity of the nonlinearized CGM.

3.1 Forward Problem Formulation

We consider that the domain of interest D is illuminated successively by N_i different incident electric fields E_l^{inc}, $l = 1, ..., N_i$. For each incidence, the scattered field is measured by an array of N_r different receivers located in the domain S, as shown in Figure 2. The receivers are located at $\mathbf{r}_m^s$, $m = 1, ..., N_r$. For each incidence l, the total electric field $E(\mathbf{r})$ at any point $\mathbf{r}$ can be expressed by the following integral equation

$$E_l(\mathbf{r}) = E_l^{inc}(\mathbf{r}) + k_b^2 \int_D G(\mathbf{r}, \mathbf{r}')\chi(\mathbf{r}')E_l(\mathbf{r}')d\mathbf{r}' \quad \mathbf{r} \in D, \tag{3.1}$$

where $\chi(\mathbf{r})$ is the contrast function that relates to the wave-scattering properties of the scatterer and $G(\cdot)$ denotes the Green's function of the background medium. From the total electric field in (3.1) the scattered field $E^{sca}(\mathbf{r})$ is defined by

$$E_l^{sca}(\mathbf{r}) = k_b^2 \int_D G(\mathbf{r}, \mathbf{r}')\chi(\mathbf{r}')E_l(\mathbf{r}')d\mathbf{r}' \quad \mathbf{r} \in S. \tag{3.2}$$

For convenience, we introduce the operators $\overline{\overline{G}}_S$ and $\overline{\overline{G}}_D$ for both 2D and 3D problems, which are defined as

$$k_b^2 \int_{\text{cell}} \frac{1}{4j} H_0^{(2)}\left(k_b \left|\mathbf{r} - \mathbf{r}'\right|\right) d\mathbf{r}' = \begin{cases} \overline{\overline{G}}_D^{2D} & \text{for} \quad \mathbf{r} \in D \\ \\ \overline{\overline{G}}_S^{2D} & \text{for} \quad \mathbf{r} \in S \end{cases}, \tag{3.3}$$

and

$$(k_b^2 + \nabla\nabla\cdot) \int_{\text{cell}} g(\mathbf{r}, \mathbf{r}')\overline{\overline{I}}\, d\mathbf{r}' = \begin{cases} \overline{\overline{G}}_D^{3D} & \text{for} \quad \mathbf{r} \in D \\ \\ \overline{\overline{G}}_S^{3D} & \text{for} \quad \mathbf{r} \in S \end{cases}. \tag{3.4}$$

Then the forward problem can be written in two different compact notations. The first form is referred to as field-type equations

$$\overline{E} = \overline{E}^{inc} + \overline{\overline{G}}_D \cdot \overline{\overline{\chi}} \cdot \overline{E} \tag{3.5}$$

$$\overline{E}^{sca} = \overline{\overline{G}}_S \cdot \overline{\overline{\chi}} \cdot \overline{E}, \tag{3.6}$$

here the total electric field is involved in both equations. By using the normalized contrast current density $J(\mathbf{r}) = \chi(\mathbf{r})E(\mathbf{r})$, the governing equations can be written in source-type equations form

$$\overline{J} = \overline{\overline{\chi}} \cdot (\overline{E} + \overline{\overline{G}}_D \cdot \overline{J}) \tag{3.7}$$

$$\overline{E}^{sca} = \overline{\overline{G}}_S \cdot \overline{J}. \tag{3.8}$$

The matrix $\overline{\overline{G}}_S$ is also known as the radiation operator matrix (Liu; Nie, 2019), which maps from the space of the induced current in domain D to the space of the scattered field on the receivers. Usually, Equations (3.5) and (3.7) are referred to as the state equations, and Equations (3.6) and (3.8) are referred to as data equations.

3.2 Conjugate Gradient Methods

The conjugate gradient method (CGM) recasts the inverse scattering problem as a minimization of a cost function. This starts with the field-type integral equations and applying the method of moments (Harrington, 1968; Richmond, 1965) leads to a nonlinear relation between the scattered field and the contrast. This approach results in a cost function that depends only on the error between measured data and the computed scattered field (Harada et al., 1995). The cost function is defined by

$$F(\overline{\overline{\chi}}) = W \sum_{l=1}^{N_i} \| \overline{\rho}_l \|_S^2 , \tag{3.9}$$

where $\overline{\rho}_l = \overline{E}_l^{sca} - \overline{\overline{G}}_S \cdot \overline{\overline{\chi}} \cdot \overline{E}_l$ is the residual error and W is a weighting coefficient given by

$$W = \left(\sum_{l=1}^{N_i} \left\| \overline{E}_l^{sca} \right\|_S^2 \right)^{-1} . \tag{3.10}$$

The solution of contrast profile $\overline{\overline{\chi}}$ is obtained by minimizing (3.9); according to Lobel et al. (1996), this consists of iterative construction of sequences $\{\overline{\overline{\chi}}_n\}$ as follows

$$\overline{\overline{\chi}}_n = \overline{\overline{\chi}}_{n-1} + \alpha_n \overline{\overline{D}}_n, \tag{3.11}$$

where $\overline{\overline{D}}_n$ is the updated search direction, which is a diagonal matrix, formed by the vector $\overline{d}_n$. And α is a complex parameter (weight factor), which is obtained by

$$\alpha_n = \text{argmin}_\alpha \{F(\overline{\overline{\chi}}_n + \alpha \overline{d}_n)\}. \tag{3.12}$$

According to Lobel et al. (1996), the Polak-Ribière search direction is used in the conjugate gradient method, then the update direction $\overline{d}_n$ is given by

$$\overline{d}_n = \overline{g}_n + \frac{\text{Re}[(\overline{g}_n - \overline{g}_{n-1})^H \cdot \overline{g}_n]}{\left\| \overline{g}_{n-1} \right\|_D^2} \overline{d}_{n-1}, \tag{3.13}$$

where the superscript H denotes the Hermitian operator and $\overline{g}_n$ is the gradient of the cost function, which is calculated by the Fréchet derivative. Two main approaches to calculate the gradient direction $\overline{g}_n$ can be distinguished: the nonlinearized and linearized approaches. These formulations are described in the next two subsections.

3.2.1 Nonlinearized approach

The CGM for solving inverse scattering problems was originally presented by Lobel et al. (1996). This method recasts the nonlinear inverse problem as a minimization of a cost function. The nonlinearized CGM considers the total electric field as an additional parameter in the calculation of the gradient direction of the cost function. Following the procedure used in Lobel et al. (1996), we have

$$\alpha_n = \frac{\sum_{l=1}^{N_i} \left\langle \overline{\rho}_{l,n}, \overline{\overline{V}}_{l,n} \right\rangle_S}{\sum_{l=1}^{N_i} \left\| \overline{\overline{V}}_{l,n} \right\|_S^2} \tag{3.14}$$

where

$$\overline{\overline{V}}_{l,n} = \overline{\overline{G}}_S \cdot [\overline{\overline{\mathcal{L}}}_{(\chi_{n-1})}]^T \cdot \overline{\overline{D}}_n \cdot \overline{E}_{l,n}, \tag{3.15}$$

where $\overline{\overline{\mathcal{L}}}_{(\chi_{n-1})} = (\overline{\overline{I}} - \overline{\overline{G}}_D \cdot \overline{\overline{\chi}}_{n-1})^{-1}$ and the superscript T denotes the transpose operator. The electric field $\overline{E}_{l,n}$ is obtained from (3.5) with the contrast taken equal to $\overline{\overline{\chi}}_{n-1}$. The gradient direction $\overline{g}_n$ of (3.9) is determined by the Fréchet derivative

$$\left\langle \nabla F(\overline{\overline{\chi}}_{n-1}), \overline{d}_{n-1} \right\rangle_D = \sum_{l=1}^{N_i} \left. \frac{\partial \left\| \overline{\rho}_{l(\overline{\overline{\chi}}_n)} \right\|_S^2}{\partial \alpha_n} \right|_{\alpha_n = 0}, \tag{3.16}$$

which is equivalent to

$$\left\langle \nabla F(\overline{\overline{\chi}}_{n-1}), \overline{d}_{n-1} \right\rangle_D = -W \sum_{l=1}^{N_i} \left\langle \overline{\rho}_{l,n}, \overline{\overline{V}}_{l,n} \right\rangle_S . \tag{3.17}$$

By developing (3.17), the gradient of the cost function is obtained as

$$\overline{g}_n = -W \sum_{l=1}^{N_i} \left[\mathrm{diag}(\overline{E}_{l,n}) \cdot \overline{\overline{\mathcal{L}}}_{(\chi_{n-1})} \right]^* \cdot \overline{\overline{G}}_S^H \cdot \overline{\rho}_{l,n}. \tag{3.18}$$

where the superscript * denotes the complex conjugate operator. Finally, the CGM depends on an initial guess $\overline{\overline{\chi}}_0$. This initial solution can be calculated using the back-propagation method (Lobel et al., 1996; Belkebir; Chaumet; Sentenac, 2005). The formulation of the back-propagation procedure can be found in Appendix B.

3.2.2 Linearized approach

In the linearized iterative inversion approach, the cost function is given by (3.9) and the optimization procedure is similar to the nonlinearized approach. In the linearized CGM, the total electric field is estimated from the best available contrast (Chaumet; Belkebir, 2009; Mudry et al., 2012), i.e., $\overline{E}_{l,n} \approx \overline{E}_{l,n-1}$. According to Chaumet and Belkebir (2009) the unique minimum of the cost function $F(\alpha_n)$ is reached for

$$\alpha_n = \frac{\sum_{l=1}^{N_i} \left\langle \overline{\rho}_{l,n},\ \overline{\overline{G}}_S \cdot \overline{\overline{D}}_n \cdot \overline{E}_{l,n} \right\rangle_S}{\sum_{l=1}^{N_i} \left\| \overline{\overline{G}}_S \cdot \overline{\overline{D}}_n \cdot \overline{E}_{l,n} \right\|_S^2}. \tag{3.19}$$

where

$$\overline{\rho}_{l,n} = \overline{E}^{sca} - \overline{\overline{G}}_S \cdot \overline{\overline{\chi}}_{n-1} \cdot \overline{E}_{l,n}. \tag{3.20}$$

The contrast is updated at each iteration by (3.11). Assuming that the total electric field $\overline{E}_l$ do not change, the gradient of the cost function is obtained as

$$\overline{g}_n = -W \sum_{l=1}^{N_i} (\overline{E}_{l,n})^* \odot \overline{\overline{G}}_S^H \cdot \overline{\rho}_{l,n}. \tag{3.21}$$

The inversion algorithm is completed with the estimation the initial guess, e.g., using the back-propagation procedure (Belkebir; Chaumet; Sentenac, 2005).

Compared with the nonlinearized approach, the gradient direction in (3.21) is simpler and therefore less time-consuming than the gradient obtained in (3.18). Note that the linearized approach does not involve the contrast variable in the gradient calculation, since the total electric field is fixed at each iteration. However, this linearized CGM works for slightly nonlinear ISPs. Therefore, this linear approximation has a limited range of applicability.

3.3 Distorted-Born Iterative Method

In the distorted Born iterative method (DBIM), the cost function is chosen as the quadratic error of mismatch of measured scattered field and computed one. In addition, a Tikhonov regularization term is added to the cost function to stabilize the optimization procedure. The cost function is defined as

$$f(\Delta\overline{\overline{\chi}}) = \sum_{l=1}^{N_i} \left\| \overline{E}_l^{sca} - \overline{\overline{G}}_S \cdot \overline{\overline{\chi}} \cdot \overline{E}_l^b - \overline{\overline{G}}_{bs} \cdot \Delta\overline{\overline{\chi}} \cdot \overline{E}_l^b \right\|_S^2 + \gamma \| \Delta\overline{\overline{\chi}} \|_D^2 , \tag{3.22}$$

where $\overline{E}_l^{sca}$ is the measured scattered field, $\overline{E}_l^b$ represents the incident electric field in the presence of the inhomogeneous background medium and $\overline{\overline{G}}_{bs}$ is the inhomogeneous Green's function for the background medium contrast, which is given by Remis and van den Berg (2000)

$$\overline{\overline{G}}_{bs,n} = \overline{\overline{G}}_S \cdot (\overline{\overline{I}} - \overline{\overline{\chi}}_n \cdot \overline{\overline{G}}_D)^{-1}. \tag{3.23}$$

The DBIM needs to solve the forward problem to calculate $\overline{E}_{l,n}^b$ at each iteration step, which can be obtained as

$$\overline{E}_{l,n}^b = (\overline{\overline{I}} - \overline{\overline{G}}_D \cdot \overline{\overline{\chi}}_n)^{-1} \cdot \overline{E}_l^{inc}. \tag{3.24}$$

Equation (3.22) is linear for $\Delta\overline{\overline{\chi}}$, however, a regularization procedure should be required in solving this linear equation due to ill-posedness. By minimizing (3.22), we obtain the following matrix equation system

$$(\overline{\overline{A}}^H \cdot \overline{\overline{A}} + \gamma\overline{\overline{I}}) \cdot \Delta\overline{\overline{\chi}}_n = \overline{\overline{A}}^H \cdot \Delta\overline{E}_{l,n}^{sca}, \tag{3.25}$$

where $\overline{\overline{A}} = \overline{\overline{G}}_{bs,n} \cdot \overline{E}_{l,n}^b$, $\Delta\overline{E}_{l,n}^{sca} = \overline{E}_l^{sca} - \overline{\overline{G}}_S \cdot \overline{\overline{\chi}}_n \cdot \overline{E}_{l,n}^b$, and γ is the Tikhonov regularization parameter. Once $\Delta\overline{\overline{\chi}}_n$ has been determined, the contrast solution is updated by

$$\overline{\overline{\chi}}_{n+1} = \overline{\overline{\chi}}_n + \Delta\overline{\overline{\chi}}_n. \tag{3.26}$$

In the DBIM, the forward solver is also efficiently implemented by iterative methods combined with FF algorithms. Moreover, it is possible to solve (3.25) using the conjugate gradient method, which requires the Fréchet derivative and its adjoint operator (Cui et al., 2001).

3.4 Efficient Conjugate Gradient Methods

In this section, three methods for solving the electromagnetic inverse scattering problem will be introduced. All these inversion methods are applied to reconstruct dielectric scatterers. First, we introduce an efficient implementation of the nonlinearized CGM, which adopts the FFT algorithms for efficient matrix-vector multiplication, because the convolutional kernels of integral equations produce a discrete type convolution, as described in Chapter 2. With these features, we can use iterative methods to efficiently calculate of total electric field and the gradient direction in the nonlinearized CGM. Secondly, a new inversion method is proposed, the subspace-based conjugate-gradient method (S-CGM), which has better convergence and accuracy than the linearized CGM. Finally, a fast CGM based on the approximation of the inverse matrix by using Neumann series expansion is introduced.

3.4.1 Efficient implementation of the CGM

In the formulation presented in subsection 3.2.1, the total field $\overline{E}_{l,n}$ can be efficiently obtained by a forward solver using iterative methods and FFT algorithms. However, direct multiplication operations in (3.15) and (3.18) remove the convolutional symmetry of the matrix coefficients in $\overline{\overline{\mathcal{L}}}_{(\chi_{n-1})}$. Without proper treatment, these procedures can make the computational cost-prohibitive, even for small-scale problems. In the worst case, a direct matrix inversion is required. Therefore, the bottleneck is in operations involving the inverse matrix $\overline{\overline{\mathcal{L}}}_{(\chi_{n-1})}$. We avoid the calculation and storage of $\overline{\overline{\mathcal{L}}}_{(\chi_{n-1})}$ by using an efficient forward solver twice at each iteration step. Instead of storing the whole matrix $\overline{\overline{G}}_{D}$, the convolutional kernels of the integral equations can be performed in $O(N \log N)$ operations using FFT algorithms. The CG-FFT method is used for 2D-TM problems, whereas the BiCGSTAB-FFT method is used for solving 3D problems. In order to implement the reconstruction algorithm, we propose to rewrite Equations (3.15) and (3.18) as follows

$$\overline{\overline{V}}_{l,n} = \overline{\overline{U}}_{s,n} \cdot \overline{\overline{D}}_{n} \cdot \overline{E}_{l,n} \tag{3.27}$$

and

$$\overline{g}_{n} = -W \sum_{l=1}^{N_i} (\overline{E}_{l,n})^{*} \odot \overline{\overline{U}}^{H}_{s,n} \cdot \overline{\rho}_{l,n}, \tag{3.28}$$

where $\overline{\overline{U}}_{s,n}$ is computed by iterative methods combined with FFT procedures satisfying

$$\overline{\overline{U}}_{s,n} = \overline{\overline{G}}_{S} + \overline{\overline{G}}_{D} \cdot \overline{\overline{\chi}}_{n-1} \cdot \overline{\overline{U}}_{s,n}. \tag{3.29}$$

or

$$\overline{\overline{U}}_{s,n} = \overline{\overline{G}}_{S} \cdot (\overline{\overline{I}} - \overline{\overline{\chi}}_{n-1} \cdot \overline{\overline{G}}_{D})^{-1}. \tag{3.30}$$

The implementation of the efficient CGM is summarized in Algorithm 3.

Algorithm 3: Efficient Conjugate Gradient Method

Step 1: Calculate $\overline{\overline{G}}_D$ and $\overline{\overline{G}}_S$

Step 2: Initial iteration, $n = 0$

Choose initial guess $\overline{\overline{\chi}}_0$
Initialize the search directions $\overline{d}_0$
Obtain $\overline{E}_0$ and $\overline{\overline{U}}_{s,0}$

Step 3: Iteration $n = n + 1$

Calculate the gradient $\overline{g}_n$ by using (3.28)
Determine the search directions from (3.13)
Calculate the weight factor α_n from (3.14)
Update $\overline{\overline{\chi}}_n = \overline{\overline{\chi}}_{n-1} + \alpha_n \overline{\overline{D}}_n$
Update $\overline{E}_n$ and $\overline{\overline{U}}_{s,n}$

Step 4: If predetermined convergence criterion is satisfied, then STOP. Otherwise, go to **Step 3**.

The computational complexity of this CGM implementation is dominated by the forward solvers and the Fréchet derivative matrix operations. Note that the total electric field $\overline{E}$ is of size $N \times N_i$ and the operator $\overline{\overline{U}}_s$ is of size $N_r \times N$, then the total number of calls to the forward solver in Algorithm 3 is $(N_i + N_r)$. Therefore, the computational cost of the inversion algorithm at each iteration step becomes

$$C_{\text{CGM}} \sim N_{\text{for}} N_c (N_i + N_r) N \log N + N_i N_r N, \tag{3.31}$$

where N_{for} is the number of iterations of the forward solver, N_c is a constant coefficient due to FFT, which depends on the FFT routine, and N is the total number of discretized cells. The second term of the right-hand side of (3.31) is the contribution of calculating the gradient direction of the cost function.

In comparison, the distorted Born iterative method (DBIM) has a computational complexity of

$$C_{\text{DBIM}} \sim N_{\text{for}} N_c (N_i + N_r) N \log N + N_{\text{CG}}^{\text{TK}} N_i N_r N, \tag{3.32}$$

where $N_{\text{CG}}^{\text{TK}}$ is the number of iterations to solve the matrix equation of the Tikhonov regularization (Cui et al., 2001). The forward problems in the CGM and the DBIM are equivalents, except that the DBIM considers an inhomogeneous background medium, while the CGM assumes a homogeneous background, and solves the forward problem to find the total field inside the domain and calculate the gradient direction. Note that the first term of the right-hand side of (3.31) and (3.32) corresponds to the computation of the forward solvers, which dominates the number of operations for small and moderately sized problems. However, the dominance of the complexity of the second term is relevant for large-scale problems. Regarding storage efficiency, the storage requirement of the inversion methods is proportional to $(N_i + N_r)N$.

3.4.2 Subspace-based conjugate gradient method

In this contribution, a new inversion method denoted as the subspace-based conjugate gradient method (S-CGM), is proposed. This method is based on the ideas of linearized CGM and the S-VBIM proposed by Liu and Nie (2019). As in the S-VBIM, we retrieve the deterministic part of the variational induced current by performing the singular value decomposition (SVD) of the radiation operator matrix $\overline{\overline{G}}_S$. In the S-CGM, the gradient calculation is derived from the linearized CGM.

In order to improve the total field estimation, we propose the following scheme to update the total field

$$\overline{E}_{l,n} = \overline{E}_{l,n-1} + \delta\overline{E}. \tag{3.33}$$

Considering small variations of the total field, we have

$$\overline{E}_{l,n} = \overline{E}_{l,n-1} + \overline{\overline{G}}_D \cdot \delta(\overline{\overline{\chi}} \cdot \overline{E}), \tag{3.34}$$

where the term $\delta(\overline{\overline{\chi}} \cdot \overline{E})$ can be understood as the variational induced current $\delta\overline{J}$. Since the radiation operator matrix $\overline{\overline{G}}_S$ is a compact operator (Chen, 2018), which has an infinite number of small singular values accumulating at zero, the induced current $\delta\overline{\overline{J}}$ can be divided into two parts: a portion of the variational induced current that produces the scattered field on receiver and a portion that produces zero or negligible scattered fields (Liu; Nie, 2019). Thus, the variational induced current $\delta\overline{J}$ cannot be uniquely retrieved from the scattered field data.

The SVD of $\overline{\overline{G}}_S$ is represented as $\overline{\overline{G}}_S = \sum_i \bar{u}_i \sigma_i \bar{v}_i^*$ and $\overline{\overline{G}}_S \cdot \bar{v}_i = \sigma_i \bar{u}_i$. This means that the radiating portion of the variational induced current is in the span of right singular vectors $\bar{v}_i$ that corresponds to the nonzero singular values, whereas the non-radiating portion is in the span of the orthogonal subspace of right singular vectors $\bar{v}_i$ that corresponds to the zero singular values (Ye; Chen, 2017). In practice, the retrieval of the portions of the induced current is difficult due to the fact that the scattered data are often contaminated with noise. We can order the singular values in a descending order such that, $\sigma_1 \geq \sigma_2 \geq \cdots \geq \sigma_{L_0} \geq \sigma_{L_0+1} = \sigma_{L_0+2} = \cdots = \sigma_N = 0$, where it is assumed that there are a total number of L_0 nonvanishing singular values (Chen, 2018). A part of the variational radiating induced current can be retrieve by using the largest L leading singular values, where L can be any integer as long as it is no larger than L_0

$$\delta\overline{J}^d = \sum_{i=1}^{L} \frac{\bar{u}_i^H \cdot \delta\overline{E}^{sca}}{\sigma_i} \bar{v}_i, \tag{3.35}$$

where $\delta\overline{E}^{sca}$ represents the variational scattered field, which is given by

$$\delta\overline{E}^{sca} = \overline{E}^{sca} - \overline{E}^{sca}_{n-1}. \tag{3.36}$$

The induced current $\delta\overline{J}^d$ is known as the deterministic part of the variational induced current (Liu; Nie, 2019) and it contributes to the major part of the scattered fields on the receiver. It is worth mentioning that both S-VBIM and S-DBIM minimize a cost function in the sense of least squares to solve the contrast difference $\delta(\overline{\overline{\chi}})$, while in the S-CGM the optimization variable is directly the contrast matrix $\overline{\overline{\chi}}$. Although the S-CGM does not use any regularization procedure, e.g., the Tikhonov regularization, the integer value L serves as a regularization parameter. The choice of the optimal value of L depends on the noise level and the criteria used to determine it are discussed in Chen (2010), Zhong and Chen (2011), and Ye and Chen (2017). Finally, the proposed iteration procedure of the S-CGM is as follows

Algorithm 4: Subspace-Based Conjugate-Gradient Method

Step 1: Calculate $\overline{\overline{G}}_D$ and $\overline{\overline{G}}_S$

Calculate the thin SVD of $\overline{\overline{G}}_S$ and choose the appropriate value of L

Step 2: Initial iteration, $n = 0$

Choose initial guess $\overline{\overline{\chi}}_0$

Initialize the search directions $\overline{d}_0$

Step 3: Iteration $n = n + 1$

Calculate the electric field

$$\overline{E}_{l,n-1} = (\overline{\overline{I}} - \overline{\overline{G}}_D \cdot \overline{\overline{\chi}}_{n-1})^{-1} \cdot \overline{E}_l^{inc}. \tag{3.37}$$

Calculate the deterministic part of the variational induced current using

$$\delta\overline{J}_l^d = \sum_{i=1}^{L} \frac{\bar{u}_i^H \cdot (\overline{E}_l^{sca} - \overline{\overline{G}}_S \cdot \overline{\overline{\chi}}_{n-1} \cdot \overline{E}_{l,n-1})}{\sigma_i} \bar{v}_i. \tag{3.38}$$

Then, update the total field

$$\overline{E}_l = \overline{E}_{l,n-1} + \overline{\overline{G}}_D \cdot \delta\overline{J}_l^d. \tag{3.39}$$

Calculate the gradient

$$\overline{g}_n = -W \sum_{l=1}^{N_i} (\overline{E}_l)^* \odot \overline{\overline{G}}_S^H \cdot \overline{\rho}_{l,n}. \tag{3.40}$$

Determine the search directions from (3.13)

Calculate the weight factor α_n

$$\alpha_n = \frac{\sum_{l=1}^{N_i} \left\langle \overline{\rho}_{l,n},\ \overline{\overline{G}}_S \cdot \overline{\overline{D}}_n \cdot \overline{E}_l \right\rangle_S}{\sum_{l=1}^{N_i} \left\| \overline{\overline{G}}_S \cdot \overline{\overline{D}}_n \cdot \overline{E}_l \right\|_S^2}. \tag{3.41}$$

Update the contrast profile: $\overline{\overline{\chi}}_n = \overline{\overline{\chi}}_{n-1} + \alpha_n \overline{\overline{D}}_n$

Step 4: Evaluate (3.9). If predetermined convergence criterion is satisfied, then STOP. Otherwise, go to **Step 3**.

The proposed Algorithm 4 needs to calculate of SVD of the radiation operator matrix only once when initializing the algorithm. The size of matrix $\overline{\overline{G}}_S$ is $N_r \times N$. Usually, the number of discretized cells is greater than the number of receivers, i.e., $N \gg N_r$. The computational complexity of a thin SVD is $O(N_r^2 N)$ (Stewart, 1998). Therefore, the additional computational cost is very small. Furthermore, the matrix-vector multiplication in the right-hand side of (3.39) can be performed in $O(N \log N)$ operations and the electric field in (3.37) can be efficiently solved by using an iterative method and FFT algorithms, as demonstrated in Chapter 2.

3.4.3 Fast CGM based on inverse matrix approximation

In this approach, we propose to reduce the consumption time of the forward solvers by introducing an approximation of the inverse matrix. We have

$$\overline{E} = (\overline{\overline{I}} - \overline{\overline{G}}_D \cdot \overline{\overline{\chi}})^{-1} \cdot \overline{E}^{inc}. \tag{3.42}$$

Consider the series expansion (Neumman series) of the inverse matrix

$$(\overline{\overline{I}} - \overline{\overline{G}}_D \cdot \overline{\overline{\chi}})^{-1} = (\overline{\overline{I}} + (\overline{\overline{G}}_D \cdot \overline{\overline{\chi}}) + (\overline{\overline{G}}_D \cdot \overline{\overline{\chi}})^2 + \cdots). \tag{3.43}$$

By substituting (3.43) in (3.42), we obtain

$$\overline{E} = (\overline{\overline{I}} + (\overline{\overline{G}}_D \cdot \overline{\overline{\chi}}) + (\overline{\overline{G}}_D \cdot \overline{\overline{\chi}})^2 + \cdots) \cdot \overline{E}^{inc}. \tag{3.44}$$

For example, using only the linear term $(\overline{\overline{G}}_D \cdot \overline{\overline{\chi}})$ of the expansion the residual error in the conjugate gradient method can be calculate by

$$\overline{\rho}_{l(\overline{\overline{\chi}})} = \overline{E}_l^{sca} - \overline{\overline{G}}_S \cdot \overline{\overline{\chi}} \cdot (\overline{\overline{I}} + \overline{\overline{G}}_D \cdot \overline{\overline{\chi}}) \cdot \overline{E}_l^{inc}. \tag{3.45}$$

As a result, the total electric field is obtained from (3.44) using only the linear term. However, the inverse problem is still nonlinear for the unknown $\overline{\overline{\chi}}$. The inherent nonlinearity of the inverse scattering problem means that for high dielectric contrasts this approximation is not valid. In order to improve this approximation, we consider small variations of the total and scattered fields as follows

$$\Delta\overline{E} = \overline{\overline{G}}_D \cdot \Delta(\overline{\overline{\chi}} \cdot \overline{E}) \tag{3.46}$$

$$\Delta\overline{E}^{sca} = \overline{\overline{G}}_S \cdot \Delta(\overline{\overline{\chi}} \cdot \overline{E}), \tag{3.47}$$

where $\Delta(\overline{\overline{\chi}} \cdot \overline{E})$ can be defined by product rule differentiation

$$\Delta(\overline{\overline{\chi}} \cdot \overline{E}) = \Delta\overline{\overline{\chi}} \cdot \overline{E} + \overline{\overline{\chi}} \cdot \Delta\overline{E}. \tag{3.48}$$

Substituting (3.48) and (3.44) into (3.46) and (3.47) produces

$$\Delta\overline{E}_{l,n} = (\overline{\overline{I}} + (\overline{\overline{G}}_D \cdot \overline{\overline{\chi}}_{n-1}) + (\overline{\overline{G}}_D \cdot \overline{\overline{\chi}}_{n-1})^2 + \cdots) \cdot \overline{\overline{G}}_D \cdot \Delta\overline{\overline{\chi}} \cdot \overline{E}_{l,n-1} \tag{3.49}$$

$$\Delta\overline{E}^{sca}_{l,n} = \overline{\overline{G}}_S \cdot (\overline{\overline{I}} + (\overline{\overline{\chi}}_{n-1} \cdot \overline{\overline{G}}_D) + (\overline{\overline{\chi}}_{n-1} \cdot \overline{\overline{G}}_D)^2 + \cdots) \cdot \Delta\overline{\overline{\chi}} \cdot \overline{E}_{l,n-1}. \tag{3.50}$$

For the nth iteration, the contrast variation is obtained from the search direction and the weight factor as $\Delta\overline{\overline{\chi}}_n = \alpha_n \overline{\overline{D}}_n$, and the update of the fields at each iteration is given by

$$\overline{E}_{l,n} = \overline{E}_{l,n-1} + \Delta\overline{E}_{l,n} \tag{3.51}$$

$$\overline{E}^{sca}_{l,n} = \overline{E}^{sca}_{l,n-1} + \Delta\overline{E}^{sca}_{l,n}. \tag{3.52}$$

Following the procedures of the gradient conjugate method presented in the previous subsections, we have

$$\alpha_n = \frac{\sum_{l=1}^{N_i} \left\langle \overline{\rho}_{l,n}, \overline{\overline{U}}_{s,n} \cdot \overline{\overline{D}}_n \cdot \overline{E}_{l,n} \right\rangle_S}{\sum_{l=1}^{N_i} \left\| \overline{\overline{U}}_{s,n} \cdot \overline{\overline{D}}_n \cdot \overline{E}_{l,n} \right\|_S^2} \tag{3.53}$$

where

$$\overline{\overline{U}}_{s,n} = \overline{\overline{G}}_S \cdot (\overline{\overline{I}} + (\overline{\overline{\chi}}_{n-1} \cdot \overline{\overline{G}}_D) + (\overline{\overline{\chi}}_{n-1} \cdot \overline{\overline{G}}_D)^2 + \cdots). \tag{3.54}$$

Finally, the gradient direction is obtained by

$$\overline{g}_n = -W \sum_{l=1}^{N_i} (\overline{E}_{l,n})^* \odot \overline{\overline{U}}^H_{s,n} \cdot \overline{\rho}_{l,n}. \tag{3.55}$$

The accuracy of the approximation depends on the number of order terms in the expansion. In addition, the matrix-vector products can be efficiently performed by FFT algorithms. This procedure is a good approximation for scatterers slightly above the range of the weak scattering (i.e., low dielectric contrast). To be specific, the convergence is determined by $\left\| \overline{\overline{G}}_D \cdot \overline{\overline{\chi}} \right\| \leq 1$.

The implementation of the fast CGM is summarized as follows

Algorithm 5: Fast Conjugate Gradient Method

Step 1: Calculate $\overline{\overline{G}}_D$ and $\overline{\overline{G}}_S$

Step 2: Initial iteration, $n = 0$

Choose initial guess $\overline{\overline{\chi}}_0$
Initialize the search directions $\overline{d}_0$
Obtain $\overline{E}_0$ and $\overline{E}_0^{sca}$
Calculate the residual error

Step 3: Iteration $n = n + 1$

Calculate the gradient $\overline{g}_n$ by using (3.55)
Determine the Polak–Ribière conjugate-gradient search directions from (3.13)
Calculate the weight factor α_n from (3.53)
Update $\overline{\overline{\chi}}_n = \overline{\overline{\chi}}_{n-1} + \alpha_n \overline{\overline{D}}_n$
Update $\overline{E}_n$ and $\overline{E}_n^{sca}$ from (3.51) and (3.52), respectively.

Step 4: If predetermined convergence criterion is satisfied, then STOP. Otherwise, go to **Step 3**.

4 Two-Dimensional (2D) Inversion

In this chapter, some 2D numerical results are presented to demonstrate the performance of efficient algorithms using different conjugate gradient approaches. We consider the reconstruction of strong scatterers applying the full-wave iterative inversion methods. Moreover, a comparison of the computational time between the efficient conjugate gradient algorithm and the original version is depicted. Finally, numerical tests for reconstruction with the approximation of the gradient are presented. In this case, we explore the validity range of the approximations for solving inverse scattering problems.

4.1 Test with synthetic data: "Austria" profile

This section provides some two-dimensional numerical results to show the performance of the inversion algorithms proposed in Chapter 3. We choose the benchmark problem known as the "Austria" problem (Chen, 2010; Ye; Chen, 2017). The geometry of the "Austria" profile is shown in Figure 16. The domain of interest is a 2×2 m^2 square centered at the origin. The simulated scatterers consist of two discs and one ring. The discs of radius 0.2 m are centered at (0.3, 0.6) m and $(-0.3, 0.6)$ m. The ring has an exterior radius of 0.6 m and an inner radius of 0.3 m, and is centered at $(0, -0.2)$ m. In all numerical examples the synthetic data are generated by the CG-FFT-based forward solver.

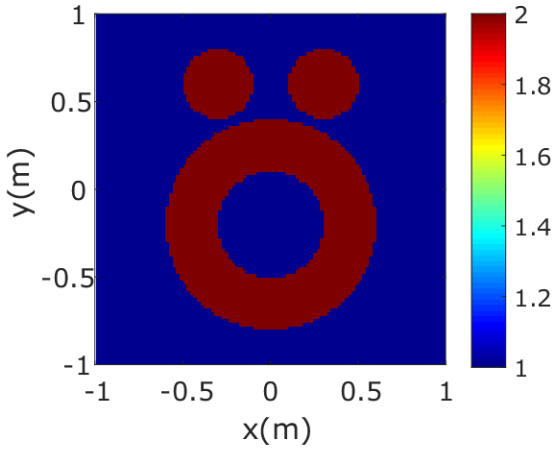

Figure 16 – "Austria" profile.

4.1.1 Reconstruction results using the efficient CGM

In this test, we consider the "Austria" profile with relative permittivity equal to 2 and the background medium is air, $\varepsilon_{rb}= 1$. An array of transmitters–receivers is placed on

a circle with radius 3 m centered at the origin. Each transmitter (line source) illuminates the domain with an operating frequency of 400 MHz. The scattered data are generated by the CG-FFT-based forward solver, the whole set of scattered field data collected is size $N_r \times N_i$ (32×16), where N_r and N_i are the number of receivers and incidences, respectively. The scattered data are corrupted with additive white Gaussian noise (AWGN). The noise level is quantified by $(\|\bar{e}_l\| / ||\overline{E}^{sca}_{l,MoM}||) \times 100\%$, where $\overline{E}^{sca}_{l,MoM}$ is the synthetic scattered data for the lth incidence, so that $\overline{E}^{sca}_{l} = \overline{E}^{sca}_{l,MoM} + \bar{e}_l$. As in (Chen, 2010), in the forward problem solver, the domain D is discretized into 100×100 cells, which is greater than the used for solving the inverse problem (64×64 cells) in order to avoid the inverse crime. In addition, the scattered data are generated by the MoM using a strict value of tolerance $\epsilon = 10^{-6}$, whereas in the computed forward problems (inversion procedure) a moderate tolerance value of $\epsilon = 10^{-3}$ on the residual error is used.

Reconstruction results using the efficient CGM (nonlinearized approach) for synthetic data in the absence of noise are shown in Figure 17. A *priori* information about the problem is that the unknown contrast is nonnegative. This *prior* information is widely used in the literature (Van den Berg; Kleinman, 1997; Chen, 2010). The results show an accurate reconstruction of the location and shape of the objects.

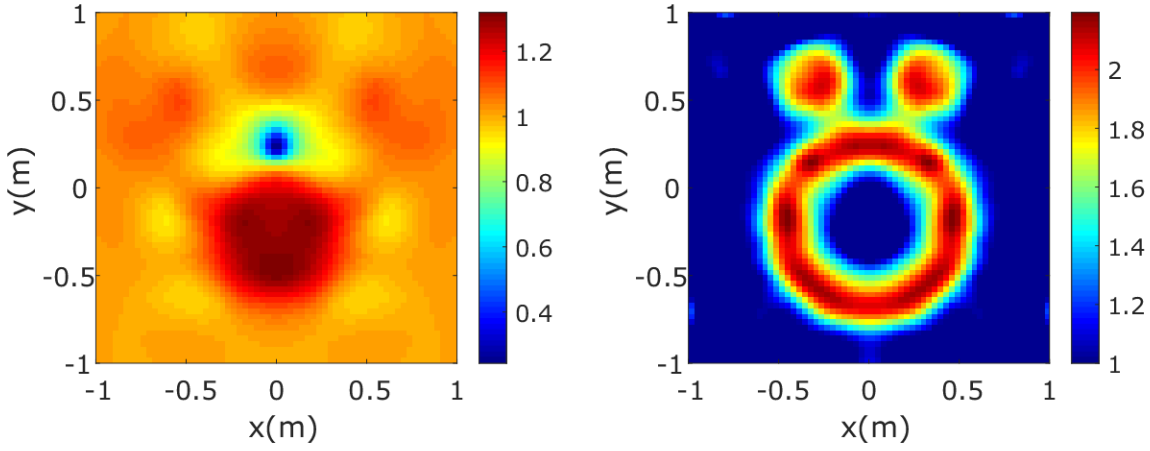

Figure 17 – Reconstructed relative permittivity profile. (a) Initial guess with back-propagation. (b) Reconstructed profile for the efficient CGM after 20 iterations.

In order to study the robustness of the efficient CGM (nonlinearized CGM) against noise in the scattered data, the reconstruction results for 10%, 30%, and 50% additive white Gaussian noise are presented in Figure 18. In all numerical experiments, the nonnegativity of the unknown contrast is assumed, that is, the real part satisfying: $\mathcal{R}(\chi) \geq 0$.

In order to evaluate the quality of the reconstructed images, we define the permittivity profile error as follows

$$ERR_{\varepsilon} = \frac{\left\| \bar{\bar{\varepsilon}}^{rec} - \bar{\bar{\varepsilon}}^{true} \right\|_D}{\left\| \bar{\bar{\varepsilon}}^{true} \right\|_D}, \tag{4.1}$$

where $\bar{\bar{\varepsilon}}^{rec}$ is the reconstructed relative permittivity profile and the $\bar{\bar{\varepsilon}}^{true}$ is the true relative permittivity.

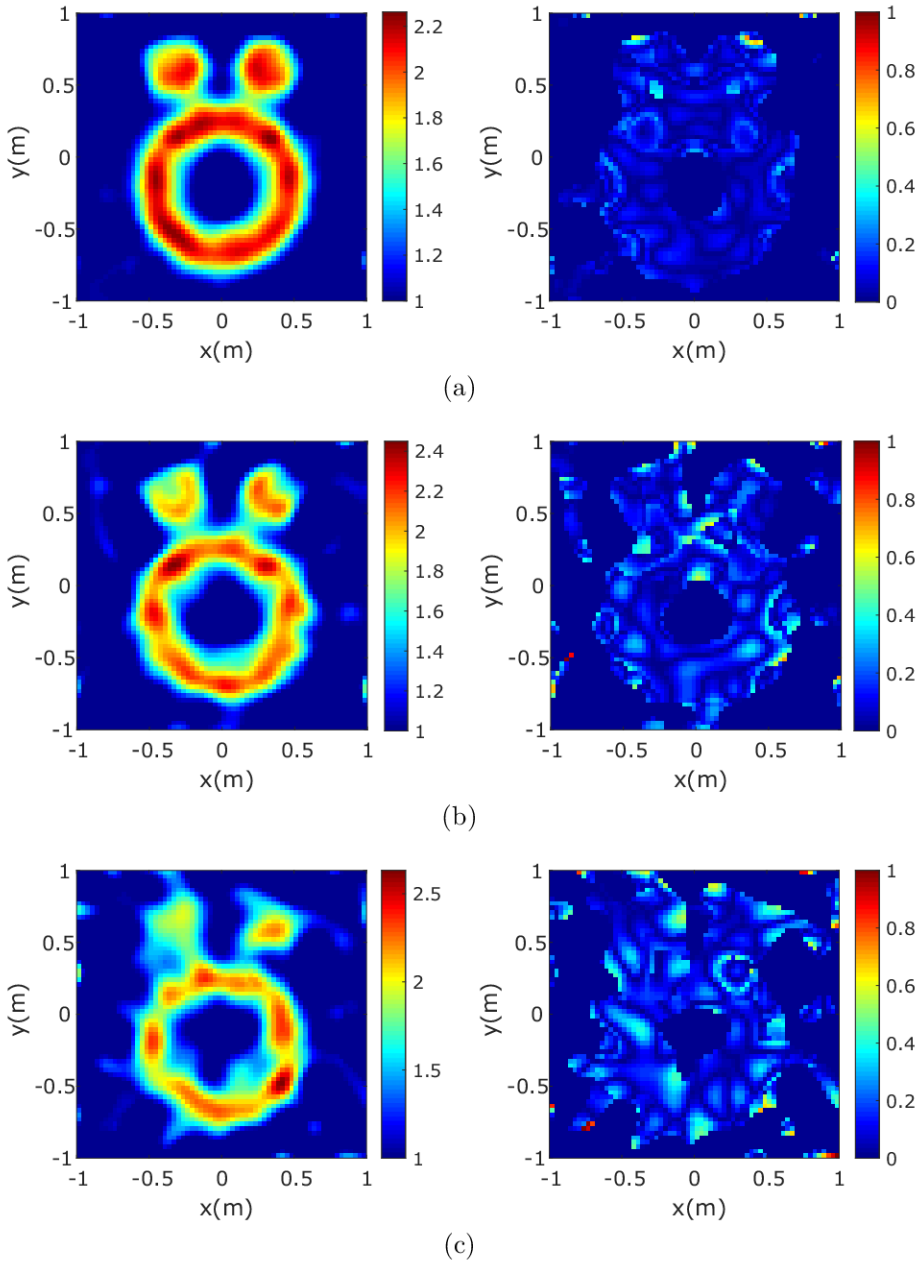

Figure 18 – Reconstruction results. Real part (left column) and negative imaginary part (right column) of the reconstructed relative permittivity profiles after 30 iterations with (a) 10%, (b) 30%, and (c) 50% AWGN.

For the three AWGN levels, the inversion results are obtained after 30 iterations. The real and imaginary parts of the images reconstruction are successful in the cases of 10% and 30% AWGN. The result in the case of 50% AWGN is also satisfactory, although

in the real part a distortion appears in the upper discs. We use the profile permittivity error, ERR_ε, as the quality criterion of the reconstructed images, which are shown in Figure 19. In terms of convergence, we depict the curve of the cost function for each noise level in Figure 20.

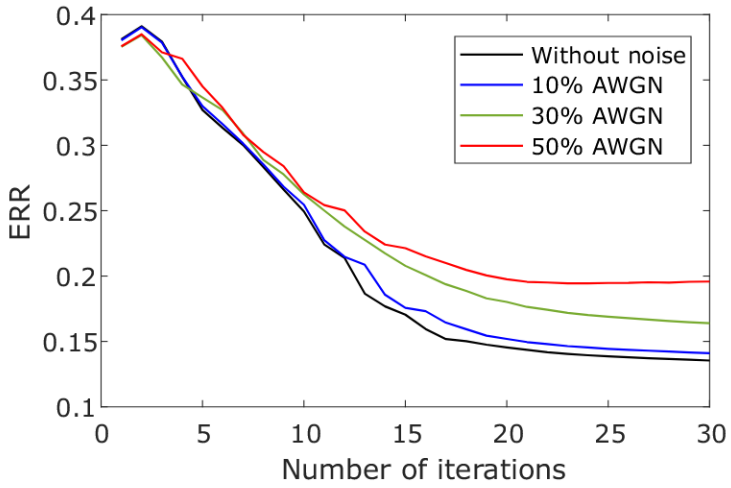

Figure 19 – Errors of the reconstructed permittivity profiles using synthetic data for noiseless, 10%, 30%, and 50% AWGN.

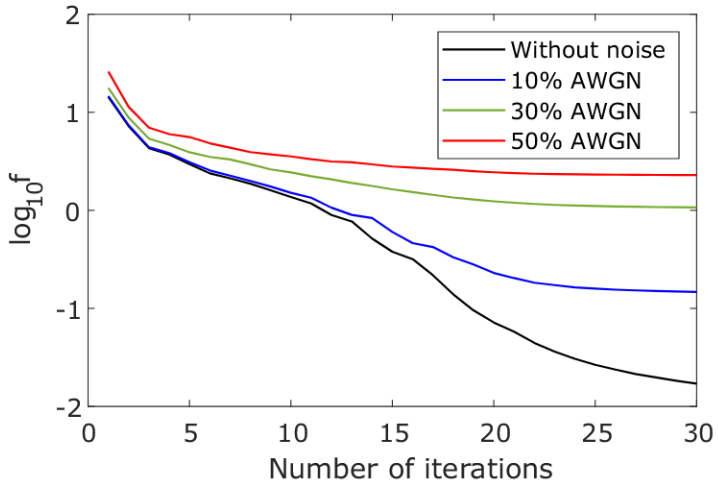

Figure 20 – Cost function as a function of the number of iterations for different noise levels.

Note that the error monotonically decreases and the reconstruction results show effectiveness in solving the inverse scattering problem with noise-corrupted data. The reconstruction errors, ERR_ε, for noiseless, 10%, 30%, and 50% AWGN are 0.1354, 0.1411, 0.1640, and 0.1958, respectively. In comparison, the rate of convergence of the original CGM and the efficient CGM is the same. Thus, the quality of the reconstructed profile of the original method is preserved.

As presented in subsection 3.4.1, the efficient CGM is found to share a computational complexity similar to the DBIM. Therefore, the convergence speed and accuracy of the

CGM are compared with the DBIM. The inversion results using efficient CGM and DBIM are depicted in Figures 21(b) and (c), respectively. The two reconstructions are very similar, which show an accurate reconstruction of the location, shape, and permittivity values of the scatterers. In this case, the null imaginary part of the reconstructed profile is omitted and the zero initial guess is used.

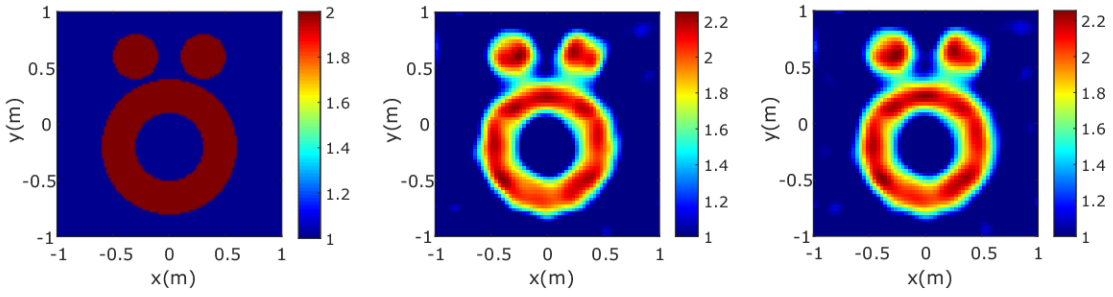

Figure 21 – Reconstruction results using synthetic data with 10% AWGN. (a) True profile. Reconstructed relative permittivity profile after 50 iterations. (b) Efficient CGM. (c) DBIM with $\gamma = 0.25$.

The profile permittivity errors are depicted in Figure 22. Different values of γ were empirically defined after successive experiments. A very small value of γ results in an unstable solution, for instance, $\gamma = 10^{-3}$, results in an unstable solution and DBIM fails to converge, while a very large value results in a slower convergence speed, see $\gamma = 0.50$ in Figure 22. There are some numerical techniques to estimate the value of the regularization parameter, such as the L-curve method (Hansen; O'Leary, 1993). Although an optimal value of the regularization parameter in the DBIM can be found by the L-curve method, this procedure will increase the computational effort. Besides, the performance of the CGM is independent of any regularization parameter in this case.

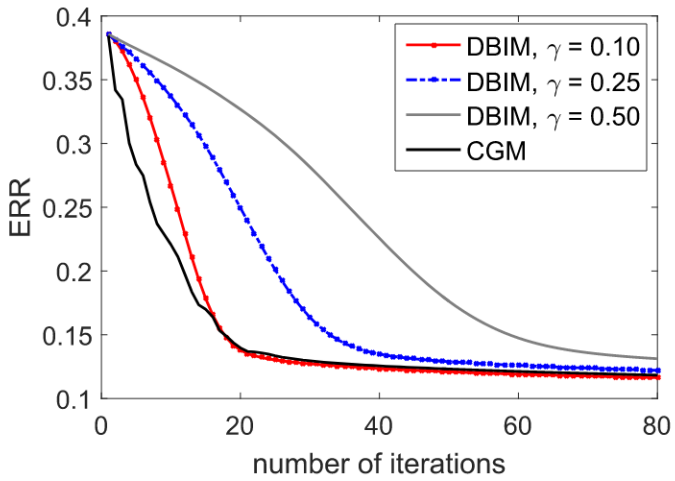

Figure 22 – Errors of the reconstructed permittivity profile for the "Austria" profile using efficient CGM and DBIM.

Finally, the computational cost and the solution accuracy for the previous numerical results are presented to demonstrate the reduction of computational time of the efficient CGM implementation. The CPU time and permittivity profile error are summarized in Table 1. Due to the high computational cost and storage requirement of the standard CGM, it is necessary to use a high-performance computer, since the original CGM would demand at least $N^2 \times 16$ Bytes to store the $\overline{\overline{\mathcal{L}}}_{(\chi)}$ dense matrix beyond the internal fields computed. Thus, the algorithms are executed on an intel Xeon E5-2640 v3, 2.6GHz with 128GB RAM.

Table 1 – CPU time after 50 iterations.

	Standard CGM	Efficient CGM	DBIM
CPU time (s)	4653.7	2531.8	2759.0
ERR_ε	0.1234	0.1230	0.1238

In addition, we compare the computational time as a function of the number of unknowns N by using the original nonlinearized CGM, the proposed CGM implementation with CG-FFT, and DBIM. Figure 23 shows the comparison of the CPU time for the three reconstruction algorithms, here the CPU time is obtained after 50 iterations.

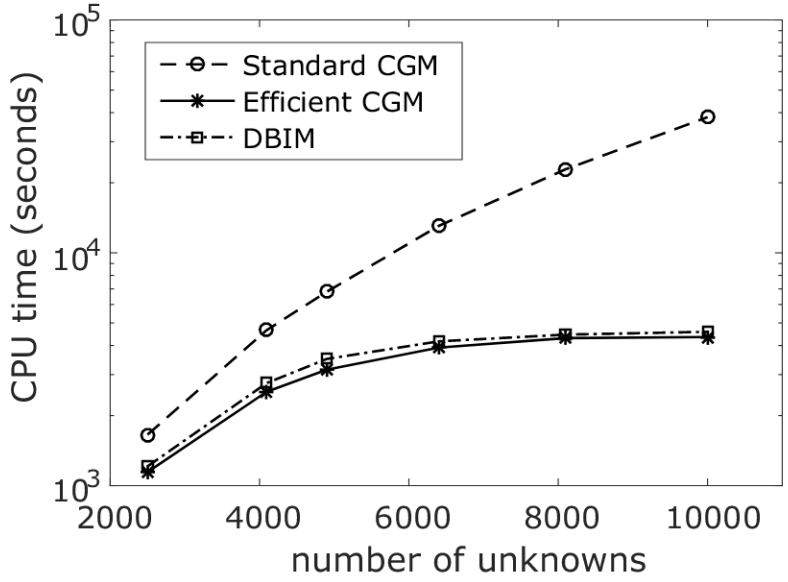

Figure 23 – Comparison of the computational time as a function of the number of unknowns for the reconstruction of the "Austria" profile using different inversion algorithms.

4.1.2 Convergence of S-CGM

This numerical experiment is devoted to demonstrating the performance of the subspace-based conjugate-gradient method (S-CGM). The well-known "Austria" profile with relative permittivity equal to 2.0 is considered. As in Ye and Chen (2017), the

scattered fields are collected for 30 receivers and 10 transmitters evenly located on a circle centered at the origin with radius 5 m. The operating frequency is 300 MHz. The measured scattered fields are obtained by solving the forward solver using MoM CG-FFT with a discretization of 100×100 cells, whereas for the inversion the discretization is 64×64 cells. The scattered data are corrupted with 10% additive white Gaussian noise (AWGN). In this case, a *priori* information about the problem is that the unknown contrast is nonnegative (Van den Berg; Kleinman, 1997) and the initial guess is obtained from the back-propagation method.

Since the proposed S-CGM is based on a linearized CGM approach and its implementation requires the forward-solver, the S-CGM is mainly compared with the linearized CGM. It is important to note that the linearized CGM can be understood as a special case of the S-CGM when $L = 0$. In the results, we refer to it as S-CGM with $L = 0$. The convergence curves of the cost function and the profile permittivity error for different values of L are shown in Figures 24(a) and (b), respectively.

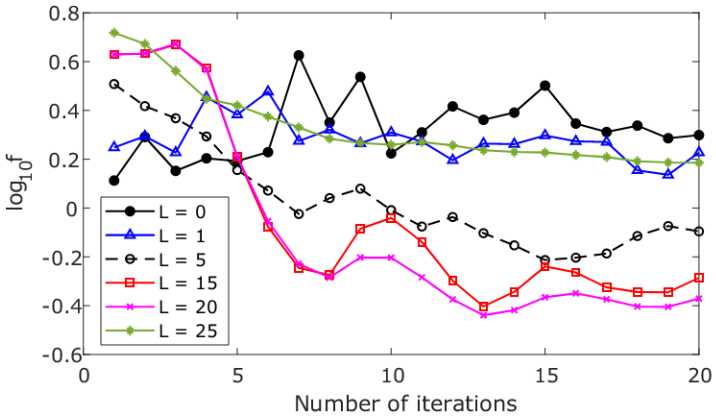

(a)

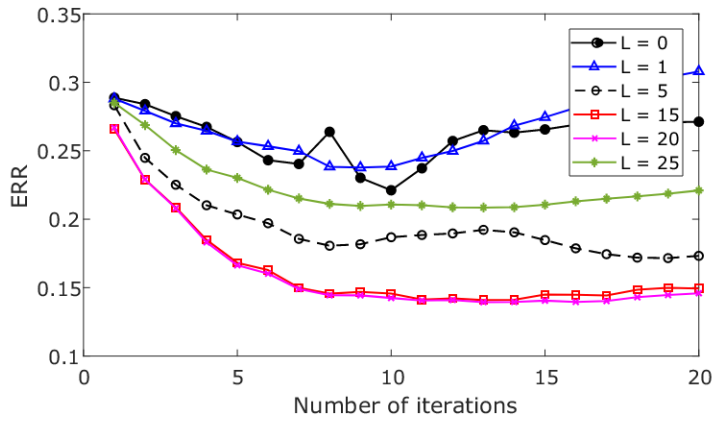

(b)

Figure 24 – Convergence curves in the first 20 iterations for S-CGM with different values of L. (a) Cost function values. (b) Error of the reconstructed permittivity profile as a function of the number of iterations.

The reconstructed profiles are shown in Figure 25. In this case, the null imaginary part of the reconstructed profile is omitted.

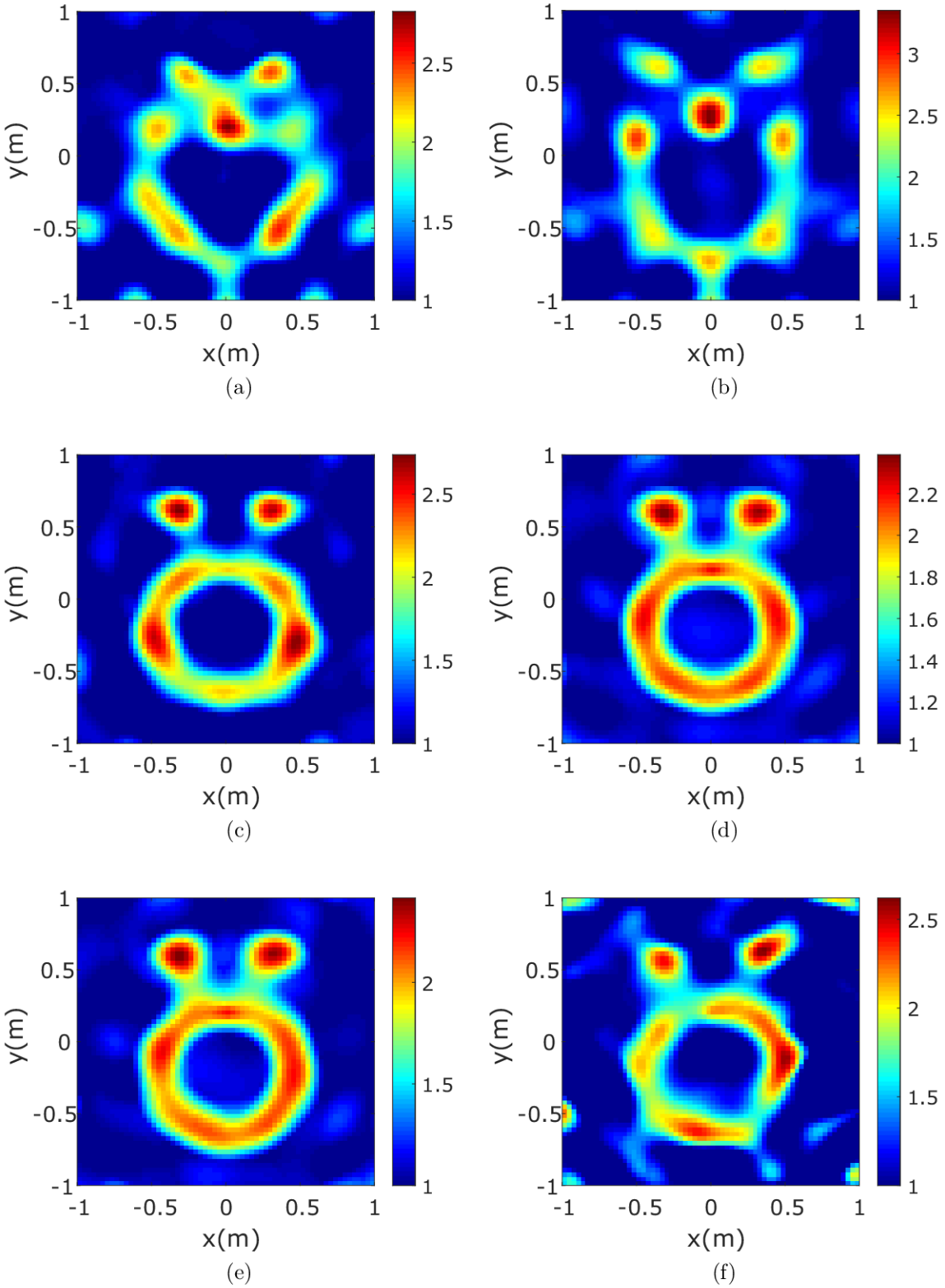

Figure 25 – Reconstruction results using synthetic data with 10% AWGN. Reconstructed relative permittivity using S-CGM with (a) $L = 0$. (b) $L = 1$. (c) $L = 5$. (d) $L = 15$. (e) $L = 20$. (f) $L = 25$.

From Figure 24, we observe that the S-CGM reaches a higher speed convergence and accuracy that the linearized CGM ($L = 0$). It is also demonstrated that for small values of L the S-CGM approximates the linearized CGM (limit case S-CGM with $L = 0$). However, the value of L cannot be very large because the calculation of the variational induced current $\delta\overline{J}^d$ is inaccuracy, due to the deterministic current is contaminated by the noise. In this problem, different integer values of L result in a satisfactory solution. In the S-CGM, the regularization parameter L is not a sensitive issue and it can be easily chosen from a wide range of consecutive integer values. Figure 26 shows the spectrum of the radiation operator matrix $\overline{\overline{G}}_s$. A good choice of the value of L is to take the value where singular values noticeably change the slope in the spectrum (Chen, 2010), for instance, $L = 15$ in Figure 26.

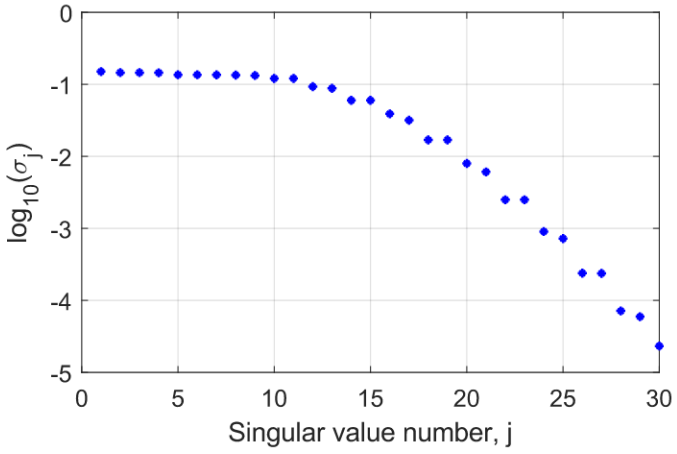

Figure 26 – Spectrum of the radiation operator matrix $\overline{\overline{G}}_s$.

In order to analyze the robustness of S-CGM against noise in the scattered data, the reconstructed profiles for 30% and 50% noise are presented in Figure 27.

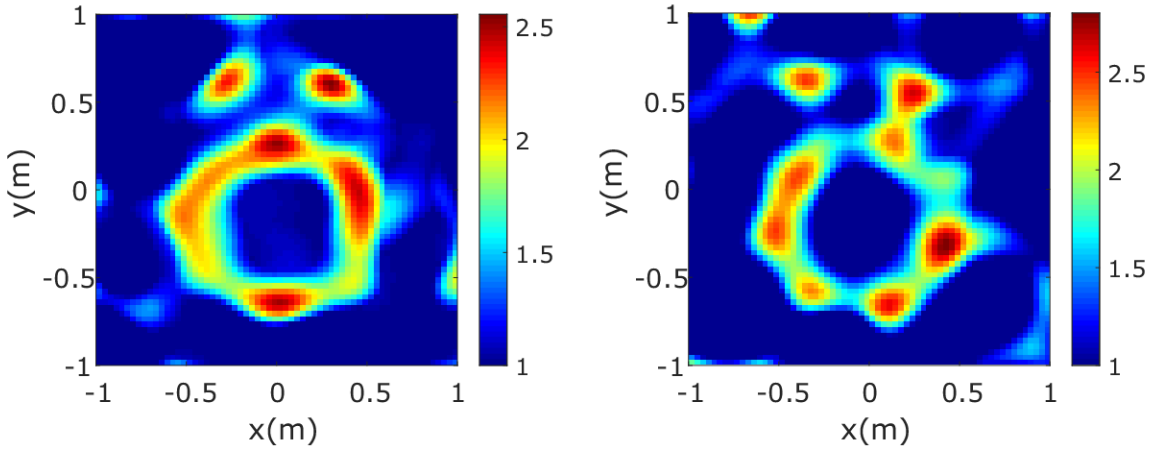

Figure 27 – Reconstruction results with $L = 15$. Reconstructed relative permittivity profile after 20 iterations. (a) 30% noise. (b) 50% noise.

The reconstructed profile with 10% noise is successful, as shown in Figure 25(d). However, the result for 30% noise exhibits a distortion in the ring. Despite this, the location and relative permittivity of the scatterers are correctly reconstructed. In the case of 50% noise, some artifacts appear in the scatterers and the image quality is not satisfactory.

4.1.3 Convergence of fast CGM

In order to show the range of applicability of the fast CGM, different contrast values have been considered. In particular, the range of the approximation in the fast CGM is determined by $\|G_D\chi\| \leq 1$. Figure 28 shows the plot of the operator $\|G_D\chi\|$ for different contrast values of the "Austria" profile, the configuration is as in the previous subsection. In addition, we analyze the norm of this operator by considering a square domain with side D_x and the matrix norm is shown in Figure 29. As can be observed, the norms increase monotonically as a function of the electrical size of the domain and it is also notable that norm increases according to the factor χ.

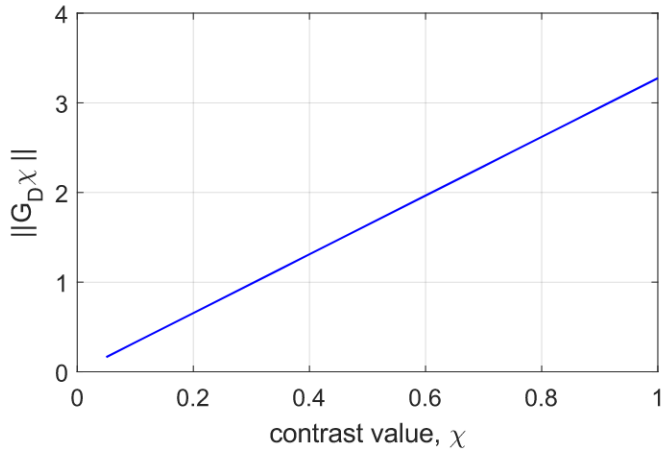

Figure 28 – Matrix norm as a function of the contrast value.

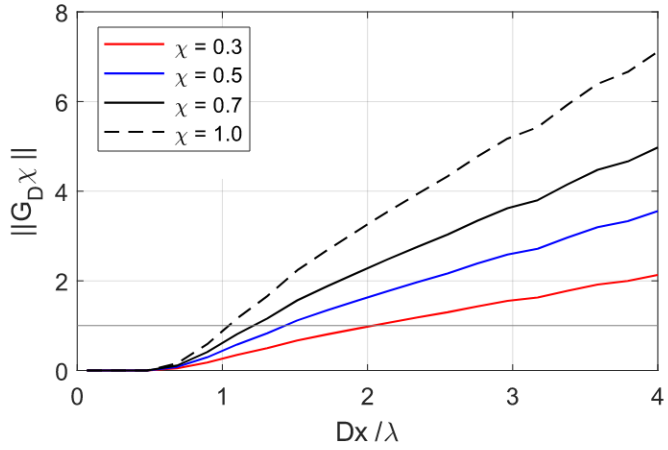

Figure 29 – Matrix norm as a function of the electrical size of the domain for different contrast values.

For this numerical test, the configuration problem is as in the previous subsection. Firstly, we consider the "Austria" profile with contrast values of $\chi = 0.3$, $\chi = 0.5$, $\chi = 0.7$, and $\chi = 1$. The background medium is air, i.e., the contrast value $\chi = 1$ represents the profile when the relative permittivity of the scatterers is $\varepsilon_r = 2$. The operating frequency is 300 MHz. The reconstructed permittivity profiles are depicted in Figure 30.

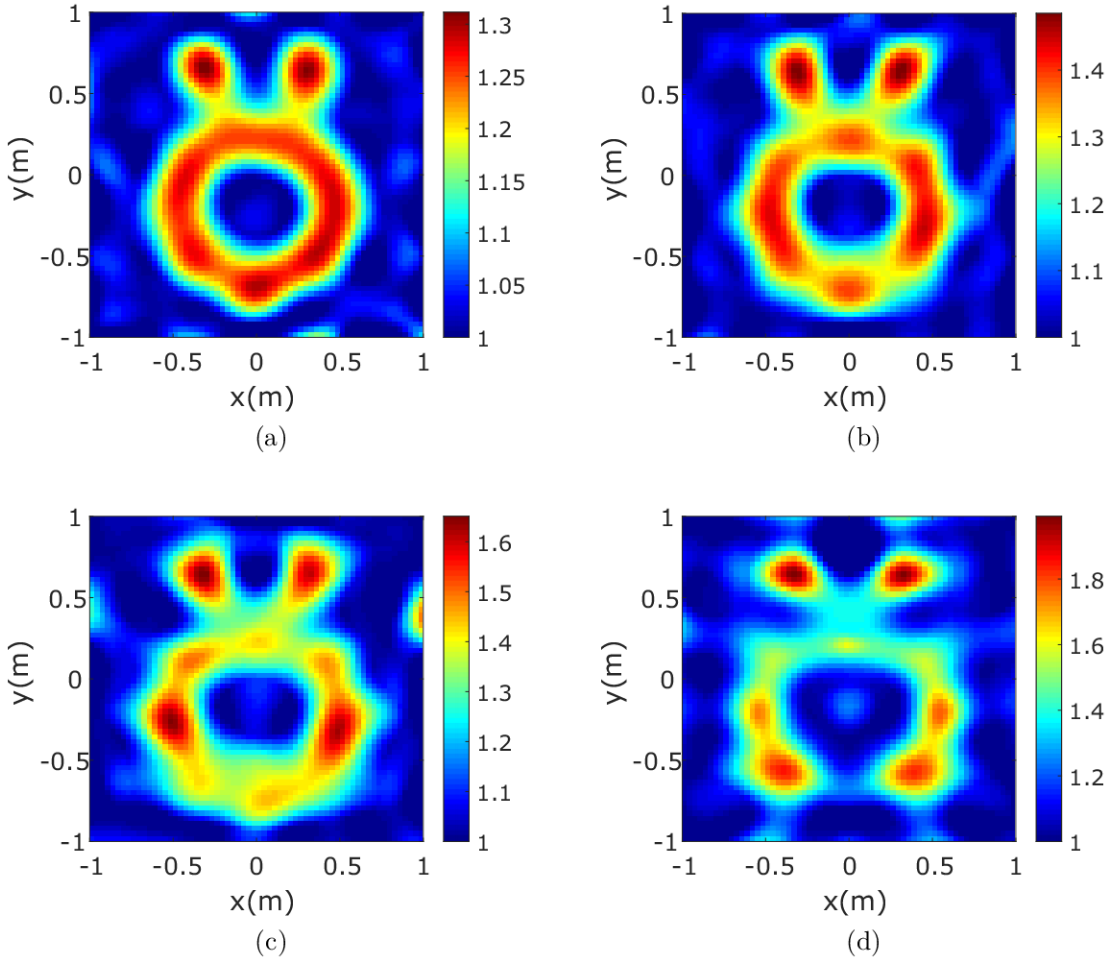

Figure 30 – Reconstruction results using fast CGM. Reconstructed relative permittivity profile after 20 iterations. (a) $\chi = 0.3$. (b) $\chi = 0.5$. (c) $\chi = 0.7$. (d) $\chi = 1$.

As expected, the fast CGM fails to reconstruct problems with high nonlinearity. However, this fast CGM approach can be interesting in linear frameworks. The permittivity profile errors in Figure 30(a)-(d) are 0.0614, 0.1094, 0.1696, and 0.2595, respectively. In comparison, the convergence curves for the four different contrast values are shown in Figure 31.

In order to prove the convergence as a function of the electrical size of the domain of interest, we set the contrast value to 0.5, i.e., the relative permittivity of the "Austria" profile equal to 1.5. Then, different relative domain sizes D_x/λ are used, specifically, D_x is held constant and equal to 2 m, while four different incident operating frequencies are used. The respective background wavelengths are are 1.2 m, 1 m, 0.8571 m, and 0.75 m.

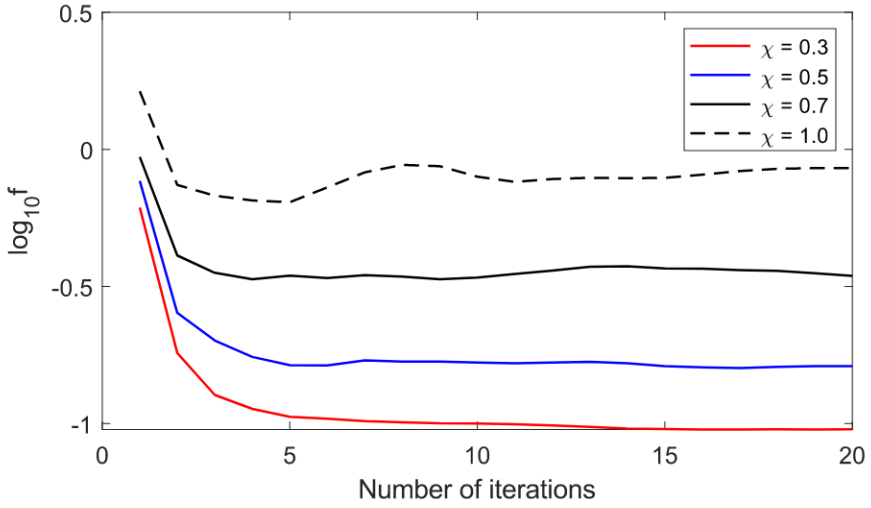

Figure 31 – Convergence curves for different contrast values.

The reconstruction results are presented in Figure 32. The permittivity profile errors in Figure 32(a)-(d) are 0.1074, 0.1094, 0.1096, and 0.1135, respectively.

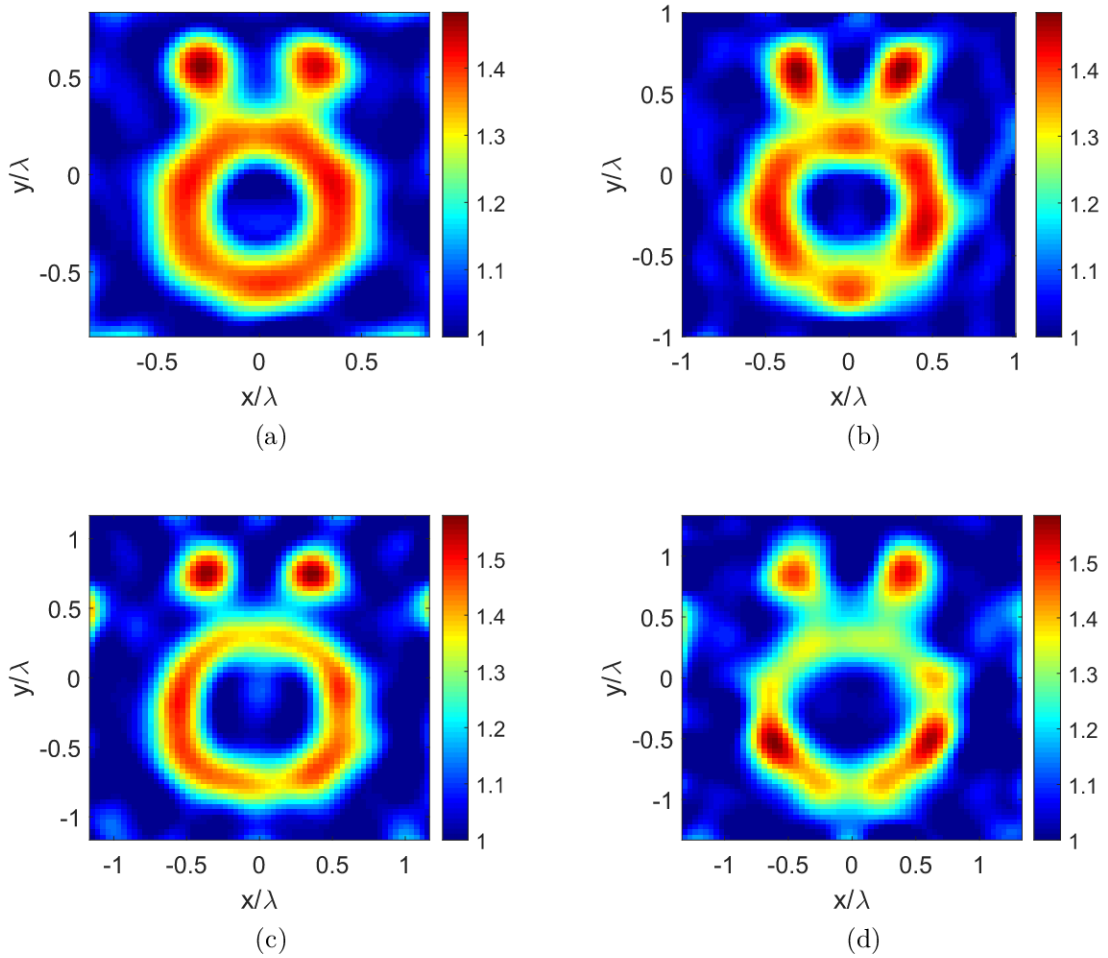

Figure 32 – Reconstruction results with $\chi = 0.5$ using fast CGM. Reconstructed relative permittivity profile after 20 iterations. (a) $D_x/\lambda = 1.67$. (b) $D_x/\lambda = 2$. (c) $D_x/\lambda = 2.33$. (d) $D_x/\lambda = 2.67$.

The cost function value during the iterative inversion procedure is shown in Figure 33. We observe that the accuracy of the reconstruction improves as the electrical domain size becomes smaller. Therefore, the inverse matrix approximation to solve the forward problems in fast CGM is more suitable for reconstructing scatterers rather smaller than the wavelength.

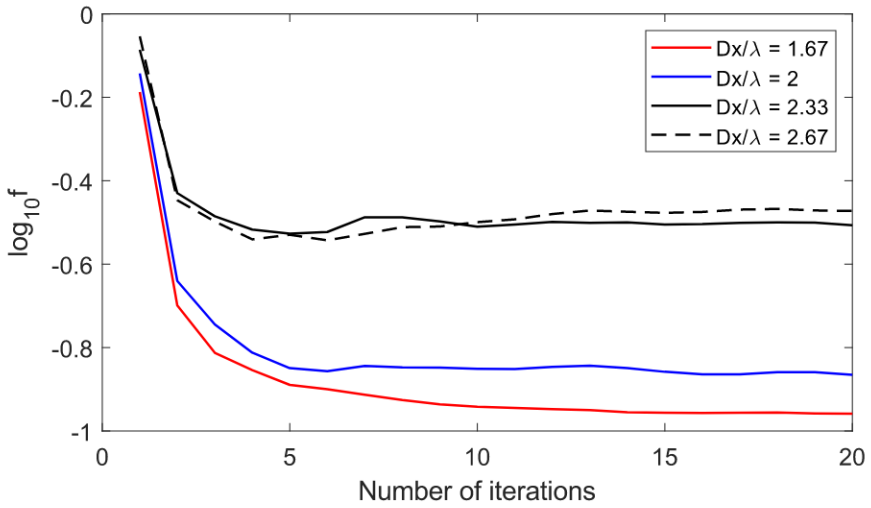

Figure 33 – Convergence curves for different domain sizes.

4.1.4 Comparison of the four methods

This numerical experiment aims to compare the different methods: nonlinearized CGM, linearized CGM, S-CGM, and fast CGM. We carry out reconstructions with both a linear and nonlinear framework. In the first case, the relative permittivity of the "Austria" profile equal to 1.5 (weak scatterer) is considered. In the second one, the relative permittivity is $\varepsilon_r = 2$, which presents more difficulty and has a higher degree of nonlinearity.

The reconstructed profiles for the "Austria" problem with $\varepsilon_r = 1.5$ are presented in Figure 34. We observe that the reconstruction results for the true relative permittivity of ε_r= 1.5 are satisfactory, e.g., location, shape, and permittivity values of the scatterers. The results are obtained from the initial guesses with back-propagation method and a 64×64 mesh grid is used. In order to evaluate the speed of convergence and quality of the results, the cost function and the permittivity profile error, ERR_ε, for the four permittivity profiles are presented in Figure 35 and Figure 36, respectively. As can be seen, the nonlinearized CGM (efficient CGM) and the S-CGM show better performance than linearized CGM and fast CGM. The fast CGM approach presents greater error in the solution due to the precision of the forward solver, which is valid when $\|G_D\chi\| \leq 1$, as discussed in subsection 4.1.3. However, this fast method is less time-consuming because it does not solve the full-forward problem. In addition, we try to increase the number of iterations, but the accuracy solution does not improve.

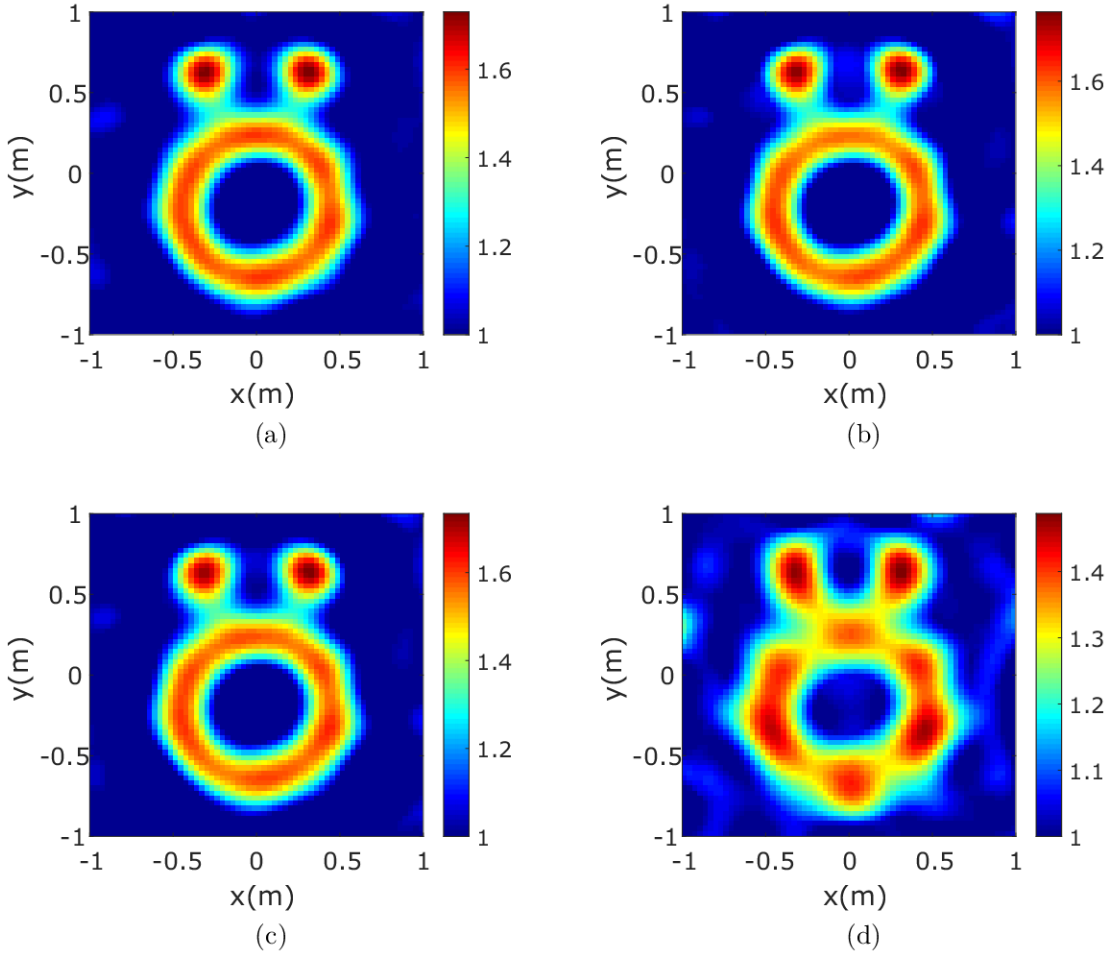

Figure 34 – Reconstruction results for the "Austria" profile with $\varepsilon_r = 1.5$ after 20 iterations. (a) Nonlinearized CGM. (b) Linearized CGM. (c) S-CGM with L = 15. (d) Fast CGM.

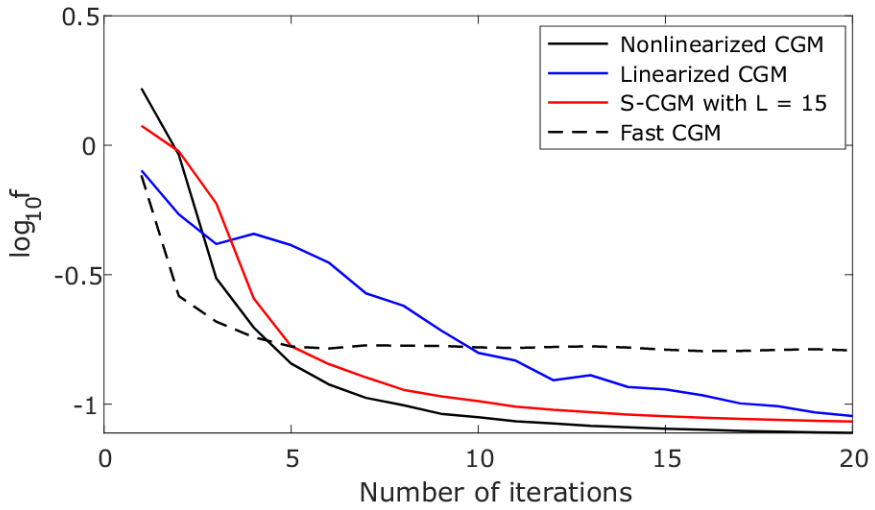

Figure 35 – Convergence curves using different inversion methods for the "Austria" profile with $\varepsilon_r = 1.5$.

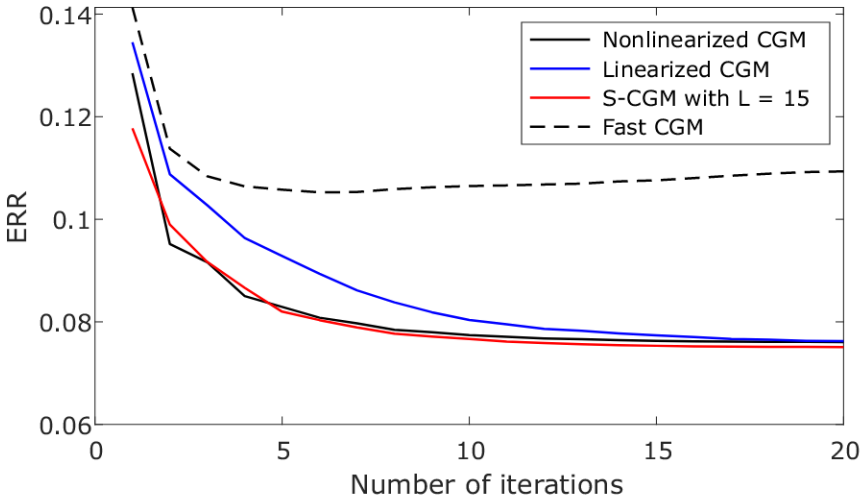

Figure 36 – Permittivity profile error using different inversion methods for the "Austria" profile with $\varepsilon_r = 1.5$.

The CPU time and the permittivity profile error for the four inversion methods are summarized in Table 2. The CPU used is AMD Ryzen 5 2400G@3.6GHz with Radeon Vega Graphics. The nonlinearized CGM takes a longer time in each iteration because it solves the nonlinear problem and the forward solvers are computationally more expensive, whereas the linearized approach and the fast CGM reduce the calculations at each iteration step by approximating the gradient computation. Besides, the S-CGM shows a solution accuracy similar to that of the nonlinearized CGM and has a short calculation time.

Table 2 – CPU time per iteration using four different methods for the "Austria" profile with $\varepsilon_r = 1.5$.

Method	CPU time(s)/iteration	ERR_ε
Nonlinearized CGM	13.77	0.0761
Linearized CGM	4.78	0.0762
S-CGM	5.18	0.0751
Fast CGM	0.97	0.1093

Secondly, we consider the "Austria" problem with $\varepsilon_r = 2$. The reconstruction of the relative permittivity profiles for the four different inversion approaches is shown in Figure 37. It is verified that this problem presents more difficulty (strong scatterers) and nonlinearity. As a result, the linearized CGM and fast CGM fail to recover the "Austria" problem when $\varepsilon_r = 2$, see Figures 37(b) and (d). Whereas the nonlinearized CGM and the S-CGM can handle this complexity, as shown in Figures 37(a) and (c), respectively. The convergence curves are presented in Figure 38. As in the previous test, the nonlinearized CGM presents faster convergence and stability in the solution. However, the S-CGM also has a good performance. The permittivity profile errors for the four inversion methods are depicted in Figure 39. We observe that the error curves in the nonlinearized CGM and S-CGM are very close.

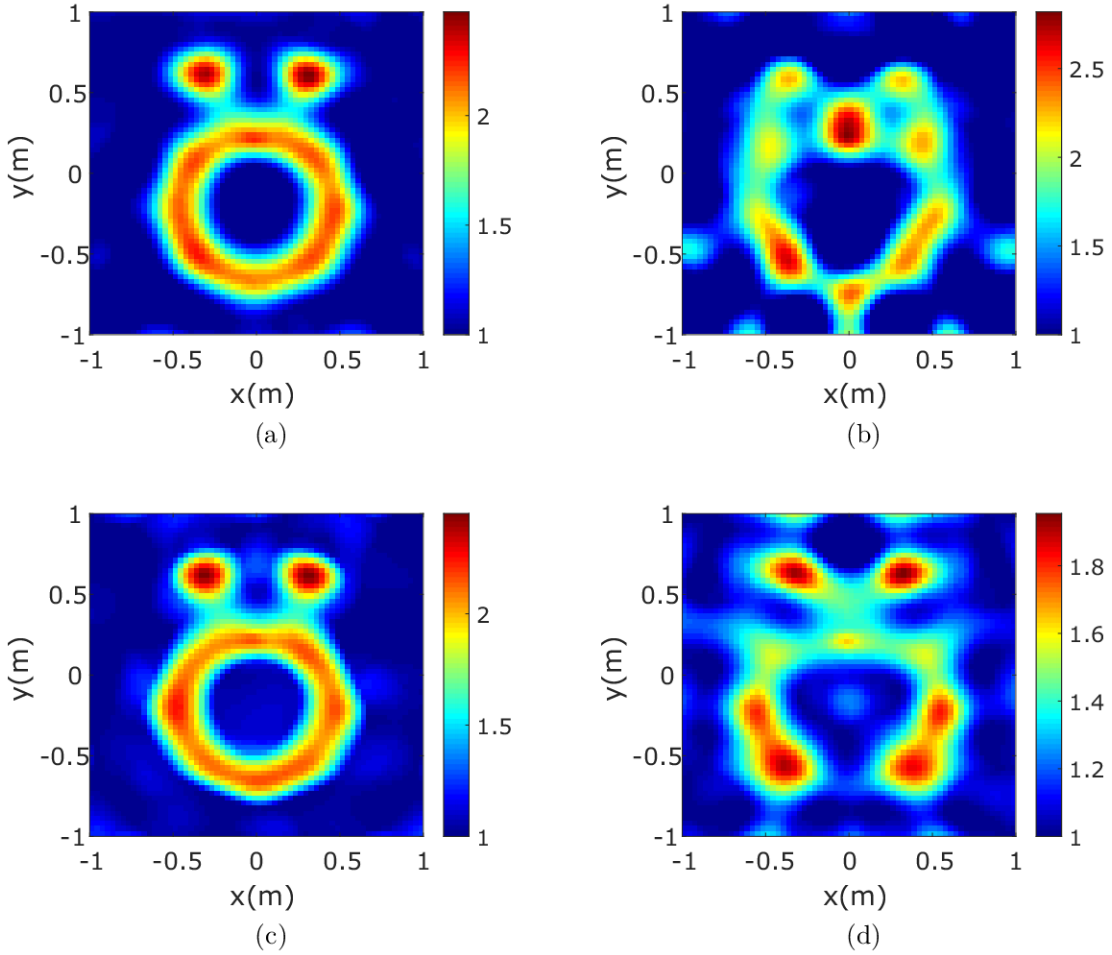

Figure 37 – Reconstruction results for the "Austria" profile with $\varepsilon_r = 2$ after 20 iterations. (a) Nonlinearized CGM. (b) Linearized CGM. (c) S-CGM with L = 15. (d) Fast CGM.

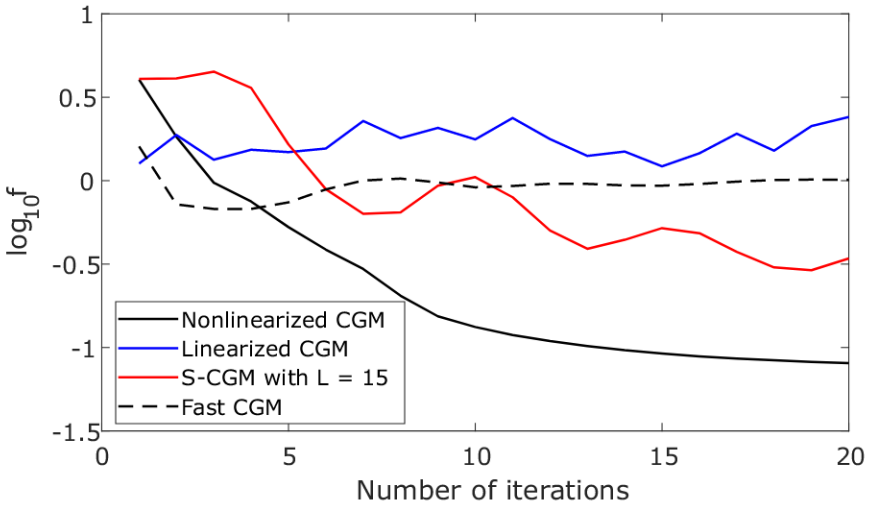

Figure 38 – Convergence curves using different inversion methods for the "Austria" profile with $\varepsilon_r = 2$.

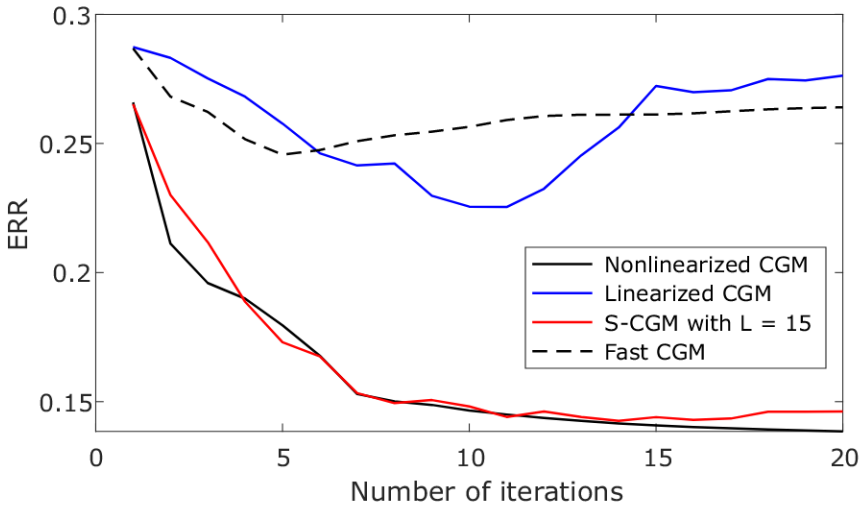

Figure 39 – Permittivity profile error using different inversion methods for the "Austria" profile with $\varepsilon_r = 2$.

Table 3 presents the CPU time per iteration for the reconstruction profiles in Figure 37. As mentioned above, the nonlinearized and the S-CGM present a good performance and success in the reconstruction of the "Austria" profile with $\varepsilon_r = 2$.

Table 3 – CPU time per iteration using four different methods for the "Austria" profile with $\varepsilon_r = 2$.

Method	CPU time(s)/iteration	ERR_ε
Nonlinearized CGM	26.83	0.1385
Linearized CGM	21.54	0.2762
S-CGM	9.98	0.1462
Fast CGM	0.76	0.2640

Finally, comparisons regarding the gradient approach, convergence speed, CPU time per iteration, and performance in the reconstruction of strong scatterers for the four methods are presented in Table 4. Each of the inversion methods based on the conjugate gradient has its advantages and disadvantages. In this sense, it is important to carefully choose the appropriate method depending on the demand of the inverse scattering problem, e.g., the contrast between the scatterers and the background medium, electrical size of the scatterers, quality of the recovered image, and execution time.

Table 4 – Comparison of the four inversion methods.

Method	Gradient approach	Convergence speed	CPU time second/iteration	Performance in strong scatterers
CGM	Nonlinear	Fast	Longest	Good
CGM	Linear	Medium	Medium	Bad
S-CGM	Linear	Medium	Medium	Average
Fast CGM	Nonlinear	Fast	Shortest	Bad

4.2 Test with synthetic data: different targets

In this numerical experiment, we consider different targets in order to explore the ability of the four methods of recovering scatterers with different shapes and materials. The simulated targets consist of a single kite, two circles, a coated cylinder within a square ring, and a set of multiple objects in the free-space background.

The measurement configuration is as follows: the synthetic scattered data are collected for 24 receivers and 12 transmitters evenly located on a circle centered at the origin with a radius of 5 m. The operating frequency is 300 MHz (wavelength $\lambda = 1$ m). We use 100×100 grid mesh to generate the synthetic scattered fields, while a 60×60 grid mesh is used in the inversion procedures and the scattered data are contaminated with 10% AWGN.

Firstly, the geometry of the kite target is as in Bevacqua and Isernia (2021). The domain of interest D is a square 1 m length. The kite shape is parameterized by $t \in [0, 2\pi]$ as follows

$$f(t) = [a\cos t + b\cos 2t - d, c\sin t], \tag{4.2}$$

where $a = 0.2750$, $b = 0.1788$, $c = 0.4125$, and $d = 0.0788$. The relative permittivity is 2. The second target consists of two circles of radius 0.2 m with relative permittivity equal to 2 centered at (0.215, 0) m and (-0.215, 0) m. In the third one, the domain of interest D is a square 2 m length. This contains a square ring with $\varepsilon_r = 1.3$, which has an exterior diameter of 1.8 m and an inner diameter of 1.7 m and is centered at the origin. A coated cylinder is located inside the square ring and is also centered at the origin. The inner cylinder has a radius of 0.2 m and the exterior radius is 0.5 m. The relative permittivity of the inner cylinder is 2, while the exterior one is 1.5. Lastly, the multiple objects consist of: a circle of radius 0.35 m, a square with a side length of 0.6 m, and a right triangle located in different positions with relative permittivities of 1.5, 2, and 1.8, respectively. The ground truth profiles are depicted in Figure 40.

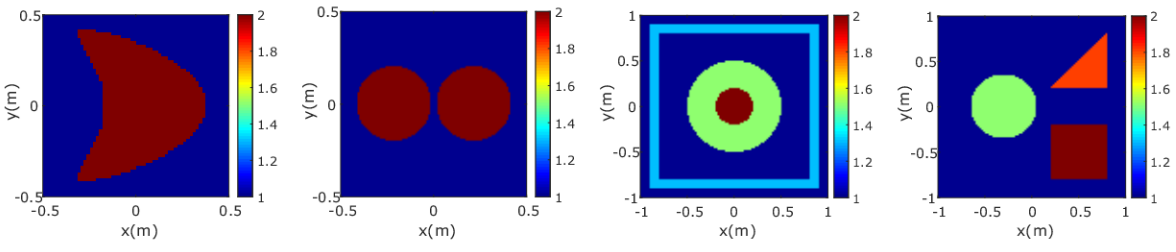

Figure 40 – Ground truth profiles. (a) kite. (b) two circles. (c) coated cylinder. (d) multiple objects.

The reconstruction results for the different targets using the nonlinearized CGM, linearized CGM, S-CGM, and fast CGM are presented in Figure 41(a)-(d), respectively. The reconstructed profiles are obtained from the back-propagation solution. In the S-CGM, the regularization term L was set to 10 for the reconstruction of all targets.

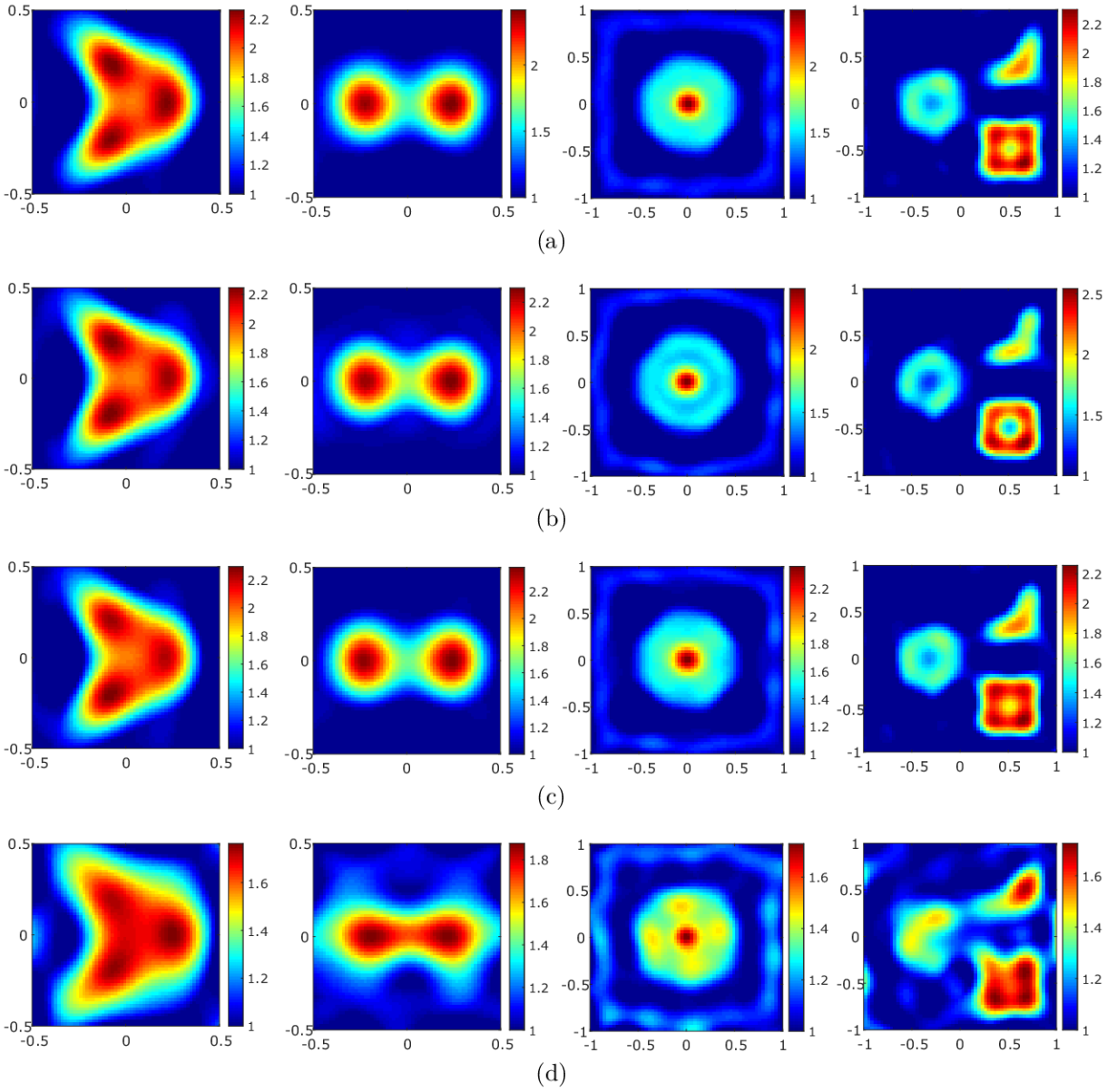

Figure 41 – Reconstructed relative permittivity profile of different targets using four inversion methods. (a) Nonlinearized CGM. (b) Linearized CGM. (c) S-CGM with $L = 10$. (d) Fast CGM.

Table 5 shows the profile permittivity error for the four inversion methods after 20 iterations. In comparison, the final error obtained by the nonlinearized CGM and the S-CGM is almost the same. On the other hand, the linearized CGM and the fast CGM present greater error in reconstruction, especially in the last two targets, which include multiple materials. Therefore, the nonlinearized CGM and the S-CGM provides higher quality in the reconstructed image than the linearized and the fast CGM approaches.

Table 5 – Permittivity profile error of numerical experiments.

Target	ERR_ε			
	Nonlinearized CGM	Linearized CGM	S-CGM	Fast CGM
Kite	0.1378	0.1390	0.1376	0.2068
Two circles	0.1539	0.1536	0.1490	0.2024
Coated cylinder	0.0859	0.1035	0.0921	0.1228
Multiple objects	0.0997	0.1093	0.0960	0.1664

Finally, the CPU time per iteration for the reconstruction of each target is listed in Table 6.

Table 6 – CPU time per iteration of numerical experiments.

Target	Second/iteration			
	Nonlinearized CGM	Linearized CGM	S-CGM	Fast CGM
Kite	6.53	2.84	3.16	0.50
Two circles	5.30	2.54	2.81	0.51
Coated cylinder	9.59	4.51	4.06	0.51
Multiple objects	11.71	5.85	5.43	0.55

4.3 Test with experimental data

This experiment aims to validate the inversion algorithms against experimental data from the Institut Fresnel database (Geffrin; Sabouroux; Eyraud, 2005). All targets are elongated objects, which have no variation in the z-direction, and measured data with TM polarization are used. The *FoamDielInt* target consists of one smaller cylinder with $\varepsilon_r = 3$, which is embedded in a larger cylinder with $\varepsilon_r = 1.45$, see Figure 42(a). In the *FoamTwinDiel* target, one smaller cylinder is added, as shown in Figure 42(b). The smaller cylinders have a radius of 3.1 cm and the radius of the larger cylinder is 8 cm. The measured data were collected for 241 receivers and 9 frequencies from 2 to 10 GHz. The *FoamDielInt* and *FoamTwinDiel* targets are illuminated by 8 and 18 transmitters, respectively. In the experimental setup performed by the Institut Fresnel, the receiving aperture is from 60° to 300°, that is, only 2/3 of a full aperture is used. To calibrate the scattered data, the procedure outlined in Geffrin, Sabouroux and Eyraud (2005) is adopted, where the transmitting antennas are approximated by electric line sources and a single calibration factor per transmitter is used. This calibration factor is derived from the ratio of the simulated incident field and the measured one at the receiver located opposite the transmitter (incidence angle of 180°). The distance from the receivers to the center of the target is 1.67 m. For each incidence, we use 72 receiving points out of 241 receivers, which are evenly distributed around the target. However, for each illumination angle, the field is measured for only 49 of the 72 receiver angles due to the physical limitations of the receiving aperture, and the field at the remaining receiving points is set to zero.

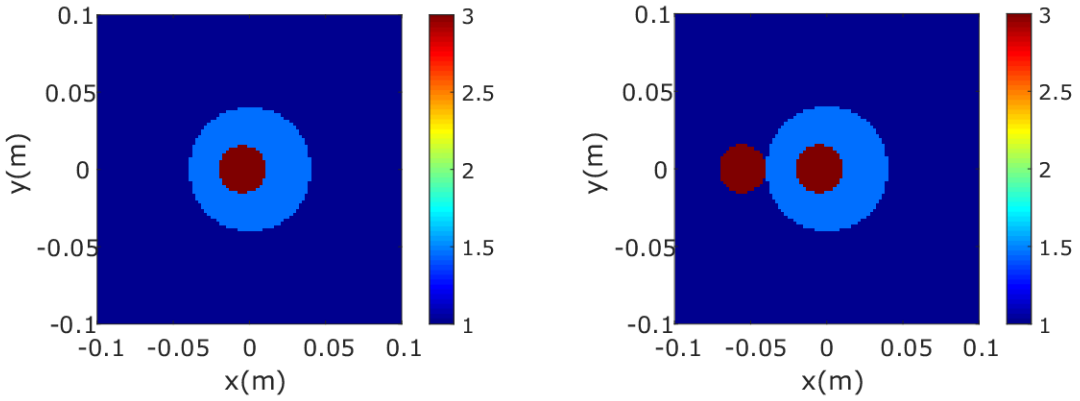

(a) (b)

Figure 42 – Experimental targets. (a) *FoamDielInt*. (b) *FoamTwinDiel*.

In the *FoamDielInt* target, the reconstruction is carried out in a single frequency of 4 GHz, whereas in *FoamTwinDiel*, a frequency of 3 GHz is used. The reconstruction results are obtained from zero initial guesses and a 64×64 grid mesh is used. The results for the *FoamDielInt* using different inversion methods are shown in Figure 43.

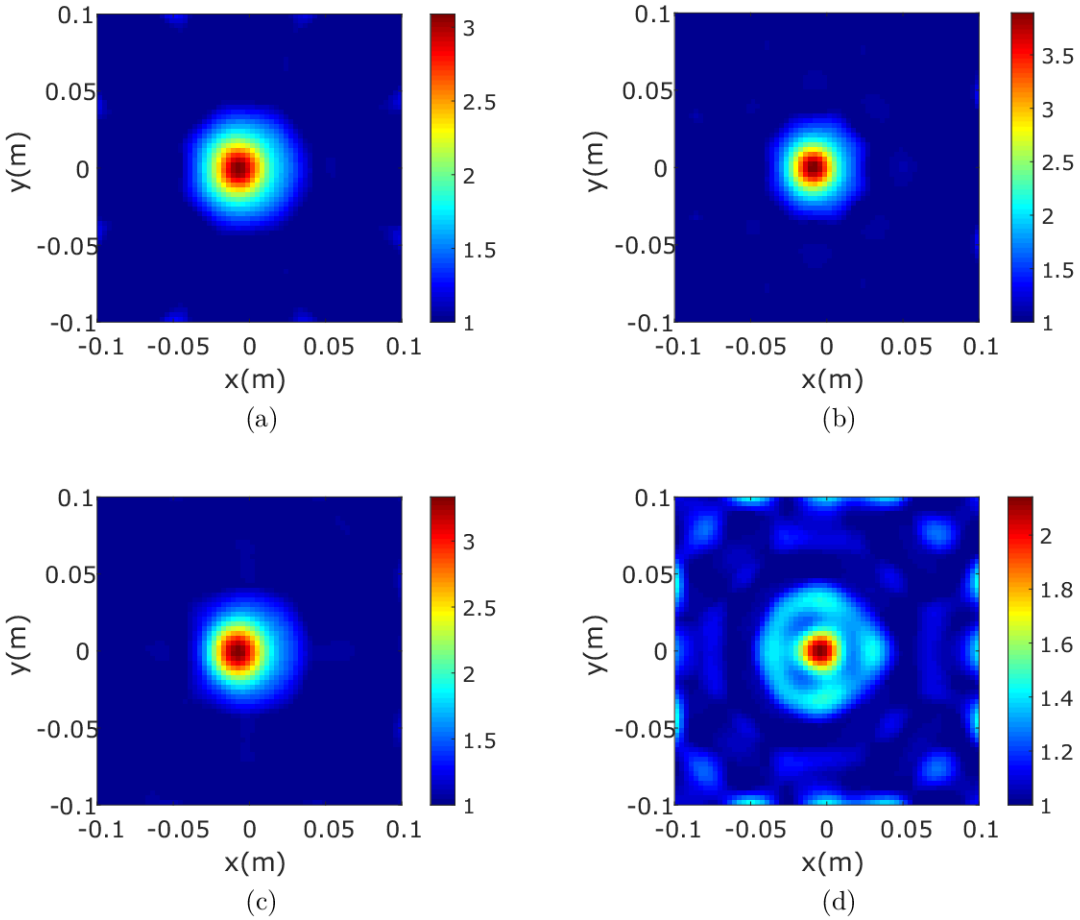

(a) (b)

(c) (d)

Figure 43 – Reconstruction results at 4 GHz of the *FoamDielInt* target. (a) Nonlinearized CGM. (b) Linearized CGM. (c) S-CGM with $L = 10$. (d) Fast CGM.

In the same way, the reconstruction results for the *FoamTwinDiel* are shown in Figure 44(a)-(d). As the scatterers are lossless dielectrics, the null imaginary part of the profile is omitted in both targets.

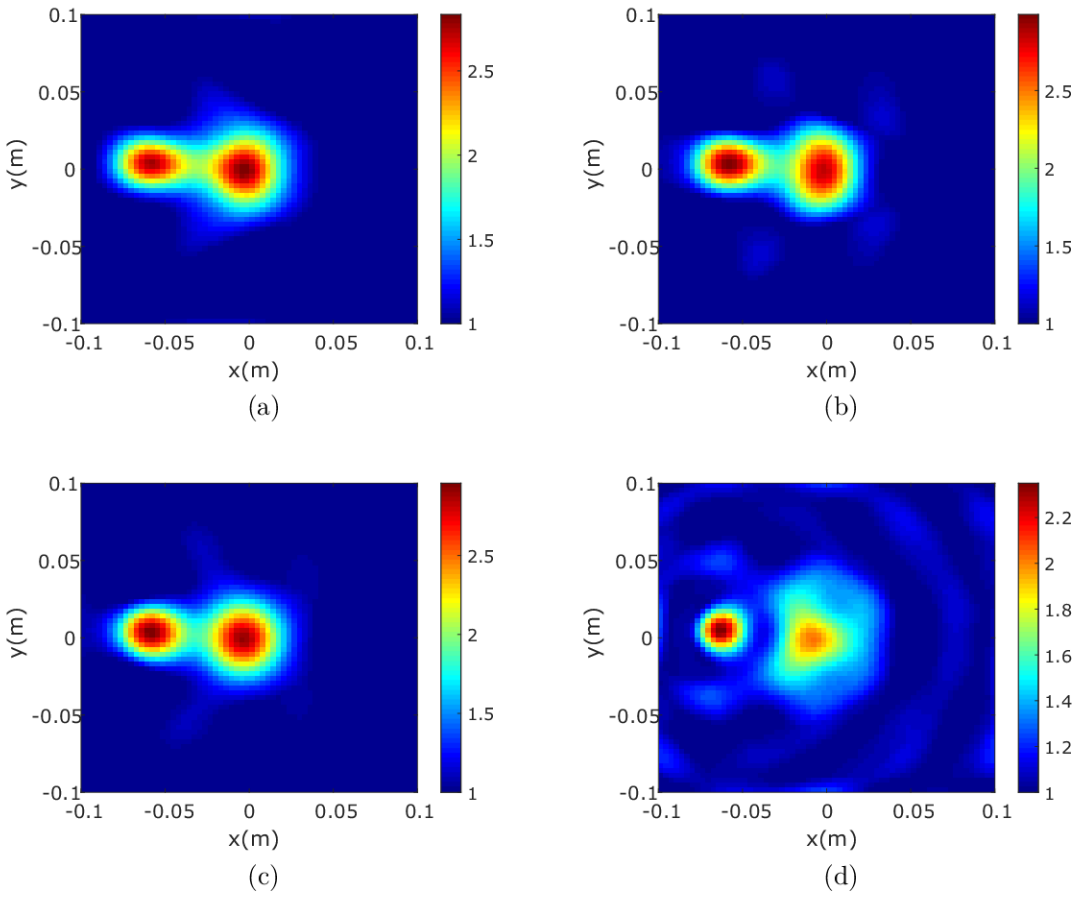

Figure 44 – Reconstruction results at 3 GHz of the *FoamTwinDiel* target. (a) Nonlinearized CGM. (b) Linearized CGM. (c) S-CGM with $L = 10$. (d) Fast CGM.

The permittivity profile error, ERR_ε, and the number of iterations of the reconstructed profiles at single-frequency data set shown in Figure 43 and Figure 44 are listed in Table 7.

Table 7 – Error quantification with experimental data using single-frequency inversion

Method	*FoamDielInt*		*FoamTwinDiel*	
	iterations	ERR_ε	iterations	ERR_ε
Nonlinearized CGM	30	0.1092	25	0.1736
Linearized CGM	40	0.1309	50	0.1753
S-CGM	20	0.1049	25	0.1653
Fast CGM	30	0.1871	24	0.2295

In addition, the four inversion methods were tested against all the experimental data using 9 different frequencies from 2 to 10 GHz with a step of 1 GHz. However, the reconstruction results are not successful at the highest frequencies. In fact, most

inversion methods fail to reconstruct the experimental data from the Institut Fresnel with higher frequency data (without using frequency-hopping or multiple-frequency approaches) (Xu; Zhong; Wang, 2018). In order to improve the reconstruction profiles, a frequency-hopping procedure can be used (Chew; Lin, 1995). At each frequency, the initial solution is obtained from the reconstruction result of the preceding frequency. In this case, we consider 5 frequencies from 2 to 6 GHz with 1 GHz step and 3 iterations per frequency. The reconstruction results for the *FoamDielInt* target using frequency-hopping technique are presented in Figure 45.

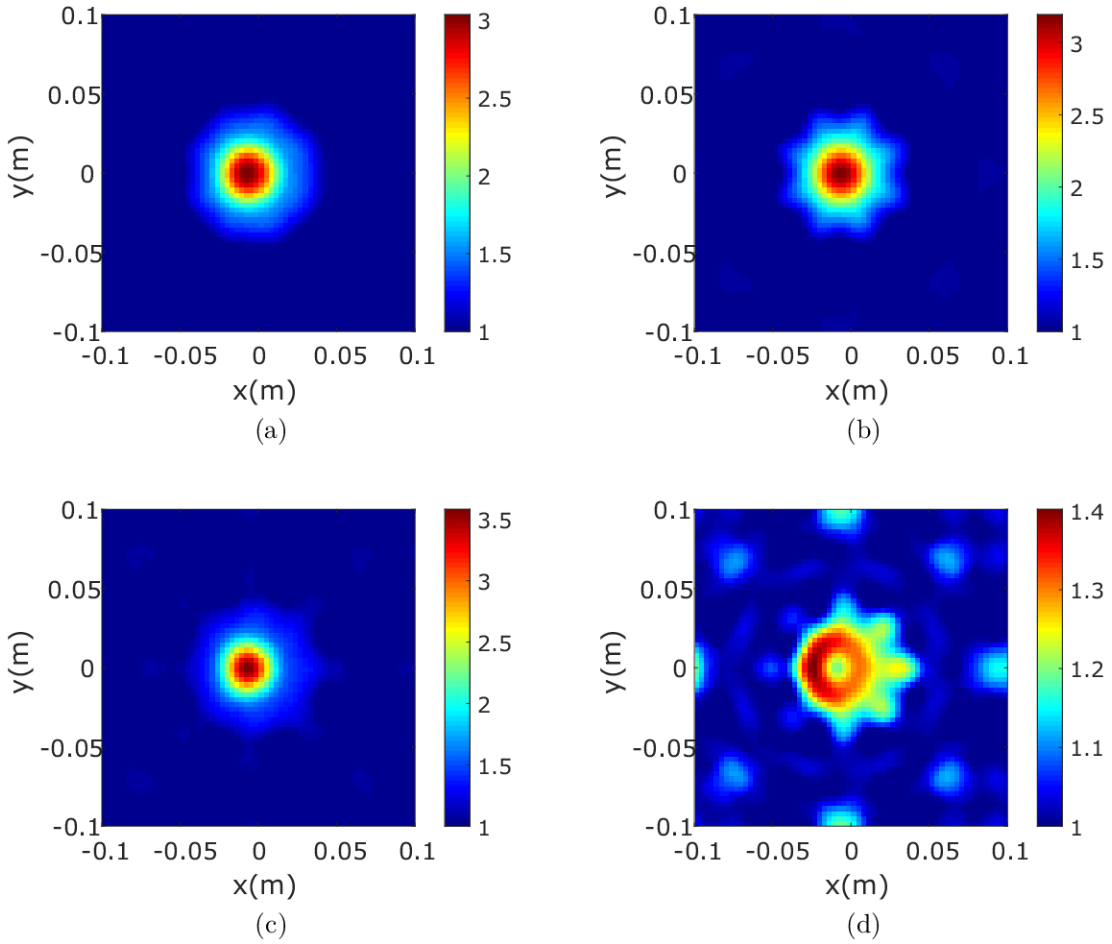

Figure 45 – Reconstruction results of the *FoamDielInt* target using frequency-hopping with 5 frequencies (2 to 6 GHz). (a) Nonlinearized CGM. (b) Linearized CGM. (c) S-CGM with $L = 10$. (d) Fast CGM.

Similarly, the reconstruction results for the *FoamTwinDiel* target using the same frequency-hopping scheme are shown in Figure 46. The error quantification of the experimental targets is given in Table 8. It is observed that the nonlinearized CGM and S-CGM combined with the frequency-hopping technique provide more accurate reconstruction profiles. In both targets, the superior performance of the S-CGM over the linearized CGM is maintained. In contrast, the fast CGM approach does not work for frequency-hopping inversion due to its limited range of applicability.

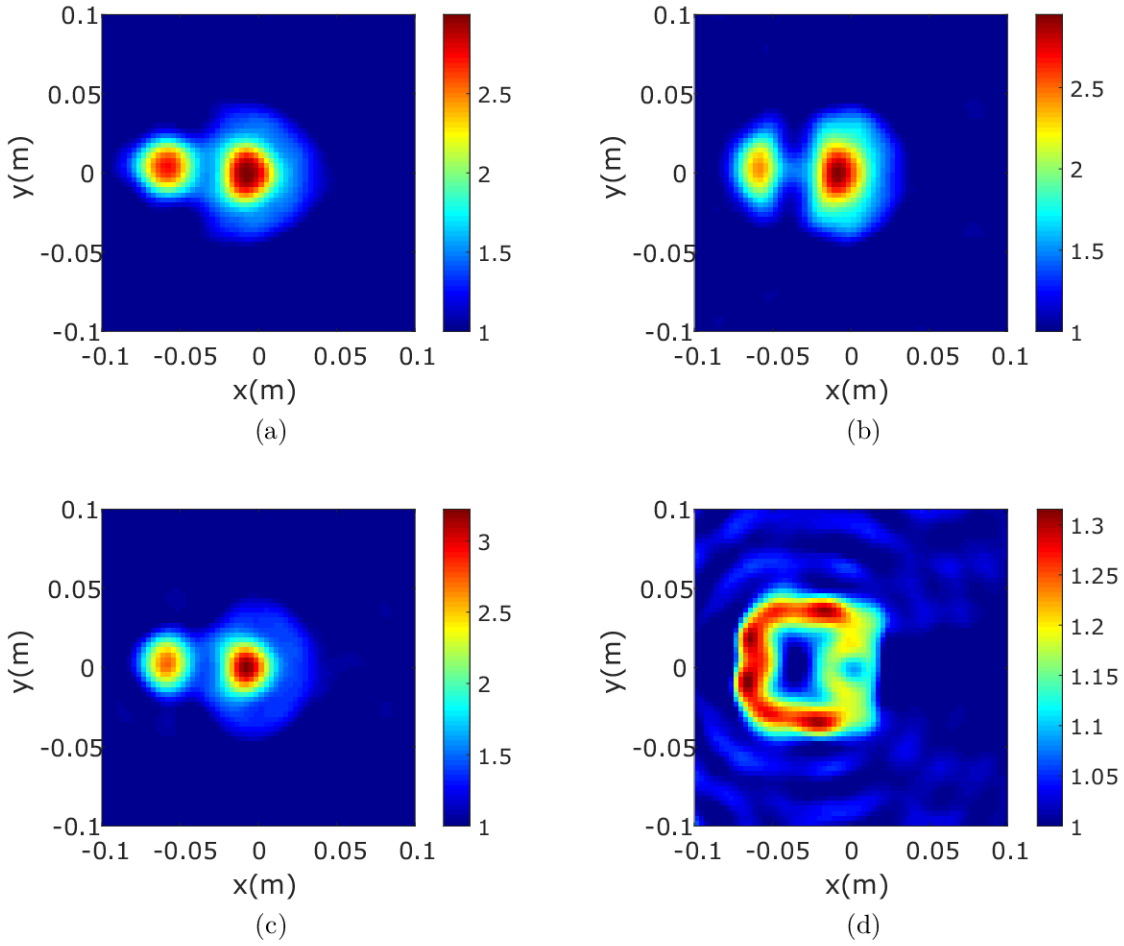

Figure 46 – Reconstruction of the *FoamTwinDiel* target using frequency-hopping with 5 frequencies (2 to 6 GHz). (a) Nonlinearized CGM. (b) Linearized CGM. (c) S-CGM with $L = 10$. (d) Fast CGM.

Table 8 – Error quantification with experimental data using frequency-hopping inversion

Method	*FoamDielInt*	*FoamTwinDiel*
	ERR_ε	ERR_ε
Nonlinearized CGM	0.0973	0.1582
Linearized CGM	0.1152	0.1795
S-CGM	0.0954	0.1569
Fast CGM	0.2261	0.3186

Finally, nonlinearized CGM and S-CGM are tested against all available data at 9 frequencies from 2 to 10 GHz with 1 GHz step. When using frequency-hopping inversion, the reconstruction by the nonlinearized CGM is successful at frequencies from 2 to 10 GHz (with 3 iterations per frequency), as shown in Figure 47, where the total error of the reconstructed profiles for the *FoamDielInt* and *FoamTwinDiel* targets are 0.0847 and 0.1483, respectively. The reconstructed profiles using the S-CGM with $L = 10$ are presented in Figure 48. The errors of reconstructions in Figure 48(a)-(b) are 0.1049 and 0.2532. It is observed that the S-CGM works for frequency-hopping inversion with all available

frequencies in the case of *FoamDielInt*. However, it fails to reconstruct the *FoamTwinDiel* target. In particular, the reconstruction of the *FoamTwinDiel* target using S-CGM is only suitable up to 7 GHz in the frequency-hopping case. Although the nonlinearized CGM solution is more accurate (with the frequency-hopping technique), the S-CGM is also capable of reconstructing objects from real data when lower frequencies are used. Furthermore, the S-CGM can be a prominent method due to its short computation time, as proved in Section 4.1.

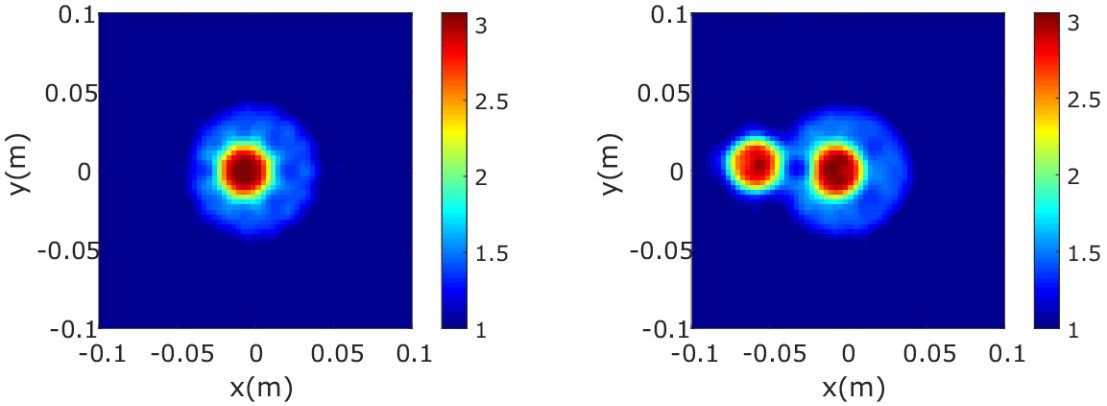

Figure 47 – Reconstruction results for the nonlinearized CGM using frequency-hopping with 9 frequencies from 2 to 10 GHz with 1 GHz step. (a) *FoamDielInt* target. (b) *FoamTwinDiel* target.

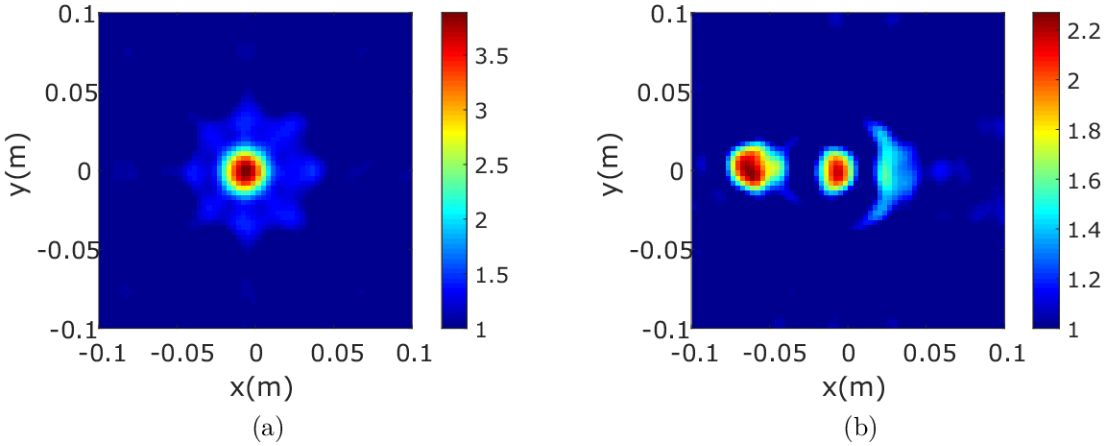

Figure 48 – Reconstruction results for the S-CGM ($L = 10$) using frequency-hopping with 9 frequencies from 2 to 10 GHz with 1 GHz step. (a) *FoamDielInt* target. (b) *FoamTwinDiel* target.

4.4 Conclusion

In this chapter, we have presented some 2D numerical results using both synthetic and experimental data. The proposed inversion algorithms show robustness against noise in the scattered data when a *priori* information on the unknown contrast is introduced. In the nonlinearized CGM, the CG-FFT approach reduces the computational cost and storage requirement of the reconstruction algorithm compared to the original version. The numerical experiments validate the reconstruction algorithm in the 2D TM case. Note that this reconstruction algorithm does not use any regularization technique. Moreover, the modified implementation makes the nonlinearized CGM significantly more efficient for large domain problems with high resolution in the reconstructed profile.

The proposed S-CGM combines the advantages of the linearized CGM and the subspace-based methods. We retrieve the deterministic part of the variational induced current by performing the SVD of the radiation operator matrix, which is calculated only once at the beginning of the iterative procedure. Thus, the S-CGM updates the total field as the sum of the estimated total field of the previous iteration and the contribution of the induced current obtained from the deterministic part of the variational induced current. The reconstruction results prove the S-CGM achieves faster convergence speed and better image reconstruction than the linearized CGM. In the S-CGM, the optimal value of parameter L can be easily chosen from different integer values rather than a single value. Therefore, the proposed S-CGM is a very interesting inversion method for the microwave imaging systems.

On the other hand, the approximation of the gradient in the fast CGM works for the reconstruction of low contrasts. This approach is computationally faster because it does not solve the full-forward problem. The approximate inverse matrix fails in the reconstruction of strong scatterers. Nevertheless, we obtain some information regarding the shape and location of the scatterers.

5 Three-Dimensional (3D) Inversion

In this chapter, we present numerical simulations to test the performance of the proposed inversion algorithms. For the 3D inversions, we choose three examples from synthetic data. In all reconstruction results, the initial solution is obtained from the back-propagation method.

5.1 Numerical Tests

5.1.1 "Off-centered sphere" profile

In the first test, we consider a dielectric sphere centered at (2, 0, 0) cm. The radius of the sphere is $R = 5$ cm and the complex relative permittivity is $\varepsilon_r = 2 - j0.5$, as shown in Figure 49. The background medium is air. The domain of interest is a 20×20×20 cm^3 cube centered at the origin. The domain of interest is illuminated by 36 vertical electric dipoles, which are located on a spherical surface of radius 0.75 m from $\theta_T = 20° - 320°$ with a step of 60° and $\phi_T = 40° - 140°$ with a step of 20°, where θ_T and ϕ_T are the elevation angle and the azimuth angle of the dipole antennas, respectively. The operating frequency is 2 GHz. The three components of the scattered field are collected by 30 receivers, which are uniformly distributed from 0° to 359° at $\theta_R = 90°$. The simulated scattered data are generated by the BiCGSTAB-FFT-based forward solver, the whole set of scattered field data collected is size $3N_r \times N_i$ (90×36). The scattered data are corrupted with 10% AWGN. In the forward problem, the domain of interest is discretized into 30×30×30 cubic cells, whereas in the inversion procedure a discretization of 20×20×20 cubic cells is used.

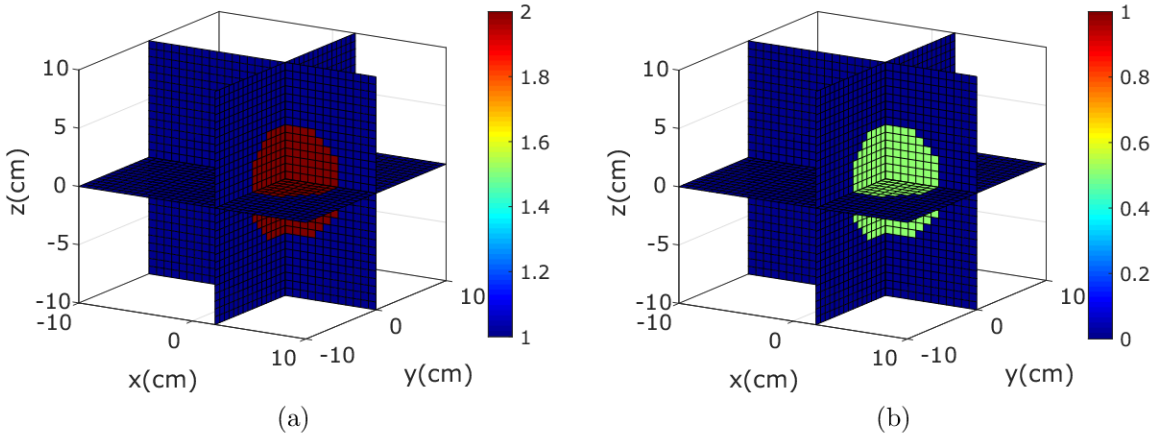

Figure 49 – Exact profile of relative permittivity. (a) Real part. (b) Negative imaginary part.

The reconstruction results (3D slice and xy plane at $z = 0$) of the real part of the relative permittivity of the sphere are shown in Figure 50, whereas the negative imaginary parts of the reconstructed images are shown in Figure 51.

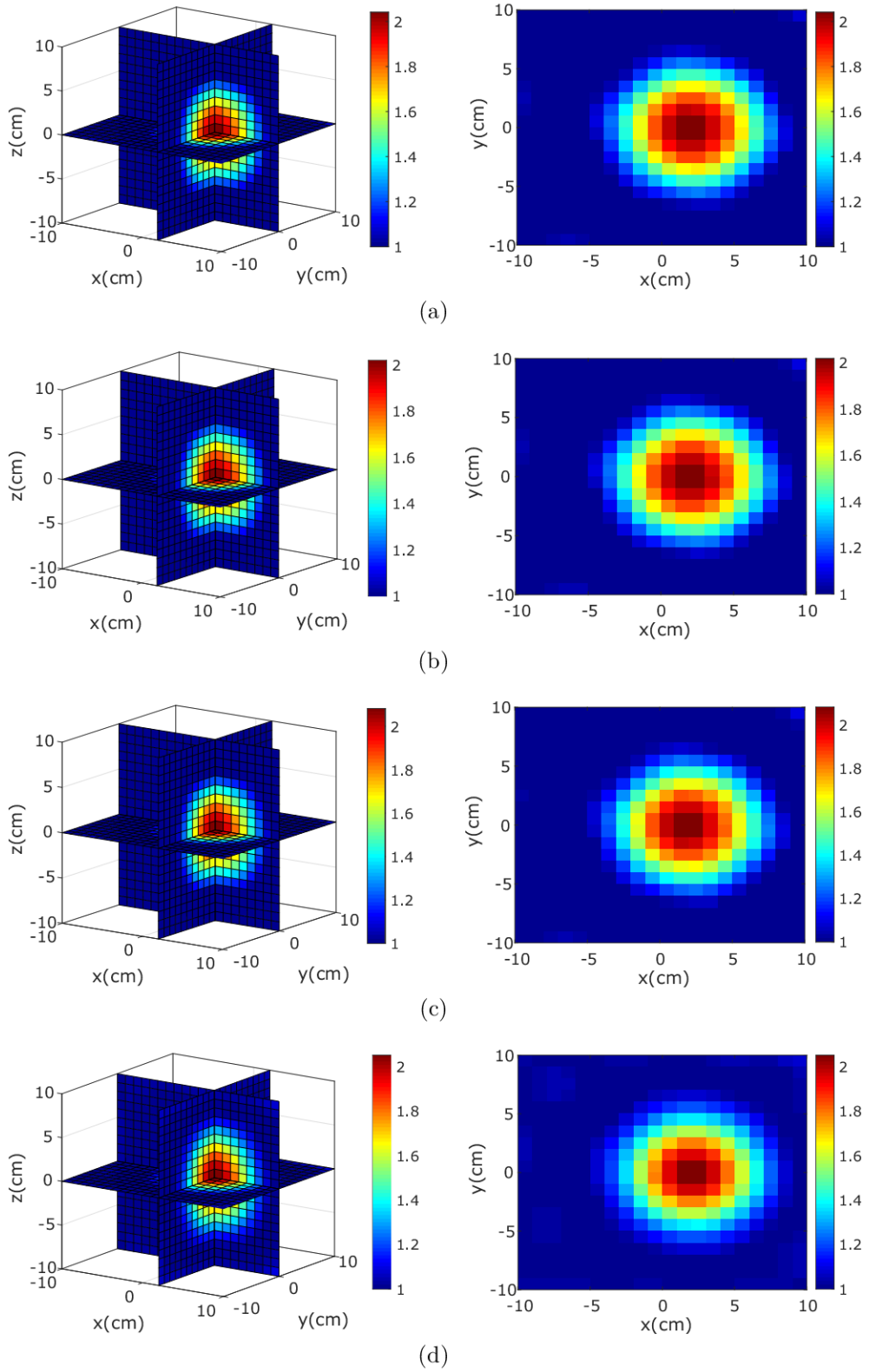

Figure 50 – Reconstructed real part of the relative permittivity profile after 30 iterations. (a) Nonlinearized CGM. (b) Linearized CGM. (c) S-CGM with $L = 20$. (d) Fast CGM.

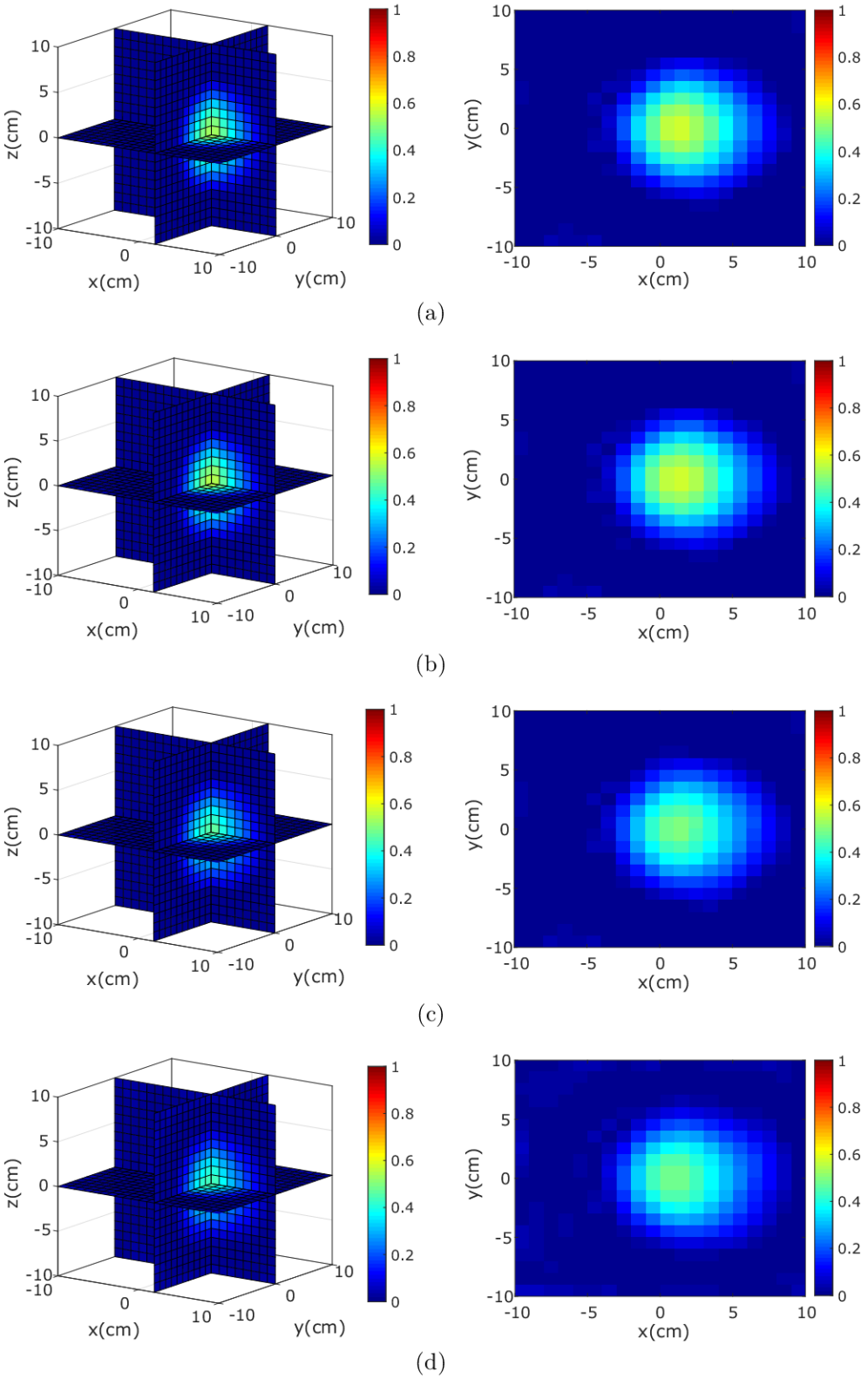

Figure 51 – Reconstructed negative imaginary part of the relative permittivity profile after 30 iterations. (a) Nonlinearized CGM. (b) Linearized CGM. (c) S-CGM with $L = 20$. (d) Fast CGM.

The curves of the permittivity profile errors are shown in Figure 52. We observe that the convergence of the methods is similar. In this case, the errors after 30 iterations of the nonlinearized CGM, linearized CGM, S-CGM, and fast CGM are 0.1345, 0.1352,

0.1355, and 0.1448, respectively. Therefore, the inversion results of the four methods are slightly different.

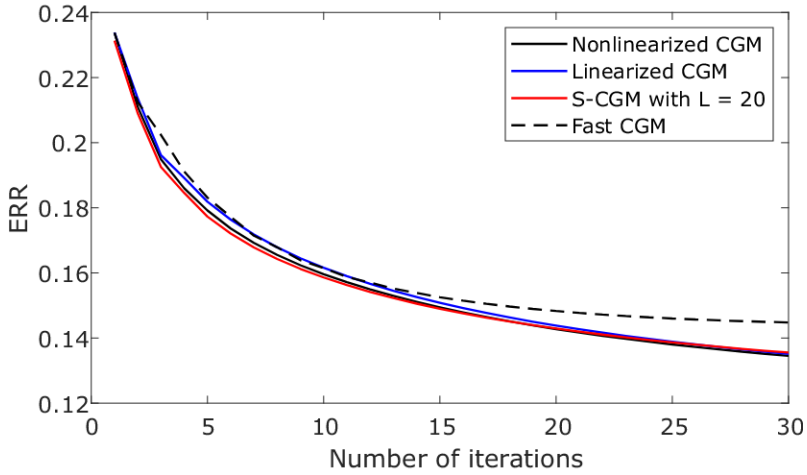

Figure 52 – Permittivity profile error using different inversion methods for the "Off-centered sphere" profile.

5.1.2 "Two parallel bars" profile

In this test, we consider two bars centered at (-0.45, 0, 0) m and (0.45, 0, 0) m. The dimensions of the two bars are 0.5 m × 1.4 m × 0.6 m. The scatterers are lossless with relative permittivity $\varepsilon_r = 2.2$. The continuous model and 3D slice of the discretized permittivity profile are depicted in Figures 53(a) and (b), respectively. The transmitters are located as in the previous test. But the radius of the spherical surface is 5 m. In this case, we use the operating frequency of 300 MHz. The scattered fields are collected by 36 receivers, which are located at the same positions as the 36 dipole sources. As in the previous example, we assume that each receiver measures the vectorial electric field in three directions. Thus, we have 108 × 36 measured data, and the synthetic data are contaminated with 10% AWGN. In inversion procedures, a 20×20×20 mesh grid is used.

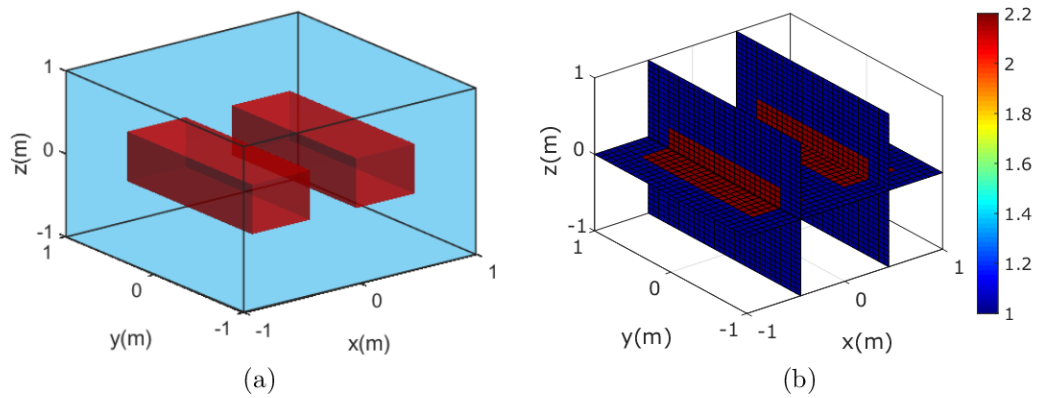

Figure 53 – "Two parallel bars" profile. (a) 3D continuous model. (b) Exact profile of relative permittivity.

The 2D slices of the reconstructed permittivity profiles are shown in Figure 54.

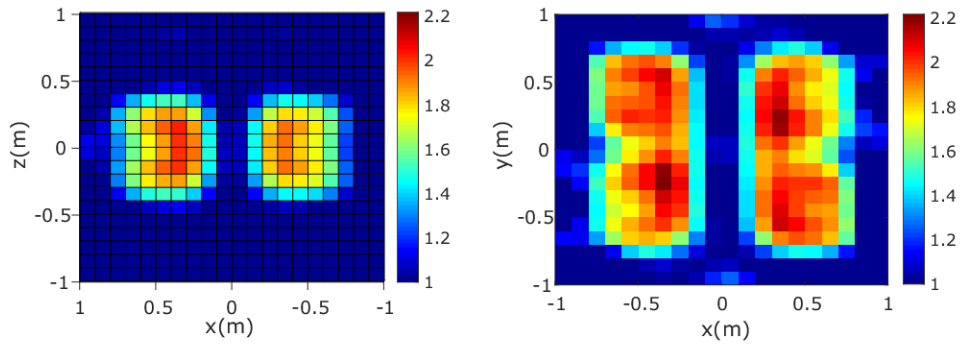

(a)

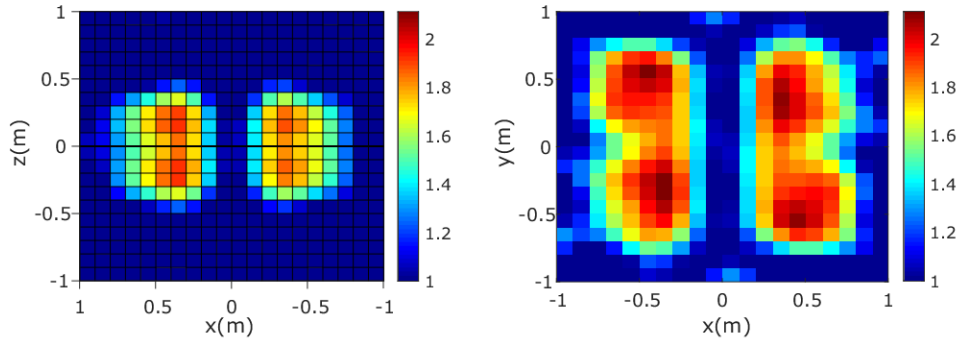

(b)

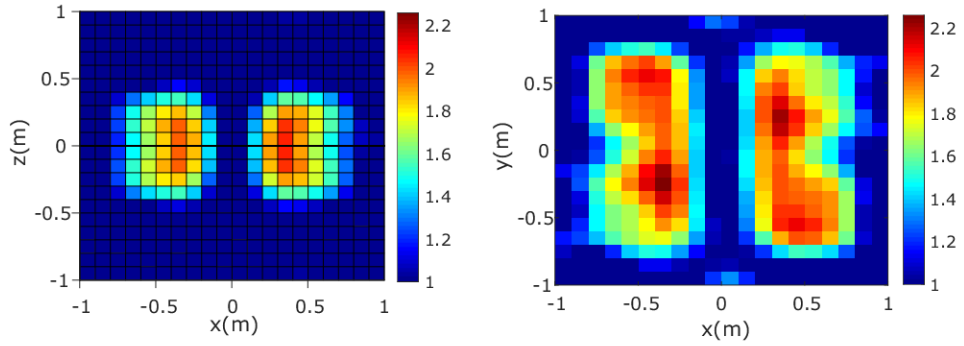

(c)

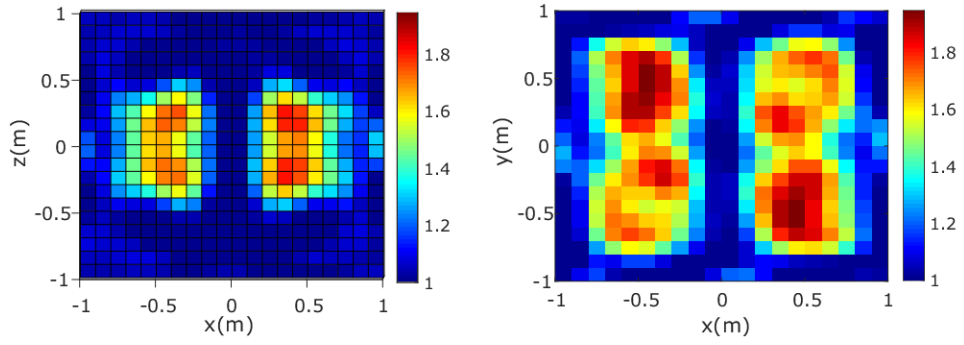

(d)

Figure 54 – Reconstructed relative permittivity profile after 40 iterations. (a) Nonlinearized CGM. (b) Linearized CGM. (c) S-CGM with $L = 35$. (d) Fast CGM.

We want to remember that the value of L in the S-CGM can be chosen from the singular values of $\overline{\overline{G}}_S$, as shown in Figure 55. It is suggested that the value of L not be greater than the index number where the singular values begin to decay dramatically. In this problem, we choose $L = 35$.

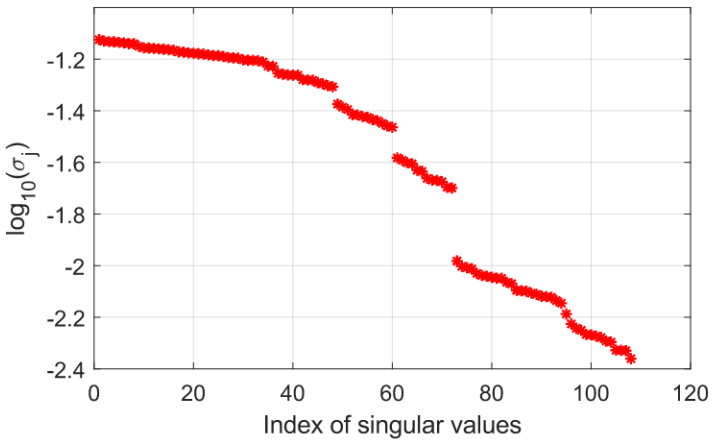

Figure 55 – Singular values of the operator $\overline{\overline{G}}_S$.

From Figure 54, we find that the size, shape, location, and permittivity of the scatterers are well reconstructed. In addition, we also can see the accuracy of the image reconstructions from the permittivity profile errors, which are decreasing all through, as shown in Figure 56. In this simulation, the errors after 40 iterations of the nonlinearized CGM, linearized CGM, S-CGM, and fast CGM are 0.1465, 0.1601, 0.1559, and 0.1875, respectively.

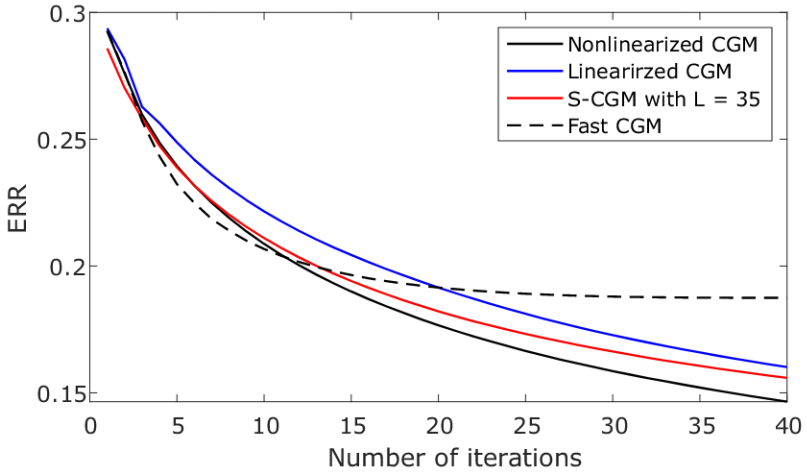

Figure 56 – Permittivity profile error using different inversion methods for the "Two parallel bars" profile.

5.1.3 "Centered cube" profile

This experiment aims at testing the ability of the different CGMs to recover extended scatterers under the assumption that the scattered data are corrupted by noise. In this test, we assume the domain of interest D of 2 m×2 m×2 m centered at the origin. The scatterer to be reconstructed is a cube of side length 1.2 m also centered at the origin. The relative permittivity of the cube is $\varepsilon_r = 2$, and the relative permittivity of the background is $\varepsilon_{rb} = 1$. The continuous model and a 3D slice of the exact profile are depicted in Figures 57(a) and (b), respectively. The operating frequency is 300 MHz and the transmitter-receiver array is located as in subsection 5.1.2. The forward scattering solver uses a 30×30×30 mesh grid, finer than the one used in the inversion procedure (20×20×20), to avoid the inverse crime. In this numerical experiment, 20% AWGN is added to the synthetic scattered data.

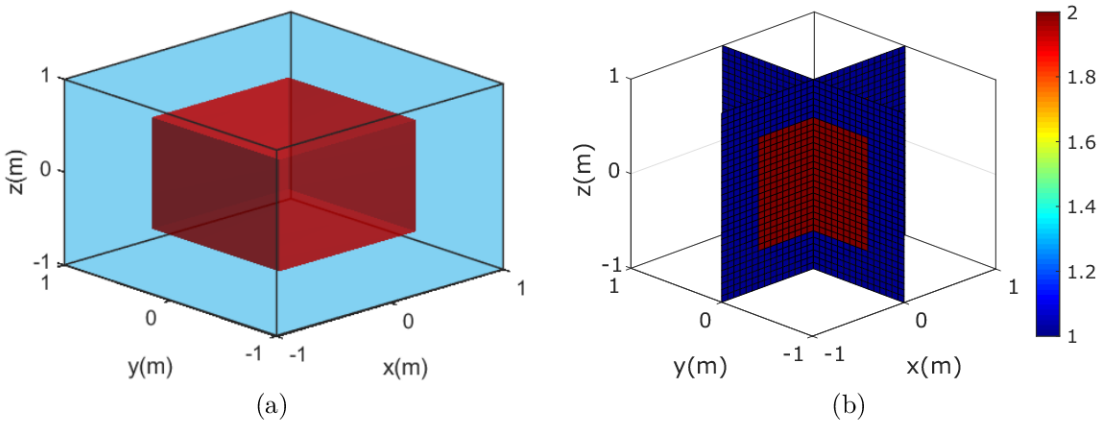

Figure 57 – "Centered cube" profile. (a) 3D continuous model. (b) Exact profile of relative permittivity.

The reconstruction results for nonlinearized CGM, linearized CGM, S-CGM, and fast CGM are shown in Figures 58(a)-(d), respectively. The 3D slices are depicted in the first column of Figure 58, whereas the 2D slices along the center of the cube (xy plane at $z = 0$) are given in the second column of Figure 58. In this case, the reconstructed profiles are obtained after 50 iterations, where the initial back-propagation solution is used. In this case, the null imaginary part of the reconstructed profile is omitted. From the reconstruction images, we observe that the reconstructed profiles show agreement between the true profile and the reconstructed one. However, this more difficult profile demonstrates that nonlinearized CGM and S-CGM have better accuracy in solving 3D inverse scattering problems with noise-corrupted data.

The trajectory of the permittivity profile error during the iterative procedure is shown in Figure 59. The errors for the reconstructed images in Figure 58(a)-(d) are 0.1053, 0.1403, 0.1122, and 0.1691, respectively.

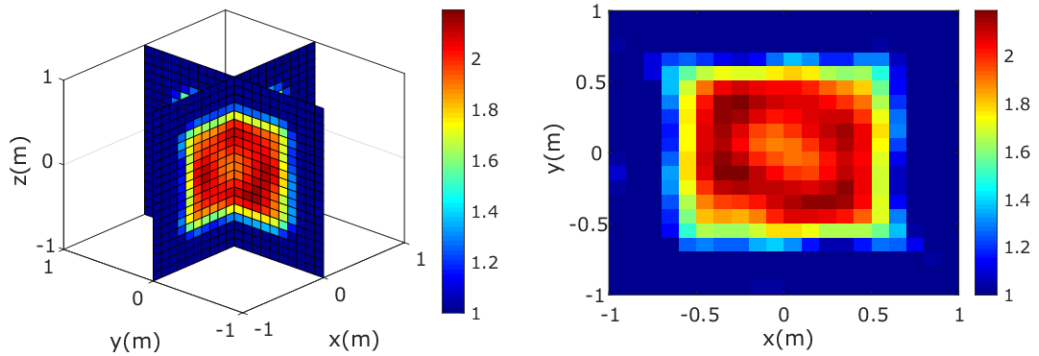

(a)

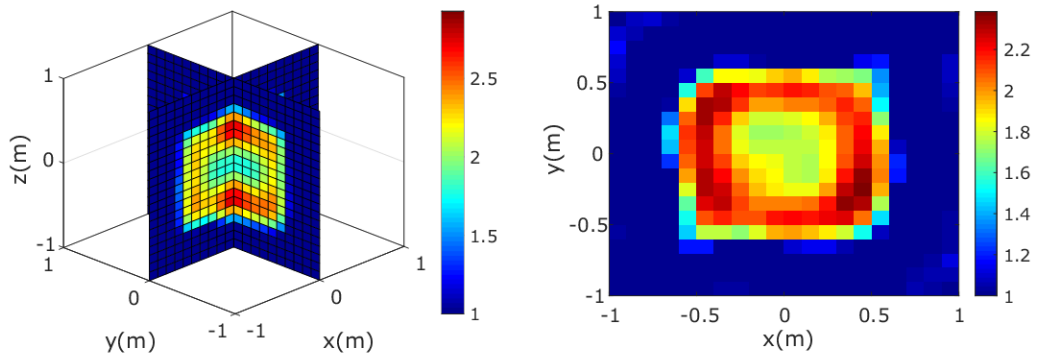

(b)

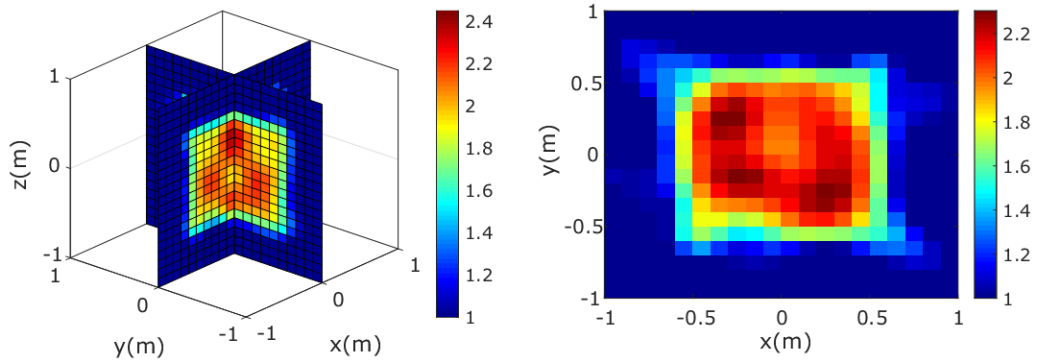

(c)

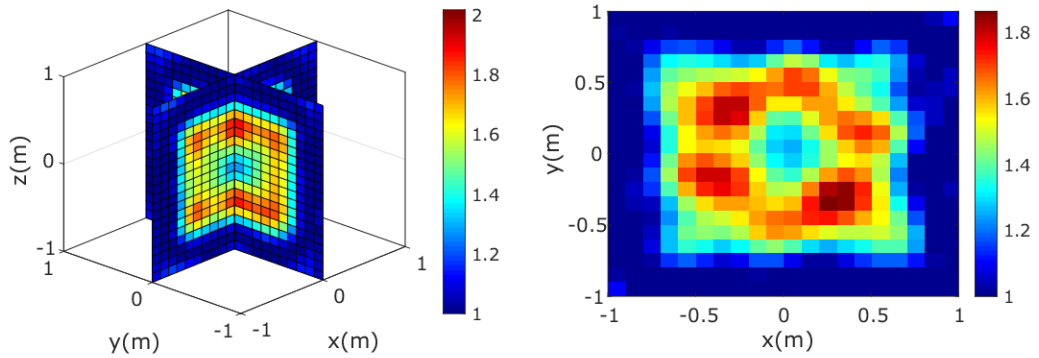

(d)

Figure 58 – Reconstructed relative permittivity profile after 50 iterations with 20% noise in the scattered data. (a) Nonlinearized CGM. (b) Linearized CGM. (c) S-CGM with $L = 35$. (d) Fast CGM.

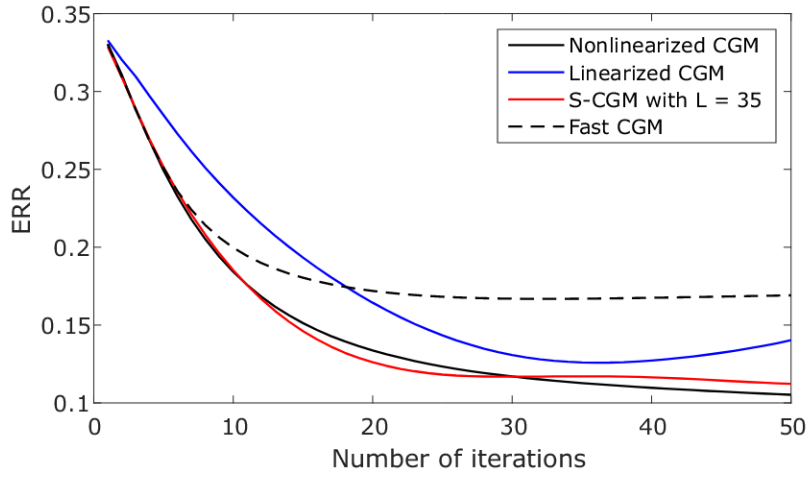

Figure 59 – Permittivity profile error using different inversion methods for the "Centered cube" profile.

In this test, the algorithms are executed on an AMD Ryzen 5 2400G, 3.6GHz with 16GB RAM with Radeon Vega Graphics. The total CPU time for the reconstructions using nonlinearized CGM, linearized CGM, S-CGM, and fast CGM under 20% noise-corrupted data are 3.64, 2.14, 3.16, and 1.46 minutes, respectively.

As in the 2D inversion case, the fast CGM is computationally faster, while the nonlinearized CGM is more time-consuming. However, the nonlinearized CGM presents better performance and robustness to noise. On the other hand, the computation time of the S-CGM is greater than that of the linearized CGM since all three components of the electric fields are used. Therefore, the receiver data points increase from N_r to $3N_r$ compared to the 2D-TM case. This additional computational cost is reflected in the calculation of the variational induced current. Nevertheless, the S-CGM and nonlinearized CGM result in similar accuracy of the reconstruction, and the computation effort of the S-CGM is less than that of the nonlinearized CGM.

5.2 Conclusion

In this chapter, we have presented some 3D numerical results using synthetic scattered data. The different CGMs are generalized to the scalar and vector formulation procedures. The efficient implementation of the forward solver with the iterative method and FFT algorithm significantly accelerates the inversion procedure and makes it suitable for applications in three-dimensional inverse scattering problems. From 3D inversion results, the CGM-based reconstruction algorithms successfully recover the shape, location, and relative permittivity of the dielectric scatterers. The proposed CGMs are also shown to be robust to noise in the three components of the scattered data.

6 Conclusions and Future Research

6.1 Conclusions

We have presented different conjugate gradient methods for solving two- and three-dimensional electromagnetic inverse scattering problems. These reconstruction algorithms can be applied to different inhomogeneous dielectric scatterers with noise-corrupted scattered data.

The proposed inversion methods in this thesis are based on gradient-based optimization approaches:

- The efficient CGM, nonlinearized CGM, reduces the computational cost and storage requirements of the original CGM implementation. In addition, this efficient CGM is found to share a computational complexity similar to the distorted-Born iterative method (DBIM). In comparison, the DBIM depends a lot on the Tikhonov regularization parameter to ensure fast convergence, while the nonlinearized CGM also achieves good results without using any regularization term.
- The subspace-based CGM (S-CGM) takes the advantages of the linearized CGM and the subspace-based methods by updating the contrast with a new total electric field approximation. Different from the original CGMs, the S-CGM uses a regularization parameter, which is defined by the number of leading singular values. This parameter can be easily chosen from different consecutive integer values instead of a single value.
- The fast CGM follows the nonlinearized CGM approach, i.e., using the nonlinear Fréchet operator to compute the gradient. This proposed method improves the computational efficiency since it uses a fast forward-solver based on inverse matrix approximation by using the Neumann series. This proposed inversion algorithm is computationally faster because it does not solve the full-forward problem. As a result, the fast CGM has good accuracy in low-degree nonlinearity problems and very short computation time.

All the inversion methods are validated in two-dimensional problems by using both synthetic and experimental data. The numerical results in the 2D case prove that the different reconstruction algorithms proposed in this thesis are feasible for microwave imaging. Depending on the contrast and electrical size of the scatterers, the nonlinear gradient approach provides a better reconstruction solution than its linear counterpart.

Besides, the forward solver approximation in the fast CGM is able to provide inversion results in a shorter period of time. For example, in problems with a low degree of nonlinearity.

The extensive validation of inversion methods to solve two-dimensional inverse scattering problems exhibits the potentialities and limitations of each of the CGMs. Fortunately, the extension of the CGMs to the three-dimensional case is straightforward. Therefore, the inversion methods are also validated in three-dimensional problems. In this case, numerical synthetic data are used.

In the 3D inversion, the performance and the solution accuracy are maintained the same as in the 2D inversion case. As expected, the numerical experiments show that the nonlinearized CGM obtains better reconstruction results in 3D problems. Reconstruction results also show robustness to noise in the scattered data. Compared to the 2D case, the computation time in the 3D case increases considerably, this is due to the fact that the three vector components of the electric fields are considered in the inversion procedures. Finally, the numerical results suggest that the proposed CGMs applied to inversion from experimental data of the three-dimensional scatterers will be feasible.

6.2 List of publications

The following journal and conference papers have been performed during the development of this thesis:

- Jose O. Vargas, André Costa Batista, Lucas S. Batista and Ricardo Adriano. On the computational complexity of the conjugate-gradient method for solving inverse scattering problems, *Journal of Electromagnetic Waves and Applications*, v. 35, n. 17, p. 2323-2334, 2021. DOI: 10.1080/09205071.2021.1946862.
- Jose O. Vargas and Ricardo Adriano. Subspace-based conjugate gradient method for solving inverse scattering problems. *IEEE Transactions on Antennas and Propagation*. (*Accepted*).
- Jose O. Vargas, André Costa Batista, Ricardo Adriano and Lucas S. Batista. A fast conjugate gradient method for solving two-dimensional electromagnetic inverse scattering problems. 20° *Simpósio Brasileiro de Micro-ondas e Optoeletrônica*, 2022. (*Accepted*).

6.3 Future research

The methods developed in this thesis could be expanded in many research aspects that can be addressed in future works. Suggestions for future work are as follows:

- Development of inversion algorithms integrating new regularization schemes and the conjugate gradient method. The standard methods are all developed in Hilbert spaces. However, regularization techniques in Banach spaces have been studied recently (Estatico; Pastorino; Randazzo, 2012; Bisio et al., 2018; Estatico et al., 2018). The Banach-space regularization approach allows for reducing the over-smoothing effects, which are often present in the standard methods.

- Propose hybrid algorithms to solve the inverse scattering problem. The efficient CGMs can be combined with stochastic algorithms, e.g., genetic and evolutionary algorithms, to improve the reconstruction in highly nonlinear problems.

- A more extensive study to validate the inversion methods in three-dimensional complex scenarios (e.g., objects buried in multilayered media), as well as validation with experimental data, in order to highlight the advantages and limitations of the CGMs when using 3D vector formulations. In addition, the frequency-hopping technique can be applied in three-dimensional inverse scattering problems, as in the 2D inversion presented in this thesis.

References

Abubakar, A.; Habashy, T. M.; Pan, G.; Li, M. Application of the multiplicative regularized gauss–newton algorithm for three-dimensional microwave imaging. *IEEE Transactions on Antennas and Propagation*, v. 60, n. 5, p. 2431–2441, 2012.

Abubakar, A.; Van den Berg, P. M.; Mallorqui, J. J. Imaging of biomedical data using a multiplicative regularized contrast source inversion method. *IEEE Transactions on Microwave Theory and Techniques*, v. 50, n. 7, p. 1761–1771, 2002.

Agarwal, K.; Song, R.; D'Urso, M.; Chen, X. Improving the performances of the contrast source extended born inversion method by subspace techniques. *IEEE Geoscience and Remote Sensing Letters*, v. 10, n. 2, p. 391–395, 2013.

Balanis, C. A. *Advanced engineering electromagnetics*. New York: John Wiley Sons, 1989.

Barrowes, B. E.; Teixeira, F. L.; Kong, J. A. Fast algorithm for matrix–vector multiply of asymmetric multilevel block-toeplitz matrices in 3-d scattering. *Microwave and Optical technology letters*, v. 31, n. 1, p. 28–32, 2001.

Belkebir, K.; Chaumet, P. C.; Sentenac, A. Superresolution in total internal reflection tomography. *J. Opt. Soc. Am. A*, v. 22, n. 9, p. 1889–1897, 2005.

Bevacqua, M. T.; Crocco, L.; Di Donato, L.; Isernia, T. Non-linear inverse scattering via sparsity regularized contrast source inversion. *IEEE Transactions on Computational Imaging*, v. 3, n. 2, p. 296–304, 2017.

Bevacqua, M. T.; Isernia, T. An effective rewriting of the inverse scattering equations via green's function decomposition. *IEEE Transactions on Antennas and Propagation*, v. 69, n. 8, p. 4883–4893, 2021.

Bisio, I. et al. Brain stroke microwave imaging by means of a newton-conjugate-gradient method in l^p banach spaces. *IEEE Transactions on Microwave Theory and Techniques*, v. 66, n. 8, p. 3668–3682, 2018.

Caorsi, S.; Massa, A.; Pastorino, M.; Rosani, A. Microwave medical imaging: potentialities and limitations of a stochastic optimization technique. *IEEE Transactions on Microwave Theory and Techniques*, v. 52, n. 8, p. 1909–1916, 2004.

Catedra, M. F.; Gago, E. Spectral domain analysis of conducting patches of arbitrary geometry in multilayer media using the cg-fft method. *IEEE Transactions on Antennas and Propagation*, v. 38, n. 10, p. 1530–1536, 1990.

Chandra, R.; Zhou, H.; Balasingham, I.; Narayanan, R. M. On the opportunities and challenges in microwave medical sensing and imaging. *IEEE Transactions on Biomedical Engineering*, v. 62, n. 7, p. 1667–1682, 2015.

Chaumet, P. C.; Belkebir, K. Three-dimensional reconstruction from real data using a conjugate gradient-coupled dipole method. *Inverse Problems*, v. 25, n. 2, p. 024003, fev. 2009.

Chen, X. Subspace-based optimization method for solving inverse-scattering problems. *IEEE Transactions on Geoscience and Remote Sensing*, v. 48, n. 1, p. 42–49, 2010.

Chen, X. *Computational methods for electromagnetic inverse scattering.* : John Wiley Sons, 2018.

Chew, W.; Lin, J. A frequency-hopping approach for microwave imaging of large inhomogeneous bodies. *IEEE Microwave and Guided Wave Letters*, v. 5, n. 12, p. 439–441, 1995.

Chew, W. C.; Wang, Y. M. Reconstruction of two-dimensional permittivity distribution using the distorted born iterative method. *IEEE Transactions on Medical Imaging*, v. 9, n. 2, p. 218–225, 1990.

Colton, D.; Kress, R. *Inverse acoustic and electromagnetic scattering theory.* New York, NY: Springer Nature, 2019. v. 93.

Colton, D.; Päivärinta, L. The uniqueness of a solution to an inverse scattering problem for electromagnetic waves. *Archive for Rational Mechanics and Analysis*, v. 119, n. 1, p. 59–70, 1992.

Cui, T. J.; Chew, W. C.; Aydiner, A. A.; Chen, S. Inverse scattering of two-dimensional dielectric objects buried in a lossy earth using the distorted born iterative method. *IEEE Transactions on Geoscience and Remote Sensing*, v. 39, n. 2, p. 339–346, 2001.

Donelli, M.; Franceschini, D.; Rocca, P.; Massa, A. Three-dimensional microwave imaging problems solved through an efficient multiscaling particle swarm optimization. *IEEE Transactions on Geoscience and Remote Sensing*, v. 47, n. 5, p. 1467–1481, 2009.

Donelli, M.; Massa, A. Computational approach based on a particle swarm optimizer for microwave imaging of two-dimensional dielectric scatterers. *IEEE Transactions on Microwave Theory and Techniques*, v. 53, n. 5, p. 1761–1776, 2005.

Estatico, C.; Pastorino, M.; Randazzo, A. A novel microwave imaging approach based on regularization in l^p banach spaces. *IEEE Transactions on Antennas and Propagation*, v. 60, n. 7, p. 3373–3381, 2012.

Estatico, C.; Pastorino, M.; Randazzo, A.; Tavanti, E. Three-dimensional microwave imaging in l^p banach spaces: Numerical and experimental results. *IEEE Transactions on Computational Imaging*, v. 4, n. 4, p. 609–623, 2018.

Franchois, A.; Pichot, C. Microwave imaging-complex permittivity reconstruction with a levenberg-marquardt method. *IEEE Transactions on Antennas and Propagation*, v. 45, n. 2, p. 203–215, 1997.

Gan, H.; Chew, W. A discrete bcg-fft algorithm for solving 3d inhomogeneous scatterer problems. *Journal of Electromagnetic Waves and Applications*, v. 9, n. 10, p. 1339–1357, 1995.

Geffrin, J.-M.; Sabouroux, P.; Eyraud, C. Free space experimental scattering database continuation: experimental set-up and measurement precision. *Inverse Problems*, IOP Publishing, v. 21, n. 6, p. S117–S130, nov 2005.

Glasko, V. B. Inverse problems in mathematical physics. *American Institute of Physics*, 1984.

Habashy, T. M.; Groom, R. W.; Spies, B. R. Beyond the born and rytov approximations: A nonlinear approach to electromagnetic scattering. *Journal of Geophysical Research: Solid Earth*, v. 98, n. B2, p. 1759–1775, 1993.

Habashy, T. M.; Oristaglio, M. L.; Hoop, A. T. d. Simultaneous nonlinear reconstruction of two-dimensional permittivity and conductivity. *Radio Science*, v. 29, n. 04, p. 1101–1118, 1994.

Hadamard, J. *Lectures on Cauchy's problem in linear partial differential equations.* : Yale University Press, 1923.

Hansen, P. C.; O'Leary, D. P. The use of the l-curve in the regularization of discrete ill-posed problems. *SIAM Journal on Scientific Computing*, v. 14, n. 6, p. 1487–1503, 1993.

Harada, H.; Wall, D. J. N.; Takenaka, T.; Tanaka, M. Conjugate gradient method applied to inverse scattering problem. *IEEE Transactions on Antennas and Propagation*, v. 43, n. 8, p. 784–792, 1995.

Harrington, R. F. *Field Computation by Moment Methods*. New York: McMillan, 1968.

Jin, J. M. *Theory and computation of electromagnetic fields*. 2nd. ed. : John Wiley Sons, 2015.

Kharkovsky, S.; Zoughi, R. Microwave and millimeter wave nondestructive testing and evaluation - overview and recent advances. *IEEE Instrumentation Measurement Magazine*, v. 10, n. 2, p. 26–38, 2007.

Li, L. et al. Deepnis: Deep neural network for nonlinear electromagnetic inverse scattering. *IEEE Transactions on Antennas and Propagation*, v. 67, n. 3, p. 1819–1825, 2019.

Liu, C.; Wang, Y.; Heng, P. A. A comparison of truncated total least squares with tikhonov regularization in imaging by ultrasound inverse scattering. *Physics in Medicine and Biology*, v. 48, n. 15, p. 2437–2451, 2003.

Liu, Z.; Nie, Z. Subspace-based variational born iterative method for solving inverse scattering problems. *IEEE Geoscience and Remote Sensing Letters*, v. 16, n. 7, p. 1017–1020, 2019.

Livesay, D.; Chen, K. Electromagnetic fields induced inside arbitrarily shaped biological bodies. *IEEE Transactions on Microwave Theory and Techniques*, v. 22, n. 12, p. 1273–1280, 1974.

Lobel, P.; Kleinman, R. E.; Pichot, C.; Blanc-Feraud, L.; Barlaud, M. Conjugate-gradient method for soliving inverse scattering with experimental data. *IEEE Antennas and Propagation Magazine*, v. 38, n. 3, p. 48–51, 1996.

Ma, H. F.; Zhang, J. F.; Chen, X.; Cheng, Q.; Cui, T. J. Cg-fft algorithm for three-dimensional inhomogeneous and biaxial metamaterials. *Waves in Random and Complex Media*, v. 19, n. 1, p. 49–64, 2009.

Massa, A. et al. Parallel ga-based approach for microwave imaging applications. *IEEE Transactions on Antennas and Propagation*, v. 53, n. 10, p. 3118–3127, 2005.

Massa, A.; Pastorino, M.; Rosani, A.; Benedetti, M. A microwave imaging method for nde/ndt based on the smw technique for the electromagnetic field prediction. *IEEE Transactions on Instrumentation and Measurement*, v. 55, n. 1, p. 240–247, 2006.

Massoudi, H.; Durney, C.; Iskander, M. Limitations of the cubical block model of man in calculating sar distributions. *IEEE Transactions on Microwave Theory and Techniques*, v. 32, n. 8, p. 746–752, 1984.

Mojabi, P.; LoVetri, J. Overview and classification of some regularization techniques for the gauss-newton inversion method applied to inverse scattering problems. *IEEE Transactions on Antennas and Propagation*, v. 57, n. 9, p. 2658–2665, 2009.

Mudry, E.; Chaumet, P. C.; Belkebir, K.; Sentenac, A. Electromagnetic wave imaging of three-dimensional targets using a hybrid iterative inversion method. *Inverse Problems*, v. 28, n. 6, p. 065007, apr 2012.

Oliveri, G.; Ding, P.; Poli, L. 3-d crack detection in anisotropic layered media through a sparseness-regularized solver. *IEEE Antennas and Wireless Propagation Letters*, v. 14, p. 1031–1034, 2015.

Pastorino, M. *Microwave Imaging.* : John Wiley Sons, 2010.

Pastorino, M.; Massa, A.; Caorsi, S. A microwave inverse scattering technique for image reconstruction based on a genetic algorithm. *IEEE Transactions on Instrumentation and Measurement*, v. 49, n. 3, p. 573–578, 2000.

Persico, R. *Introduction to ground penetrating radar: inverse scattering and data processing.* : John Wiley Sons, 2014.

Peterson, A. F.; Ray, S. L.; Chen, C. H.; Mittra, R. Numerical implementations of the conjugate gradient method and the cg-fft for electromagnetic scattering. *Progress In Electromagnetics Research*, v. 05, p. 241–300, 1991.

Peterson, A. F.; Ray, S. L.; Mittra, R. *Computational Methods for Electromagnetics.* New York: IEEE press, 1998.

Remis, R. F.; van den Berg, P. M. On the equivalence of the newton-kantorovich and distorted born methods. *Inverse Problems*, v. 16, n. 1, p. L1–L4, 2000.

Richmond, J. Scattering by a dielectric cylinder of arbitrary cross section shape. *IEEE Transactions on Antennas and Propagation*, v. 13, n. 3, p. 334–341, 1965.

Rocca, P.; Benedetti, M.; Donelli, M.; Franceschini, D.; Massa, A. Evolutionary optimization as applied to inverse scattering problems. *Inverse Problems*, IOP Publishing, v. 25, n. 12, p. 123003, nov 2009.

Roy, D. N. G.; Couchman, L. S. *Inverse problems and inverse scattering of plane waves.* : Academic Press, 2001.

Sarkar, T.; Arvas, E.; Rao, S. Application of fft and the conjugate gradient method for the solution of electromagnetic radiation from electrically large and small conducting bodies. *IEEE Transactions on Antennas and Propagation*, v. 34, n. 5, p. 635–640, 1986.

Shi, Y.; Liang, C. Application of the spatial–spectral cg-fft method for the solution of electromagnetic scattering by buried flat metallic objects. *IEEE Geoscience and Remote Sensing Letters*, v. 4, n. 1, p. 37–40, 2007.

Song, L.-P.; Liu, Q. H. Fast three-dimensional electromagnetic nonlinear inversion in layered media with a novel scattering approximation. *Inverse problems*, v. 20, n. 6, p. S171, 2004.

Song, L.-P.; Yu, C.; Liu, Q. H. Through-wall imaging (twi) by radar: 2-d tomographic results and analyses. *IEEE Transactions on Geoscience and Remote Sensing*, v. 43, n. 12, p. 2793–2798, 2005.

Stewart, G. W. *Matrix Algorithms.* : Philadelphia, PA, USA: SIAM, 1998.

Su, C.-C. Calculation of electromagnetic scattering from a dielectric cylinder using the conjugate gradient method and fft. *IEEE Transactions on Antennas and Propagation*, v. 35, n. 12, p. 1418–1425, 1987.

Su, C.-C. The three-dimensional algorithm of solving the electric field integral equation using face-centered node points, conjugate gradient method, and fft. *IEEE Transactions on Microwave Theory and Techniques*, v. 41, n. 3, p. 510–515, 1993.

Van Bladel, J. Some remarks on green's dyadic for infinite space. *IRE Transactions on Antennas and Propagation*, v. 9, n. 6, p. 563–566, 1961.

Van den Berg, P. M.; Kleinman, R. E. A contrast source inversion method. *Inverse Problems*, v. 13, n. 6, p. 1607–1620, 1997.

Van den Berg, P. M.; Van Broekhoven, A. L.; Abubakar, A. Extended contrast source inversion. *Inverse Problems*, v. 15, n. 5, p. 1325–1344, 1999.

Van der Vorst, H. A. Bi-cgstab: A fast and smoothly converging variant of bi-cg for the solution of nonsymmetric linear systems. *SIAM Journal on scientific and Statistical Computing*, v. 13, n. 2, p. 631–644, 1992.

Vogel, C. *Computational Methods for Inverse Problems.* : Society for Industrial and Applied Mathematics, 2002. (Frontiers in Applied Mathematics).

Wang, Y. M.; Chew, W. C. An iterative solution of the two-dimensional electromagnetic inverse scattering problem. *International Journal of Imaging Systems and Technology*, v. 1, n. 1, p. 100–108, 1989.

Wilton, D. R.; E. Wheeler III, J. Comparison of convergence rates of the conjugate gradient method applied to various integral equation formulations. *Progress In Electromagnetics Research*, v. 05, p. 131–158, 1991.

Xu, K.; Zhong, Y.; Chen, X.; Lesselier, D. A fast integral equation-based method for solving electromagnetic inverse scattering problems with inhomogeneous background. *IEEE Transactions on Antennas and Propagation*, v. 66, n. 8, p. 4228–4239, 2018.

Xu, K.; Zhong, Y.; Wang, G. A hybrid regularization technique for solving highly nonlinear inverse scattering problems. *IEEE Transactions on Microwave Theory and Techniques*, v. 66, n. 1, p. 11–21, 2018.

Xu, X. M.; Liu, Q. H.; Zhang, Z. Q. The stabalized biconjugate gradient fast fourier transform method for electromagnetic scattering. *Applied Computational Electromagnetics Society Journal*, v. 17, n. 1, p. 97–103, 2003.

Ye, X.; Chen, X. Subspace-based distorted-born iterative method for solving inverse scattering problems. *IEEE Transactions on Antennas and Propagation*, v. 65, n. 12, p. 7224–7232, 2017.

Zhang, W.; Liu, Q. H. Three-dimensional scattering and inverse scattering from objects with simultaneous permittivity and permeability contrasts. *IEEE Transactions on Geoscience and Remote Sensing*, v. 53, n. 1, p. 429–439, 2015.

Zhang, Z. Q.; Liu, Q. H. Three-dimensional weak-form conjugate- and biconjugate-gradient fft methods for volume integral equations. *Microwave and Optical Technology Letters*, v. 29, n. 5, p. 350–356, 2001.

Zhang, Z. Q.; Liu, Q. H. Applications of the bcgs-fft method to 3-d induction well logging problems. *IEEE Transactions on Geoscience and Remote Sensing*, v. 41, n. 5, p. 998–1004, 2003.

Zhang, Z. Q. et al. Microwave breast imaging: 3-d forward scattering simulation. *IEEE Transactions on Biomedical Engineering*, v. 50, n. 10, p. 1180–1189, 2003.

Zhang, Z. Q.; Liu, Q. H.; Xu, X. M. Rcs computation of large inhomogeneous objects using a fast integral equation solver. *IEEE Transactions on Antennas and Propagation*, v. 51, n. 3, p. 613–618, 2003.

Zhdanov, M. S.; Fang, S.; Hursán, G. Electromagnetic inversion using quasi-linear approximation. *Geophysics*, v. 65, n. 5, p. 1501–1513, 2000.

Zhong, Y.; Chen, X. An fft twofold subspace-based optimization method for solving electromagnetic inverse scattering problems. *IEEE Transactions on Antennas and Propagation*, v. 59, n. 3, p. 914–927, 2011.

Zhong, Y.; Chen, X.; Agarwal, K. An improved subspace-based optimization method and its implementation in solving three-dimensional inverse problems. *IEEE Transactions on Geoscience and Remote Sensing*, v. 48, n. 10, p. 3763–3768, 2010.

Zhou, Y.; Zhong, Y.; Wei, Z.; Yin, T.; Chen, X. An improved deep learning scheme for solving 2-d and 3-d inverse scattering problems. *IEEE Transactions on Antennas and Propagation*, v. 69, n. 5, p. 2853–2863, 2021.

Zhu, G. K. *Sphere scattering*. MATLAB Central File Exchange, 2022. Available on: <https://www.mathworks.com/matlabcentral/fileexchange/31119-sphere-scattering>.

Zwamborn, P.; van den Berg, P. M. The three dimensional weak form of the conjugate gradient fft method for solving scattering problems. *IEEE Transactions on Microwave Theory and Techniques*, v. 40, n. 9, p. 1757–1766, 1992.

APPENDIX A – Implementation details

This appendix presents some important details for the Matlab implementation of fast algorithms for matrix-vector multiplication in scattering problems. The Matlab commands provided in this appendix can be easily ported into other programming languages.

A.1 Two-dimensional case

The first step of the implementation consists in discretizing the domain of interest as follows

```
%% DISCRETIZATION BY CELLS

% Length of each cell in x and y-axis
dx = (xmax-xmin)/Nx;
dy = (ymax-ymin)/Ny;

% Centers of each cell
x = xmin-(Nx/2-1)*dx : dx: xmax+(Nx/2 -1)*dx;
y = ymin-(Ny/2-1)*dy : dy: ymax+(Ny/2 -1)*dy;
[xe,ye] = ndgrid(x,y);  % Extended domain (2Nx-1)x(2Ny-1)

% distance between the cells
Rmn = sqrt(xe.^2 + ye.^2);  % size (2Nx-1)x(2Ny-1)
```

The second step is to compute the dyadic Green's function. The entries of the matrix $\overline{\overline{G}}$ produce a Toeplitz matrix due to the property of translational invariance of the Green's function kernel. Therefore, we use uniform cells to preserve the convolutional symmetry in the matrix and the elements of the matrix are calculated as follows

```
%% COMPUTING DYADIC GREEN'S FUNCTION

% Matrix elements for off-diagonal entries
Gmn = -((1i*pi*kb*a)/2)*besselj(1,kb*a)*besselh(0,2,kb*Rmn); % m=/n

% Matrix elements for diagonal entries
Gmn(Nx,Ny)= -((1i*pi*kb*a)/2)*besselh(1,2,kb*a) - 1;         % m==n
```

The next step is to create a circular discrete convolution, then the extended matrix $\overline{\overline{G}}^e$ is obtained by

```
% Extended matrix Ge. (2Nx-1)x(2Ny-1)
Ge = zeros(2*Nx-1,2*Ny-1);
Ge(1:Nx,1:Ny) = Gmn(Nx:2*Nx-1,Ny:2*Ny-1);
Ge(Nx+1:2*Nx-1,Ny+1:2*Ny-1) = Gmn(1:Nx-1,1:Ny-1);
Ge(1:Nx,Ny+1:2*Ny-1) = Gmn(Nx:2*Nx-1,1:Ny-1);
Ge(Nx+1:2*Nx-1,1:Ny) = Gmn(1:Nx-1,Ny:2*Ny-1);
```

Finally, the matrix-vector product is performed using FFT and the result is extracted from the extended matrix as follows

```
%% Computing matrix-vector product by using two-dimensional FFT

u = reshape(u,Nx,Ny);
e = ifft2(fft2(Ge).*fft2(u,2*Nx-1,2*Ny-1)); % Product G*U
e = e(1:Nx,1:Ny,:);
e = reshape(e,Nx*Ny,1);
```

A.2 Three-dimensional case

In this case, the 3D domain is discretized as follows

```
%% DISCRETIZATION BY CELLS

% Length of each cell in x, y, and z-axis
dx = (xmax-xmin)/Nx;
dy = (ymax-ymin)/Ny;
dz = (zmax-zmin)/Nz;

% Centers of each cell
x = xmin-(Nx/2-1)*dx : dx: xmax+(Nx/2 -1)*dx;
y = ymin-(Ny/2-1)*dy : dy: ymax+(Ny/2 -1)*dy;
z = zmin-(Nz/2-1)*dz : dz: zmax+(Nz/2 -1)*dz;
[xe,ye,ze] = ndgrid(x,y,z);  % Extended domain (2Nx-1)x(2Ny-1)x(2Nz-1)

% distance between the cells
R = sqrt(xe.^2 + ye.^2 + ze.^2);  % size (2Nx-1)x(2Ny-1)x(2Nz-1)
```

The second step is to compute the dyadic Green's function. For example, for DGFE implementation the elements of the matrix are calculated as follows

```
%% COMPUTING DYADIC GREEN'S FUNCTION

% Matrix elements for off-diagonal blocks
Gxy = -(dv./(4*pi.*R.^3)).*exp(-1i*kb*R).*(((x.*y)./R.^2)...
       .*((kb*R).^2 - 3*1i*kb*R - 3));
Gxy(Nx,Ny,Nz) = 0;

Gxz = -(dv./(4*pi.*R.^3)).*exp(-1i*kb*R).*(((x.*z)./R.^2)...
        .*((kb*R).^2 - 3*1i*kb*R - 3));
Gxz(Nx,Ny,Nz) = 0;

Gyz = -(dv./(4*pi.*R.^3)).*exp(-1i*kb*R).*(((y.*z)./R.^2)...
        .*((kb*R).^2 - 3*1i*kb*R - 3));
Gyz(Nx,Ny,Nz) = 0;

% Matrix elements for diagonal blocks
Cn  = (2/3)*(1i*kb*a + 1)*exp(-1i*kb*a) - 1;

Gxx = -(dv./(4*pi.*R.^3)).*exp(-1i*kb*R).*...
       ((1-(kb*R).^2 +1i*kb*R)+(x./R).^2.*((kb*R).^2 - 3*1i*kb*R - 3 ));
Gxx(Nx,Ny,Nz) = Cn;

Gyy = -(dv./(4*pi.*R.^3)).*exp(-1i*kb*R).*...
       ((1-(kb*R).^2 +1i*kb*R)+(y./R).^2.*((kb*R).^2 - 3*1i*kb*R - 3 ));
Gyy(Nx,Ny,Nz) = Cn;

Gzz = -(dv./(4*pi.*R.^3)).*exp(-1i*kb*R).*...
       ((1-(kb*R).^2 +1i*kb*R)+(z./R).^2.*((kb*R).^2 - 3*1i*kb*R - 3 ));
Gzz(Nx,Ny,Nz) = Cn;
```

The next step is create a 3D circular discrete convolution, then the extended matrix of each block $\overline{\overline{G}}^{e}_{x_p x_q}$ is obtained by

```
% Extended matrix Ge. (2Nx-1)x(2Ny-1)x(2Nz-1)
Ge = zeros(2*Nx-1,2*Ny-1,2*Nz-1);
Ge(1:Nx,1:Ny,1:Nz) = G(Nx:2*Nx-1,Ny:2*Ny-1,Nz:2*Nz-1);
Ge(1:Nx,1:Ny,Nz+1:2*Nz-1) = G(Nx:2*Nx-1,Ny:2*Ny-1,1:Nz-1);
```

```
Ge(1:Nx,Ny+1:2*Ny-1,1:Nz) = G(Nx:2*Nx-1,1:Ny-1,Nz:2*Nz-1);
Ge(1:Nx,Ny+1:2*Ny-1,Nz+1:2*Nz-1) = G(Nx:2*Nx-1,1:Ny-1,1:Nz-1);
Ge(Nx+1:2*Nx-1,1:Ny,1:Nz) = G(1:Nx-1,Ny:2*Ny-1,Nz:2*Nz-1);
Ge(Nx+1:2*Nx-1,1:Ny,Nz+1:2*Nz-1) = G(1:Nx-1,Ny:2*Ny-1,1:Nz-1);
Ge(Nx+1:2*Nx-1,Ny+1:2*Ny-1,1:Nz) = G(1:Nx-1,1:Ny-1,Nz:2*Nz-1);
Ge(Nx+1:2*Nx-1,Ny+1:2*Ny-1,Nz+1:2*Nz-1) = G(1:Nx-1,1:Ny-1,1:Nz-1);
```

Finally, the matrix-vector product of each component of the DGF is performed using 3D FFT and the result is extracted from the extended matrix as follows

```
%% Computing matrix-vector product by using three-dimensional FFT

u = reshape(u,Nx,Ny,Nz);
e = ifftn(fftn(Ge).*fftn(u,[2*Nx-1 2*Ny-1 2*Nz-1])); % Product G*U
e = e(1:Nx,1:Ny,1:Nz,:);
e = reshape(e,Nx*Ny*Nz,1);
```

APPENDIX B – Back-propagation method

B.1 Back-propagation procedure to obtain an initial guess

The reconstruction algorithm based on back-propagation (BP) procedure uses the adjoint operator or conjugate transpose $\overline{\overline{G}}_S^H$. For each incidence l, we estimate the contrast source

$$\overline{J}_l = \gamma\, \overline{\overline{G}}_S^H \cdot \overline{E}_l^{sca}, \tag{B.1}$$

where the scalar weight γ is determined by minimizing the following cost function

$$F(\gamma) = \sum_{l=1}^{N_i} \left\| \overline{E}_l^{sca} - \gamma\, \overline{\overline{G}}_S \cdot \overline{\overline{G}}_S^H \cdot \overline{E}_l^{sca} \right\|_S^2. \tag{B.2}$$

The minimization of (B.2) requires that $\frac{\partial F}{\partial \gamma} = 0$, this leads to an analytical solution for γ, given by

$$\gamma = \frac{\left\langle \overline{E}_l^{sca}, \overline{\overline{G}}_S \cdot \overline{\overline{G}}_S^H \cdot \overline{E}_l^{sca} \right\rangle_S}{\left\| \overline{\overline{G}}_S \cdot \overline{\overline{G}}_S^H \cdot \overline{E}_l^{sca} \right\|_S^2}. \tag{B.3}$$

The total electric field $\overline{E}_l$ inside the domain of interest can be calculated by

$$\overline{E}_l = \overline{E}_l^{inc} + \overline{\overline{G}}_D \cdot \overline{J}_l. \tag{B.4}$$

Finally, the solution for the contrast function $\overline{\overline{\chi}}$ inside the domain can be obtained analytically as

$$\overline{\overline{\chi}} = \frac{\sum_{l=1}^{N_i} \overline{J}_l \odot \overline{E}_l^*}{\sum_{l=1}^{N_i} \left\| \overline{E}_l \right\|^2}. \tag{B.5}$$